UNIVERSITY OF CALIFORNIA
RIVERSIDE

Structure-Property Relationships, and Biomimetic Designs from the Compression-Resistant Cuticle of the Ironclad Beetle

A Dissertation submitted in partial satisfaction
of the requirements for the degree of

Doctor of Philosophy

in

Materials Science and Engineering

by

Jesus Rivera

September 2020

Dissertation Committee:
Prof. David Kisailus, Chairperson
Prof. Pablo Zavattieri
Prof. Suveen Mathaudhu

The Dissertation of Jesus Rivera is approved:

Committee Chairperson

University of California, Riverside

Acknowledgments

This research was supported by grants from Airforce Office of Scientific Research, AFOSR, Multi-University Research Initiative, Award# FA9550-15-1-0009. We also like to thank the Army Research Office DURIP Grant (W911NF-16-1-0208) for the MIRA SEM and AFOSR DURIP Grant W911NF-16-1-0208, for the Hysitron nanoindenter. I would also like to thank the Institute of Global Innovation Research (GIR) at TUAT for their support. This research used resources of the Central Facility for Advanced Microscopy and Microanalysis (CFAMM) as well as the Advanced Light Source, which is a DOE Office of Science User Facility under contract no. DE-AC02-05CH11231.

First, I would like to thank my advisor, Professor David Kisailus, for providing me with the opportunity to work in his lab and be a part of his research group. I truly appreciate everything he has done for me over the years and the ability to be part of this exciting and impactful research. During my time in his lab, Dr. Kisailus has provided me countless opportunities to interface with the top researchers, work in world class facilities, and attend a variety of domestic and international conferences, and for that I will be forever grateful. Furthermore, I would like to thank Dr. Kisailus for constantly pushing me to achieve more and never settling for what is easy. I know things may have not always been easy for him, but I truly appreciate all the care and effort he took to ensure I realized my full potential. I truly appreciate everything I have learned from him over the years and for this wonderful opportunity.

Next, I would like to thank all my current and past lab members specifically, Chris Salinas, Para wee Pumwongpitak, Nick Yaraghi, Steven Herrera, Ramya Mohan, Thomas

Dagger, Luz Cruz, Taifeng Wang, Rushing Zhao, Morgan Dundon, Joshua Edwards, Wei Huang, Satoshi Murata, Nana Matsumoto, Drago Vagile and Allison Pickle. All of you have truly made this a wonderful experience and I appreciate your support and friendship over the years.

To my collaborators and instructors, I would like to thank Pablo Zavattieri, Atsushi Arakaki, Krassimir Bozhilov, Suveen Mathaudhu, Luis Zepeda-Ruiz, David Restrepo, Philip Flater, Dilworth Parkinson, Harold Barnard, Maryam Sadat Hosseini, Keisuke Matsushita you have taught me so much during this experience and I thank you for your mentorship and guidance.

Ultimately, I want to thank my family for always supporting me in all my endeavors. Thank you, Mom, Dad, and Con. Your love and support mean more to me than you will ever know.

ABSTRACT OF THE DISSERTATION

Structure-Property Relationships, and Biomimetic Designs from the Compression-Resistant Cuticle of the Ironclad Beetle

by

Jesus Rivera

Doctor of Philosophy, Graduate Program in Materials Science and Engineering
University of California, Riverside, June 2020
Prof. David Kisailus, Chairperson

Biological composites provide valuable design guidelines to produce the next generation of engineering materials. Incorporating readily available resources in environmentally friendly method, these biological organisms produce lightweight, strong, and tough materials with superior mechanical properties to engineering counterparts. The key to this success results from their hierarchical organization as well as structural and compositional gradients imparted by an ordered self-assembly of organic material. In this work we study the structure-mechanical property relationship and multifunctional nature of a compression resistant beetle elytra able to withstand crushing and piercing attacks from predators while thriving in an arid desert environment. We uncover the macro and microstructural architectural features responsible for transferring stress and imparting localized stiffness and compliance to toughen the bulk biological composite. These insights are then subsequently applied to the fabrication of bioinspired fiber reinforced composites using conventional engineering materials and additive manufacturing. Validating their

performance, mechanical testing was used to highlight the enhanced performance of these biological materials compared to industry standard designs. This work may further provide insights into the fabrication of lightweight, strong, and tough structural materials for use in engineering applications.

Table of Contents

List of Figures

Chapter 1: Introduction

Technology has been limited by the relative understanding of materials to the point where the prominent material of the age defines the civilization. Initially, the creation of simple tools from readily available resources such as stone and wood marked the initial stages of humanity. Through thousands of years of development and a greater understanding of materials advancements in technology flourished. This increase in understanding remains the driving principle in materials science and has lead humanity through various ages from bronze to steel and now polymer composite and nanomaterials. Ever expanding with our knowledge, materials science remains an interdisciplinary field involving related subspecialties including metallurgy, ceramics, semiconductors, nanotechnology, composites, and biomaterials all striving to enhance technology.

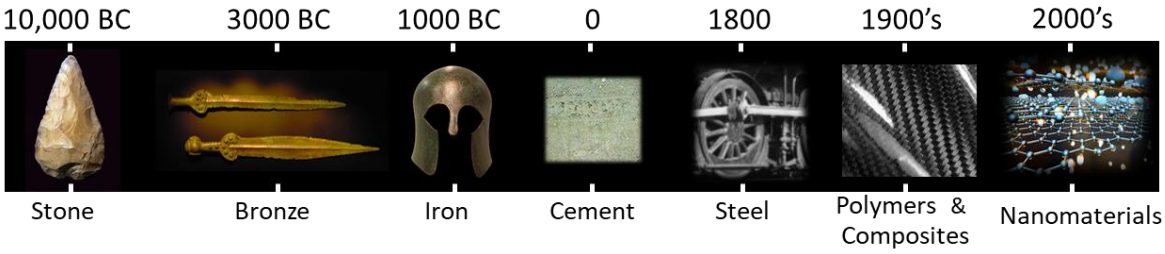

Figure 1. 1. Materials development over the ages. Images highlighting the advancements and latest technology of the period. Images composited from shutterstock.com.

In the current generation, pressing engineering challenges and increasing carbon emissions are pushing material scientists and engineers to enhance mechanical, optical, and thermal properties in structural materials (*1*, *2*). Therefore, there remains an industry demand for a new generation of structural components that improves upon current strength

and toughness (*1*–*3*). To understand these properties further we must first define what they represent. In engineering terms, toughness refers to the maximum amount of energy a material absorbs before failing while strength represents the total stress; force over a given cross-sectional area, withstood by a material before plasticly deforming or failing. Conventionally, strength and toughness remain mutually exclusive, with materials only typically possessing one of these factors (*4*). For instance, polymers exhibiting increased extensibility show high toughness, yet lack compressive strength. This energy absorbing deformative nature remains a prime motive for the incorporation of polymers in bumpers of automobiles. In contrast, ceramics displaying high compressive strength typically fail to have the extensibility of other materials leading to fracture under impact or bending loads. This behavior is prevalently seen in the catastrophic failure of ceramic cups or plates when dropped. Addressing these limitations, developments of metal and alloy materials seek to merge these properties yet suffer from density concerns that hinder widespread application where light weight is key. Alternative solutions include composites such as fiber reinforced materials adopted in industry applications to overcome individual material limitations. The Ashby plot in Figure 1.2 highlights the ability for composites to merge strength and toughness. Despite suffering high production cost barriers that hinder broad adoption, these composites have been utilized in performance materials such as electric vehicles, buildings, automobiles, and aircrafts (*5*, *6*).

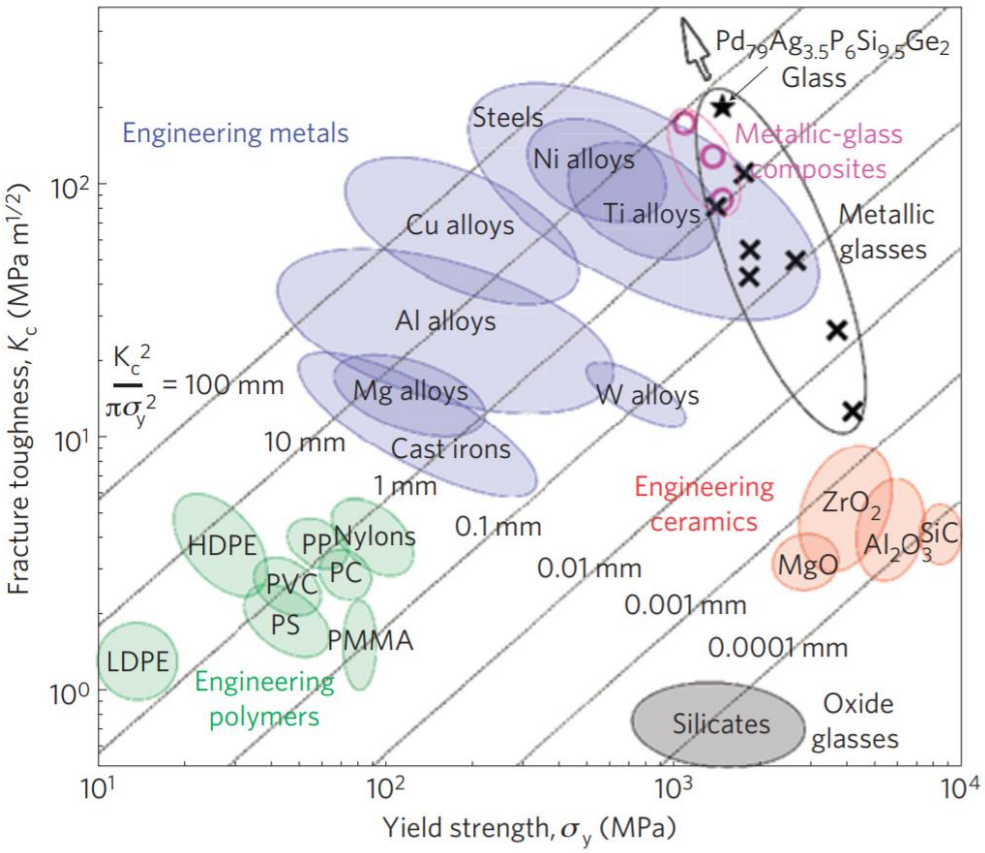

Figure 1. 2. Ashby map of the damage tolerance (toughness) versus yield strength of materials highlighting the performance benefit of composites (*4*).

Through generations, composite materials have a widespread history of incorporation. The onset of their use remains up for debate, yet history includes references to varying forms of composite materials. Early adoption saw Israelites combining straw into the fabrication of their mud bricks to increase their strength. The ancient Egyptians pioneered plywood to resist swelling due to moisture and thermal expansion apart from increasing the strength of the wood. Apart from fibrous composites, Medieval blacksmith layered different metals in the pursuit of better swords. Currently, refinement of processing

techniques has brought a rise to the incorporation of fiber reinforced polymer matrix composites.

Composite materials remain ideal for structural applications requiring high stiffness-to-weight and strength-to-weight ratios. Beneficial properties have driven a great adoption of composites in the aerospace and automotive industries. Notable high-performance examples include the interstage mandrel of the SpaceX Falcon 9 rocket and the monocoque shells of formula one racecars reminiscent of fighter jet cockpits (*6*, *7*). Ever expanding in their adoption, composites account for upwards to 30-40 percent of modern airframe production with these percentages increasing with every advancement of production. Modern widespread adoption includes the Airbus A-350 which represented the first use of a fuselage and wings manufactured primarily using carbon fiber reinforced polymers (*8*).

Graphite or carbon fibers remains the filament of choice in today's composites due to their high strength-to-density and stiffness-to-density ratios (*9*). Both can be manufactured from pitch, rayon, or polyacrylonitrile (PAN) precursor fibers by carbonization in an inert atmosphere at 1700 °C - 3000°C to partially graphitize the fibers. Increasing the temperature during this process yields fibers with a greater modulus but lower strength. After this process the final product is a fiber around 10 μm in diameter with a tensile strength of 1.7 GN/m^2 that can be woven into a fabric and infused with a matrix (*10*, *11*).

To produce structural elements capable of bearing load, these fibrous elements must be bonded together using a matrix material. This binding matrix is typically less stiff, strong, and dense than the fibers yet is tasked with supporting, protecting, and transferring load between the elements. Through the combination of these materials the resulting composite

can have elevated stiffness and strength while still maintaining low density. In engineering structures this matrix material can vary between polymers, ceramics metals or carbon depending on the needs of the final structure.

Engineering composites such as carbon fiber, concrete and ceramics possess appealing mechanical properties yet suffer from drawbacks. Often costly to the environment and industry, these materials are typically manufactured with energy intensive processes, that require high temperatures and pressures to synthesize the specific components or involve environmentally toxic chemicals such as strong acids or bases (*1*, *2*). A prevalent example remains the production of carbon fiber. The production of the precursors for the fiber element of this composite involves use of toxic and corrosive chemicals including nitric acid and dimethylacetamide and high heating temperatures (*10*, *11*). With encroaching environmental standards, alternative manufacturing techniques for these materials must be implemented to incorporate efficient and sustainable production methods, reduce cost and lower environmental impact.

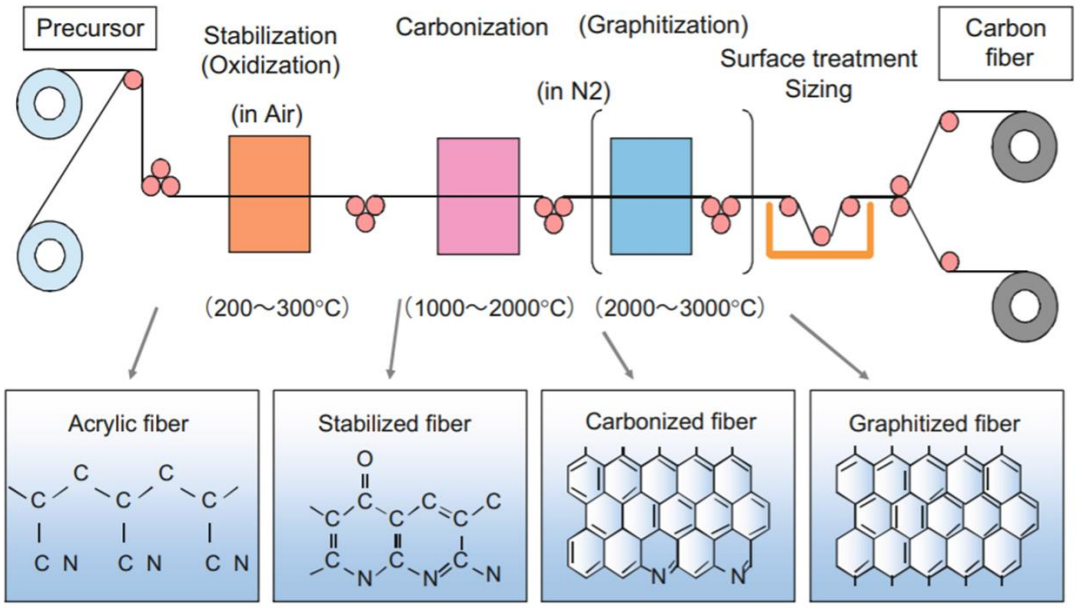

Figure 1. 3. Temperature and chemical intensive Carbon fiber production process (*10*).

When faced with the challenge of fabricating the next generation of strong and tough materials, researchers must examine the experts that have been doing this for hundreds of millions of years. Nature serves as a great inspiration due to its ability to synthesize a wide range of materials at ambient temperatures and pressure using readily available resources. These structures exhibit unique or superior performance versus engineering counterparts with their strength and toughness being, in part, attributed to the hierarchical assembly of different components. Incorporating multifunctionality into these structural materials enables these organisms to have defenses against predators without sacrificing sensing or feeding functions (*12*, *13*). The optimization of resources in these natural systems remain rather fascinating as a limited subset of elements are responsible for these complex structures.

Biological composites are generally segregated into relatively hard mineralized or softer nonmineralized structures. Sharing a variety of organic components these structures incorporate polysaccharides such as chitin, lignin, cellulose and hemicellulose or proteinaceous biopolymers like keratin, collagen, and elastin (*13–16*). Lacking the availability to relatively stiff organic elements responsible for increased strength in mineralized systems, non-mineralized organisms must harness the intermolecular bonds to fortify their tissue, typically relying on hydrogen bonds or the crosslinking of polymer chains. In contrast mineralized organisms incorporate calcium phosphate, calcium carbonate or silicon dioxide in crystalline or amorphous forms to achieve their strength (*13, 15*).

Depending on inherently weak and brittle materials nature must develop alternative architectural strategies to fortify its constituents. Exhibiting exceptional efficiency, nature often sparingly uses materials to reduce weight with no hindrance to mechanical performance. For these biological systems strong structure-function relationships drives performance of these biopolymers and biominerals through the incorporation of controlled gradients and specific hierarchical designs assembled from the nano to macroscale. (*16–19*). An Ashby diagram highlights this optimization of resources allowing for unique properties (Figure 1.4) (*20*). By controlling the density of these materials, nature can vary its modulus exhibiting values that range from 100 to 0.1 GPa (*21*). Typically, mutually exclusive in engineering materials strength and toughness begin to coexist in biological structures. Incorporating relatively soft matter with stiff minerals in complex structures nature overcomes the engineering conflicts between strength and toughness. Examining an

Ashby plot comparing the stiffness and toughness of natural materials we begin to see the enhanced benefits of architected composites. Therefore, to fully understand these features we must study these natural systems.

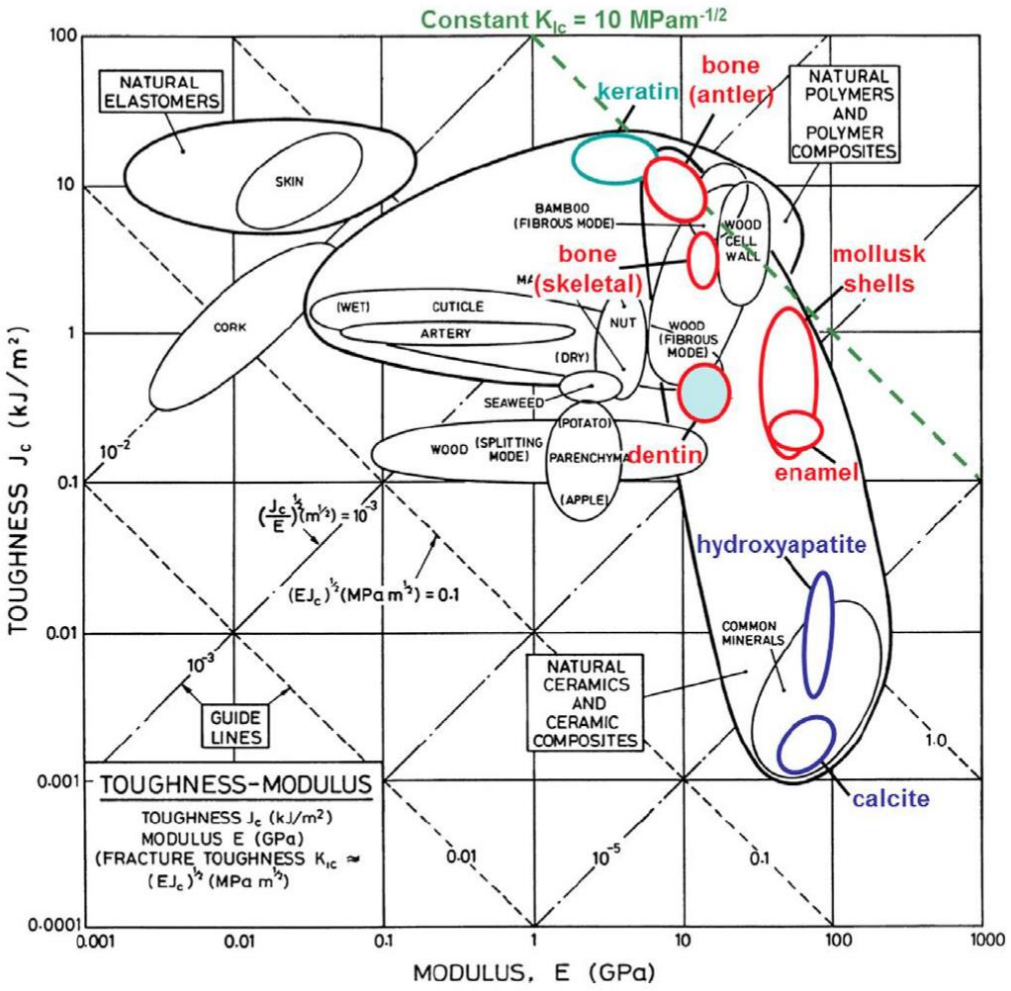

Figure 1. 4. Wegst-Ashby plot highlighting variations in toughness vs Young's modulus of natural materials. Adapted from (*21*)

Found in the internal layers of mollusk sells, nacre remains a prevalent example of the structure-performance relationships in biological materials. Considered one of the best natural composite armors, nacre exhibits high mechanical strength, stiffness, and fracture

toughness due to the architectural arrangement of its constituents. This organic mineral composite consists of polygonal calcium carbonate plates separated by biopolymer forming a lamellar sandwich structure. These aragonite plates range from two to five hundred nanometers in thickness and encompass about ninety five percent of the structure with the organic polymer occupying the rest (*22*). Hierarchical in construction, the mineralized plates are formed from millions of single crystal nano-grains that are bound by chitin fibers and proteins. Compared to the crystalline form of calcium carbonate, aragonite, the nacre structure shows a forty-fold increase in fracture toughness due to the change in architecture (*23*). This structural change provided increased toughness by deterring crack propagation that plagued the pure aragonite structure (*24*). Figure 1.5 shows the toughening mechanisms found in nacre. These features highlight how the inorganic hard mineral plates cause a stiff response while the interlayer shear of the organic components contributes to inelastic deformation that dissipates energy and enhances toughness. By studying the fractured surface of nacre Figure 1.5 C, we observe the jagged structure resulting from the pullout of tablets. Incorporating this hierarchical architecture enables toughening mechanisms that include tablet bridging, micro voids, biopolymer phase viscoplasticity and deflection of the crack tip that ultimately provide key design insights (*25*, *26*).

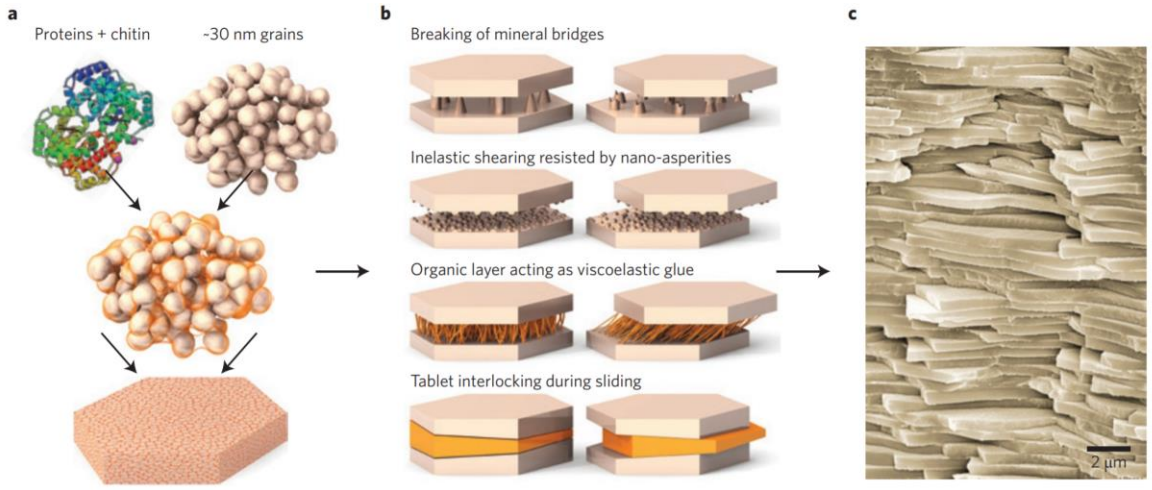

Figure 1. 5. Nacre structure and toughening mechanisms. (A) Architecture and composition of single nacre plate. (B) Toughening mechanisms found between plates that include mineral bridging, viscoelastic glue, mineral bridging. (C) False colored SEM micrograph of fractured brick and mortar nacre structure. (*23*)

Through the study and understanding of the structure-property relations and the synthesis of biological materials, we can apply the countless advancements seen in evolution to the creation of the next-generation structural and multifunctional materials. The application of these ideals remains the driving force in biomimetic composites. In engineering, bio-inspired materials take design influenced from nature and apply it to the production of synthetic systems. An example of this is seen in light harvesting photonic materials that take cues from photosynthesis in plants and the design of engineering actuators motivated by the movement of jelly fish (*27*, *28*). Unlike these composites, biomimetics seeks to mimic the processes and hierarchical designs by which the natural materials are formed (*29*, *30*). The increase of structural mimics of natural systems over the past decade highlights the expansion of this field (2; 53; 68-70; 75-80). At the forefront of innovation a variety of manufacturing processes such as fiber reinforced composite

processing, 3D printing, magnetically-assisted slip casting, and freeze casting have facilitated the production of composite materials mimicking these natural microstructures (*31*). Closely mimicking the features in biological structures, production methods such as freeze casting have allowed researchers to create similar hierarchical architectures such as brick and mortar tablets with mineral bridges and nano asperities that provide enhanced toughening in the natural nacre system (*32*). By incorporating engineering materials like hydroxy apatite and alumina, into these architectures researchers have exceeded the performance of the natural systems (*33*).

Looking to the natural world we are met with a variety of fascinating systems to gain insight for bio-inspiration. With over 350,000 species of flying, terrestrial and aquatic variants, beetle cuticles exemplify these traits by providing structural support, water collection and retention, and serve as a defense mechanism against crushing and piercing predators (*30*, *34–37*). Particularly the evolution of the organism's delicate forewings to exoskeletal hardened forewings or elytra, represents the impetus for the evolutionary diversification of the order Coleoptera (*38*).

Unlike aquatic ancestors that incorporate heavy mineral into their protective structures, beetle represent a relatively light weight fiber reinforced polymeric composite. These non-mineralized composites consist of an orchestrated hierarchical assembly of alpha-chitin fibers embedded within a proteinaceous matrix that provides both strength and toughness (*39–41*). The high strength and reduced weight of this cuticle structure results from a honeycomb architecture, incorporation of trabecula, and a stacked layered structure (*42*). A proposed model of the internal layered arrangement of the cuticle is shown in Figure 1.6.

Helicoidal organization of layers have been found in some species with neighboring layers varying by about 45° (*43*, *44*). Within each ply unidirectional fibers fortify the cuticle and have been reported to wrap around the trabecula structure. This arid arrangement of the cuticle is primarily tuned to sustain flight, yet evolutionary variants among these microstructures provide increased resistance to ecological pressures (*45*, *46*).

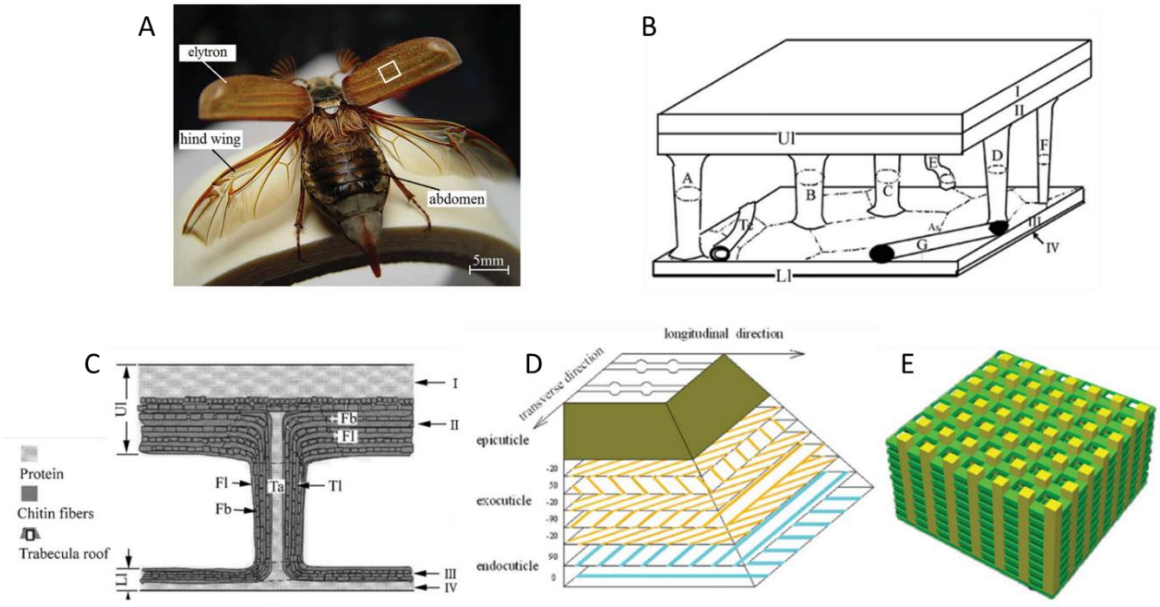

Figure 1. 6. Beetle cuticle structure. (a) Beetle cuticle structure. (A) Optical overview of abdomen, forewings, and hindwings of Cockchafer *Melolontha melolontha*. (B) Models of elytra internal structure. (C) Schematic of microstructural features of the cuticle. (D) Model highlighting variations between successive layers in the cuticle. (E) Schematic of pours structure in the cuticle linked by chitin chains. Adapted From (*43*)**.**

A model system when examining damage resistant composite materials lies in the exoskeletal and elytral structure of *Phloeodes diabolicus*, or how it is colloquially known, the diabolical ironclad beetle. Primarily used as a defense against the environment and predation, the elytra of this organism remain known amongst entomologist for its ability to bend their steel mounting pins and withstand predator strikes. The hardened elytra of *P.*

diabolicus remains an example of compression and penetration resistant biological composites suited for protection against crushing and peaking predators. Terrestrial in nature the Ironclad beetle lacks the ability to fly away from antagonist as it no longer has membranous forewings and has a fused elytron bound by a medial suture (*38*). Lacking any active defenses (advanced musculature, horns, aggressive mandibles, or chemical secretions) after its passive camouflage has failed, the ironclad evolved a fortified cuticle.

Structure-mechanical property relationships remain commonly examined for a variety of insect exoskeletons yet unlike the elytra of the ironclad, these organisms are not able to withstand similarly high compressive events (*47*, *48*). The microstructural variations relating to these mechanical properties have yet to be fully analyzed for the ironclad elytra. Additionally, these mechanical properties rely on variations of ultrastructural features including crosslinking of proteins, crystallinity, and orientation, that remain ordered during development into the adult stage. Previous work has examined ultrastructural features form an entomological point of view presenting possible mechanisms for toughening (*49*). Yet, this work leaves many questions unanswered as it only provides lose sketches of these features and fails to link them to mechanical performance. Studying the structure-mechanical property relationship of this cuticle would yield insights into the fabrication of complex composite architectures that exhibit enhanced toughening. Furthermore, few efforts have been undertaken to fabricate, mimic and validate the mechanical response of biomimetic composites inspired by the elytra of terrestrial beetle.

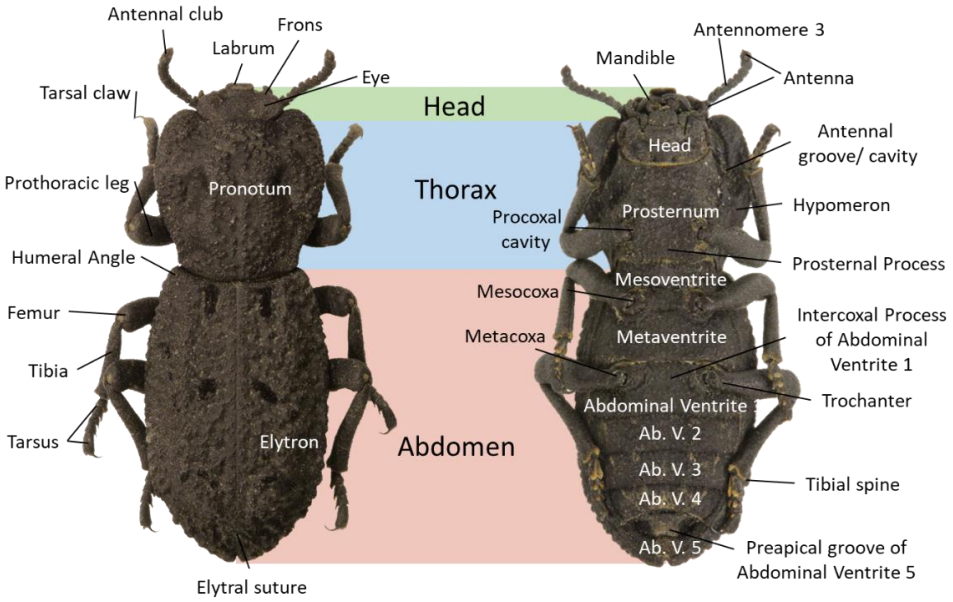

Figure 1. 7. Exoskeleton anatomy of *P. diabolicus.*

The aims of this dissertation are to perform a study of the 1) structure-mechanical property relationship of the compression resistant elytral of the diabolical ironclad beetle, 2) multifunctional nature of the ironclad elytra and its ability to collect transport and store water in an arid climate, 3) structure-mechanical property relationship and evolutionary divergence of flying and terrestrial elytra, and 4) mechanical response of biomimetic composite materials inspired by architecture of arthropod exoskeleton. The study of these biological composites and the mechanical properties driven by ultrastructural features and chemical gradients will provide guidelines for the ordered fabrication and synthesis of organic and inorganic engineering composites. These biomimetic designs will further yield light weight, strong and tough composite materials compared current engineering standards.

Chapter 2: Structure-mechanical property relationships of the ironclad beetle elytra

2.1 Background

Entomological work has extensively identified the phylogeny and ultrastructure of the ironclad beetles of the world (Coleoptera Zopheridae) (*50*–*53*). Utilizing optical microscopy, the author characterized the morphological variations of the beetles to achieve a phylogenetic analysis of the species along with collection data to provide their geographic distribution. More recent work has offered a closer examination of these morphological features providing scanning electron micrographs of the external structure, yet little is known about the mechanical properties of this organism's exoskeleton (*52*, *54*). Primarily focusing on flying relatives, previous work has revealed beetle elytra as multilayered structure divided into an outermost epicuticle followed by the chitin procuticle, encompassing the dense exo- and thicker endocuticle. Developing from imaginal discs and evaginations of the epidermis, the elytra displays a dorsal and ventral cuticle connected by trabecula with a network of hemolymph space (Figure 2.1 C). These structures consist of a hierarchical assembly of alpha-chitin fibers surrounded by a proteinaceous matrix (*45*, *55*). Optical and electron microscopy analysis reveals unit layers (lamellae) organized in a periodic arrangement reminiscent of a spiral pattern or Bouligand pattern of parabolic arcs (Figure 2.1 D, E). Common amongst arthropod cuticles, this architecture provides toughening by deterring crack propagation through the bulk. The proteins within the elytra are heavily crosslinked to stiffen the structure. Electron dispersive x-ray spectroscopy of

the elytra has confirmed a lack of mineral within the cuticle, and is primarily comprised of organic (i.e., C, N and O) [(*56*)]. Further analysis of the microstructure highlights variations between the arrangement of these chitin fibers amongst different families of beetles. Architectures from other beetles show macrofibres of tightly packed parallel unidirectional bundles, balken, that vary in direction with successive layers (Figure 2.1 D). Although the tensile, compressive, and flexural properties of many arthropod cuticles have been selectively studied, details concerning the bulk structure-property relationships and the hierarchical microstructural responses have not been fully examined. Work on Tenebrionoid family encompassing fungus, bark, darkling and blister beetles has provided sketches that highlight variations between interfacial regions connecting the elytron, but little is known about their microstructure or mechanical response (*38*). Therefore, key insight into the mechanisms for distributing stress and the mechanical response due to the variation of these features has yet to be interrogated.

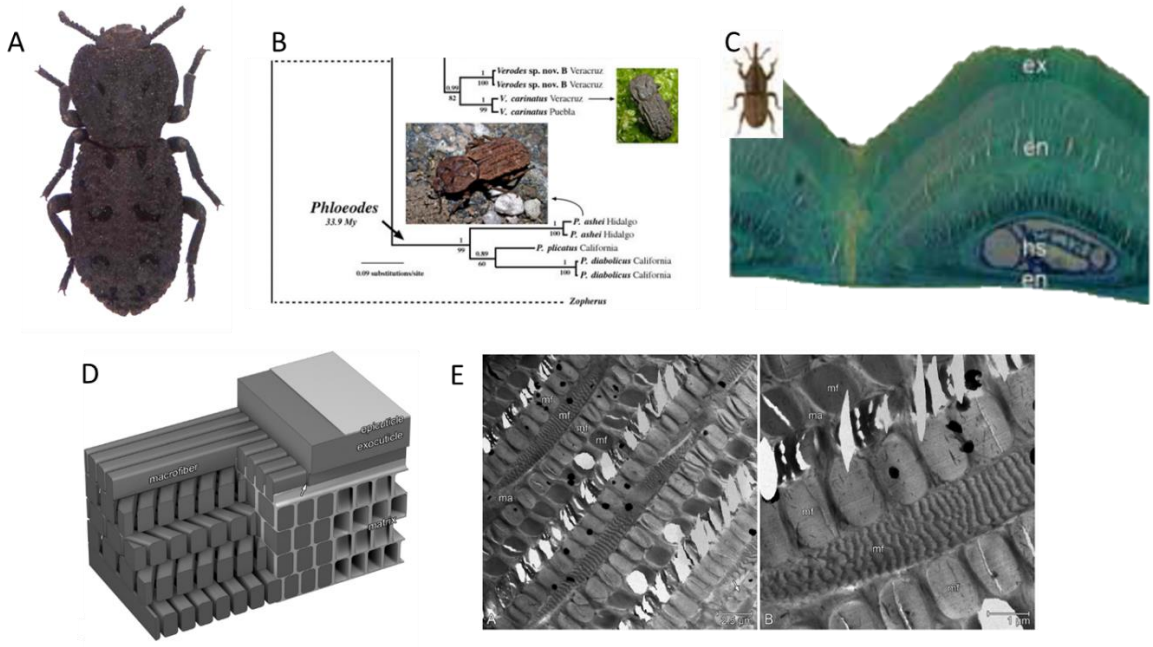

Figure 2. 1. Brief Phylogeny of *P. diabolicus* and microstructure of terrestrial beetles. (A) Optical micrograph of *P. diabolicus* (*50*) (B) Phylogeny of Zopherus highlighting the deviation of genius *Phloeodes* (*57*). (C) Terrestrial weevil stained cross section (*42*)**. D) Model of microstructure highlighting cuticle layers and large macro fibers (*49*). E) TEM of weevil elytra (*49*).**

2.2 Objectives and hypotheses

The objectives of this work are to characterize the structural and compositional features of the diabolical ironclad beetle, measure the resulting mechanical responses that contribute to compression resistance and translate this knowledge to the development of light-weight tough composites. Damaged sections will be interrogated to identify toughening mechanism within the cuticle. To mediate stress convention in the interfacial regions of the elytra, the organism mist incorporates multiscale architectural features within these segments to dissipate energy and ultimately prevent catastrophic fracture.

2.3 Materials and methods

Specimen Handling and Sample Preparation.

Research Specimens. live specimens of *Phloeodes diabolicus* (0.43 ± 0.13g; 21.3 ± 3.7-mm length; 5.3 ± 1.1 mm height) *Asbolus verrucosus, Eleodes grandicollis* and *Cryptoglossa muricata* were acquired from the University of California, Riverside campus and a series of local collectors. Before experimentation, beetles were housed in a terrarium at room temperature (25° C). Elytra were obtained from recently deceased specimens. For optical characterization, samples were embedded in epoxy (System 1618, Polymer Composites, USA) resin, sectioned using a Techcut 4 low speed saw with a diamond blade (Allied), and polished progressively down to a 0.05 µm roughness using diamond abrasive (Allied). Cross sections were obtained in transverse and longitudinal directions. Fractured samples of the elytra were prepared by breaking with forceps.

Organic component analyses. Elytra obtained from *P. diabolicus* and *Trypoxylus dichotomus* were dried at 60°C for 24 hours and were weighed. Lipids were extracted from dried elytra with 1 ml of ethyl ether for 24 hours at room temperature. This treatment was repeated 3 times. After removal of solvent, elytra were dried for 3 hours and were weighed. The elytra were deproteinized using a 1M sodium hydroxide solution for 1 hour at 85°C. This was repeated several times until the protein concentration in the extracted solution was below the detectable limits using a BCA assay. The resulting elytra, which had a white color, were dried for 24 h at 60°C. The weight was determined as the chitin content in the elytra. Lipid content was calculated from the difference of weights between untreated dried elytra and dried elytra after lipid extraction. Protein content was determined from the

difference in weight between dried elytra after lipid extraction and dried deproteinized elytra.

Scanning Electron Microscopy (SEM). Fractured and polished samples were sputter coated with Platinum / Palladium and examined in the SEM (Philips XL 30, CFAMM UCR).

Mechanical Testing. Exoskeletal compression tests were conducted on euthanized and dehydrated samples using a Bose ElectroForce 3200 Series III Test Instrument at a rate of 0.01 mm/ sec between two steel plates. Samples were tested until failure of the exoskeleton (fracture of the suture) and the peak load was measured. Five samples of each beetle were tested.

Compression tests were conducted on selected 2mm cross sections (by using a Techcut 4 low speed saw with a diamond blade (Allied) attained from recently deceased specimens. The sections were distinguished by the varying lateral supports of *P. diabolicus*. Samples from each section were compressed using a Bose ElectroForce 3200 Series III Test Instrument at a rate of 0.01 mm/ sec.

3D Printed Mechanical Testing. Tensile tests were conducted on an Instron 5969 Dual Column Testing System in accordance to adapted ASTM D638 standards and at a rate of 0.05 mm/ sec. 3D printed samples were fabricated using a Formlabs Form 2 stereolithography printer and their proprietary tough resin (TOTL04) at a layer thickness of 0.05 mm with a final part geometry of 40 x 55 x 5 mm. The samples were post-cured under a 405 nm light at 60 °C for 120 min, according to manufacturer specifications.

Mechanical properties for the resin samples were obtained by tensile tests conforming to ASTM D638 standards; (N=5), $E = 1.7 \pm 0.1$ GPa $\sigma = 9 \pm 1.9$ MPa (mean ± SD).

The material properties of the two polymers (i.e., TangoBlack and VeroWhite) used for the fabrication of 3D printed jigsaw puzzle-like specimens were characterized in order to obtain material properties in FE simulations (see section H). The 3D printed samples were fabricated using Connex 350 and cured for a week after the print according to the manufacturer specifications. We carried out tensile tests on dog bone coupon samples made of VeroWhite and TangoBlack in accordance with ASTM D638 and at a rate of 0.05 mm/s, which was deemed to be slow enough to avoid strain rate dependence of the polymers. Since the TangoBlack is used as an adhesive to connect VeroWhite layers in the puzzle-like blades (see section H(4)), we conducted two types of experiments to characterize the fracture properties (i.e., Double Cantilever Beam (DCB) tests and End Notch Flexure tests (ENF)). The DCB sample consists of two VeroWhite rectangular plates with a TangoBlack midplane, acting as the adhesive. The geometry and test setup followed ASTM D5528. Opening forces are applied to the end of the DCB specimen through a special tab that was bonded near the ends of the specimen. The load is applied by controlling the crosshead movement of the MTS tensile testing machine, while the load and delamination length are recorded.

While the DCB samples were used to characterize the mode-I energy release rate, ENF provides the mode-II energy release rate. The ENF samples were 3D printed based on ASTM D7905, and consists of two rectangular, uniform thickness VeroWhite plates with the TangoBlack adhesive as the midplane. The specimen is then subjected to three-

point bending using displacement-control. The results from the load-displacement curves enabled calculation of mode-II energy release rates using an iterative process using finite element analysis to determine the main cohesive properties.

3D Printed Laminated Samples. Tensile tests were conducted on the 3D printed samples of blades inspired from the ironclad beetle macro- and microstructures. 3D printed samples were fabricated using a Connex 350 3D printer with two base materials. The 3D printed samples contain layers of VeroWhite (thickness of 1.2 mm) connected by TangoBlack interfaces (thickness of 0.6 mm). Three different models were developed and tested by varying the angle, θ, at 15°, 25°, 50°. The out of the plane thickness of all samples was equal to 12 mm. The tensile tests were conducted on the MTS Testing System along with Digital Image Correlation (DIC) in accordance with ASTM D638 standards. Test were conducted at a rate of 0.05 mm/ sec for all samples.

Biomimetic Composite Blade Fabrication and Testing. Composite blade samples used a 25° contact angle between segments and were manufactured using unidirectional carbon fiber, 85 grams per square meter (GSM) out of autoclave toughened epoxy pre-impregnated carbon fabric (AX-6201XL-C-85GT700-24" RC34, and AX-6201XL-C-150GT700-24" RC34, Axiom, USA) and a chopped graphite fiber (571-A, Fiberglast, USA) and epoxy core. The layup architecture consisted of 30 layers of unidirectional fiber, circumferentially wrapped around the structure. The final dimensions were 8 x 45 x 49 mm. Five sets of composite blades were fabricated for tensile testing. Samples were cured using the manufactures specified cycle. A female fixture was machined out of Aluminum 6061-T6. Randomly oriented composite blades were fabricated out of 1/4" chopped graphite fiber

(50 volume%, 571-A, Fiberglast, USA) and epoxy (System 1618, Polymer Composites, USA) and cured in a custom mold for consistent dimensions. Polymer blades were fabricated using epoxy resin (System 1618, Polymer Composites, USA) and cured in a custom mold for consistent dimensions. Mechanically fastened samples used Titanium Hi-Lok Pins (HL10VAZ6-3) fastened by Aluminum Hi-Lok Collar (HL79-62024) to secure a quasi-isotropic 3k 13-ply plain weave panel to an Aluminum 6061-T6 plate. All samples were sectioned to meet the dimensional standards with four duplicates of each produced for statistics of mechanical testing and structural characterization.

Tensile testing of composite blades. The tensile tests were conducted on all the samples including epoxy, randomly orientated chopped fibers, chopped strand graphite fibers blade, laminated carbon fibers blade, and Hi-Lok fastener using the MTS tensile testing machine. All the tests were conducted at a rate of 0.01 mm/ sec to satisfy the quasi-static loading condition. The Digital Image Correlation method is also utilized during the experiments to get better insight into the failure mechanism of each system. Tests were continued until the fully separation occurred inside the blades.

Micro Computed Tomography. Micro-Computed Tomography scans were conducted at the Advanced Light Source at Lawrence Berkeley National Laboratory (BL 8.3.2, Berkeley, CA). Samples were imaged (continuous mode, 1025 projections, 180° rotation) using a monochromatic X-ray energy of 17 keV with a 10 mm sample to scintillator distance and a 700 ms exposure. The 1x and 10x objectives were used, resulting in a pixel size of 6.5 μm and 0.65 μm, respectively. Volumes were reconstructed using the Xi cam software developed at the Advanced Light Source facility.

Full specimens were studied using X-ray micro-tomography in a SkyScan 1076 at 250 µA and 40 kV with no Filter. N-Recon Software (Bruker) was used for reconstruction. Scans were visualized using CT Vox (Bruker) and Amira (Thermo Fisher Scientific).

Finite Element Modeling of the Elytra and 3D Laminated Samples.

2D Sections: 2D optical images of a transverse cross section of the DIB showing the medial sutures and the lateral supports were digitized in the finite element software Abaqus for its analysis. The models were meshed using 65217 four node plane strain elements (CPE4 in Abaqus). An elastic-plastic model was assumed for the simulations with a Young's modulus, *E*=11,160 MPa, obtained from nanoindentation; Poisson's ratio, ν = 0.3; and a plasticity power law following $\sigma = \sigma_y\left(E/\sigma_y\right)^{\mu}\varepsilon^{\mu}$, where σ_y and μ were inversely calculated from the experimental data corresponding to 100 and 0.1, respectively. The models were compressed between two rigid analytical surfaces. The contact between the plates and the sections of the elytra was assumed frictionless and rigid (i.e., no penetration is allowed). The bottom surface was assumed fixed, while displacement control was applied to the top surface. Force-displacement curves were obtained by measuring in a reference point located in the top surface. The same model was using for comparing the medial sutures of different beetles. In this case, the medial sutures of the *Cryptoglossa muricata*, *Asbolus verrucosus* and *Eleodes grandicollis*, were digitized using Abaqus and scaled to fit in the cross section of the DIB; the other simulation parameters were kept constant.

3D Model: 3D Micro-Computed Tomography scans of the entire abdomen of the DIB were used to create the 3D CAD geometries and meshed using Amira. Both geometry and meshes were transferred to ABAQUS (*58*) for further analysis. The entire abdomen consists of 1458337 linear tetrahedral elements (C3D4 in ABAQUS). Material is assumed to be elastic with Young's modulus, E=11,160 MPa, and Poisson's ratio ν = 0.3. The abdomen model is then compressed between two rigid analytical surfaces. The bottom surface is fixed, and displacement control is applied to the top surface. The contact between the rigid plates and the abdominal parts was assumed to be frictionless and rigid.

Parametric Blades Analysis: 2D finite element models of the 3D printed blades specimens were developed using ABAQUS. The material is assumed to be elastic-perfectly plastic with Young's modulus of E=1700 MPa, ν =0.22, $\sigma_y = 9$ MPa, and the fracture strain, ε_f =0.35. The material properties for resin were adopted from section (E). For all jigsaw blades, displacement load-control is applied on the top surface of the female part and bottom surface in the male part is fixed against displacements and rotations.

Laminated Samples: A 3D finite element model of jigsaw puzzle-like blade similar to the 3D printed sample was developed for θ = 25° in ABAQUS. The model consists layers of VeroWhite connecting by TangoBlack polymers. The VeroWhite is characterized following the ASTM D638 standards. The TangoBlack polymer is characterized by performing three tests, i) tensile tests, ii) Double Cantilever Beam (DCB) tests using ASTM D5528 to obtain the mode-I properties of TangoBlack, and iii) End Notch Flexure tests (ENF) using ASTM D7905 to characterize the mode II behavior of TangoBlack. By using the force-displacement curves from these experiments and reverse engineering technique

using FE simulations, we were able to obtain the material properties of both polymers. In our simulations, the VeroWhite Polymer is assumed to be elastic-perfectly plastic with Young's modulus, E=950 MPa, ν=0.22, $\sigma_y = 60$ MPa, and fracture strain of ε_f =0.35. The TangoBlack polymer is modeled using the traction-separation law model and the normal stress, $\sigma_{max} = 2.0$ MPa with mode I energy, G_I = 2 *MPa.m* , the shear stress, $\tau_{max} = 0.65$ MPa, with mode-II energy equal to G_{II} = 0.6 *MPa.m*. The boundary and loading conditions are similar to those described in the previous section.

Nano Indentation. Recently deceased samples were embedded in epoxy (System 1618, Polymer Composites, USA) cut to a 5 mm thickness, adhered to a steel AFM puck and polished to .05 µm roughness. Indentation was performed on polished flat cross-sections of the exoskeleton at room temperature using a TI 950 Triboindenter (Hysotron, USA). Detailed indentation maps were preformed using a low load transducer with a diamond cone spherical tip. Eight rows of 50 indents are performed with each indent programed to land on a single bundle of fibers. Test used a 2000 µN force and a load function consisting of a 5 s load, followed by a 2 s hold, and a 5 s unload. Values for reduced elastic modulus and hardness were calculated using the Oliver and Pharr method (*58*). Spatial maps of reduced modulus and hardness were subsequently plotted using the scatter function in MATLAB (MathWorks, USA).

2.4 Results and discussion

2.4.1 Mechanical and structural characterization

In order to assess *P. diabolicus*' resistance to external loads, possibly encountered in its natural habitat, we performed compression tests on its entire exoskeleton and compared the maximum compressive strength to other beetles native to the southern California region (Figure 2.2,). The terrestrial beetles, *Asbolus verrucosus*, *Eleodes grandicollis* and *Cryptoglossa muricata*, were selected for comparison due to similar predation (i.e., via crushing and pecking), defense by playing dead (thanatosis), and habitat (17–20). At the onset of compression, *P. diabolicus* exhibits a change in stiffness from 115 N/mm to 291 N/mm at 0.64 mm displacement (Figure 2.2 C) and fractures at a maximum force of 149 N with an average load of 133 ± 16 N (~39,000 times its body weight), significantly greater than the force an adult human can generate by pressing the thumb and index finger together (i.e., 43.0 ± 18.4 N) (21). In contrast, the other beetles can only withstand an average peak load of less than 68 N and exhibit a diminished strength to weight ratio (Figure 2.2 C inset). A. verrucosus exhibited a similar initial stiffness as P. diabolicus yet fractured at approximately 50% of the strain demonstrated by the ironclad beetle, suggesting a variation in composition and/or design features within the exoskeleton.

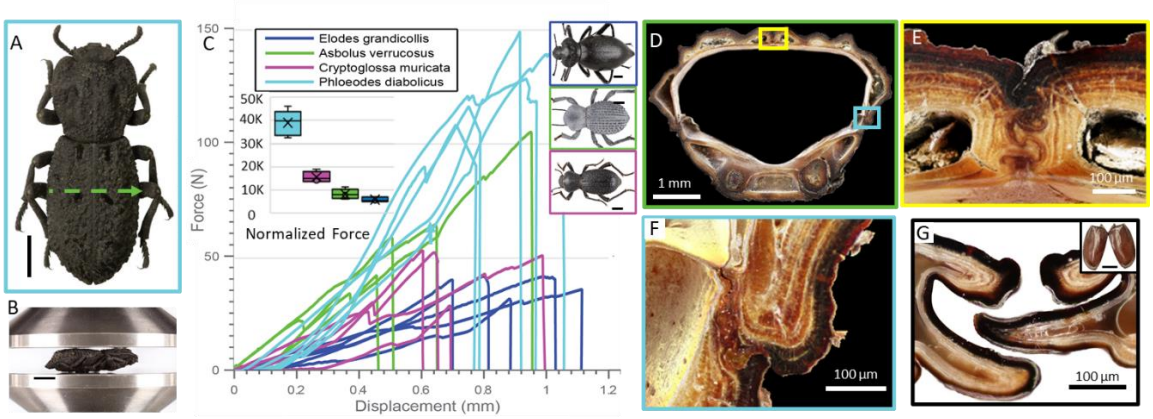

Figure 2. 2. Mechanical properties of terrestrial beetles during compression and unique architectures. (A) Image of Diabolical Ironclad beetle (*P. diabolicus*), Scalebar 5 mm; (B) Image of compression test apparatus, with recently deceased sample mounted between two parallel steel plates, Scalebar 5 mm; (C) Representative force vs. displacement curves for beetles tested. (Inset: Normalized maximum load, (Force / Weight), N=5. Additional beetles tested in compression (top to bottom): *Eleodes grandicollis*, *Asbolus verrucosus* and *Cryptoglossa muricate*, Scalebars 5 mm; (D) Optical micrographs of a transverse cross section (green box) of the diabolical ironclad beetle, highlighting the interfacial architectural regions of interest: lateral supports (blue box) and medial sutures (yellow box). Bottom left: Cross-sectional optical micrograph of suture of a Japanese flying beetle, *Trypoxylus dichotomus* (Inset: elytra of *T. dichotomus*, Scalebar 10 mm).

The exoskeletons of these beetles are non-mineralized and analysis of the organic components from the elytra of P. diabolicus revealed a mixture of approximately 37.9 wt% chitin, 57.4 wt% protein, and 4.7 wt% lipid. In contrast, the elytra from the flying beetle, *Trypoxylus dichotomus*, contained 70.7 wt%, 24.4 wt%, and 4.8 wt% of chitin, protein and lipid, respectively. The relatively high protein content found in the elytra of P. diabolicus is likely correlated to its significantly thicker endocuticle (*42*), which suggests a means for enhanced toughening. Beyond structural enhancement, these proteins play a key role in the elytra morphogenesis (*59*) and microstructural formation (*60*).

Since terrestrial arthropod cuticles are generally comprised of alpha-chitin fibers integrated within a non-mineralized protein matrix (*61–64*), *P. diabolicus*' high

compression resistance likely results from not only the matrix components, but also the assembly of remarkable architectures across multiple length scales (*19*). Cross-sectional analysis of the DIB reveals two distinct features within its exoskeleton: two lateral interfaces connecting/supporting the elytra to the ventral cuticle (Figure 2.2 F), and a medial suture that fuses the two elytron together (Figure 2.2 E). This medial suture consists of interdigitated "jigsaw" arrangements of protruding segments, called blades, that persist along the length of the abdomen. Subsequent evaluation of the DIB's flying ancestors highlights a tongue and groove design (Figure 2.2 G) that enables actuation and flight. Comparative analyses between the sutures and lateral interfaces of multiple terrestrial species reveal significant differences in the thickness and degree of interdigitation, with the greatest number of interlocking elements found in P. diabolicus. However, little insight to variations of these protective interlocking interfaces has been provided (*38*, *65*).

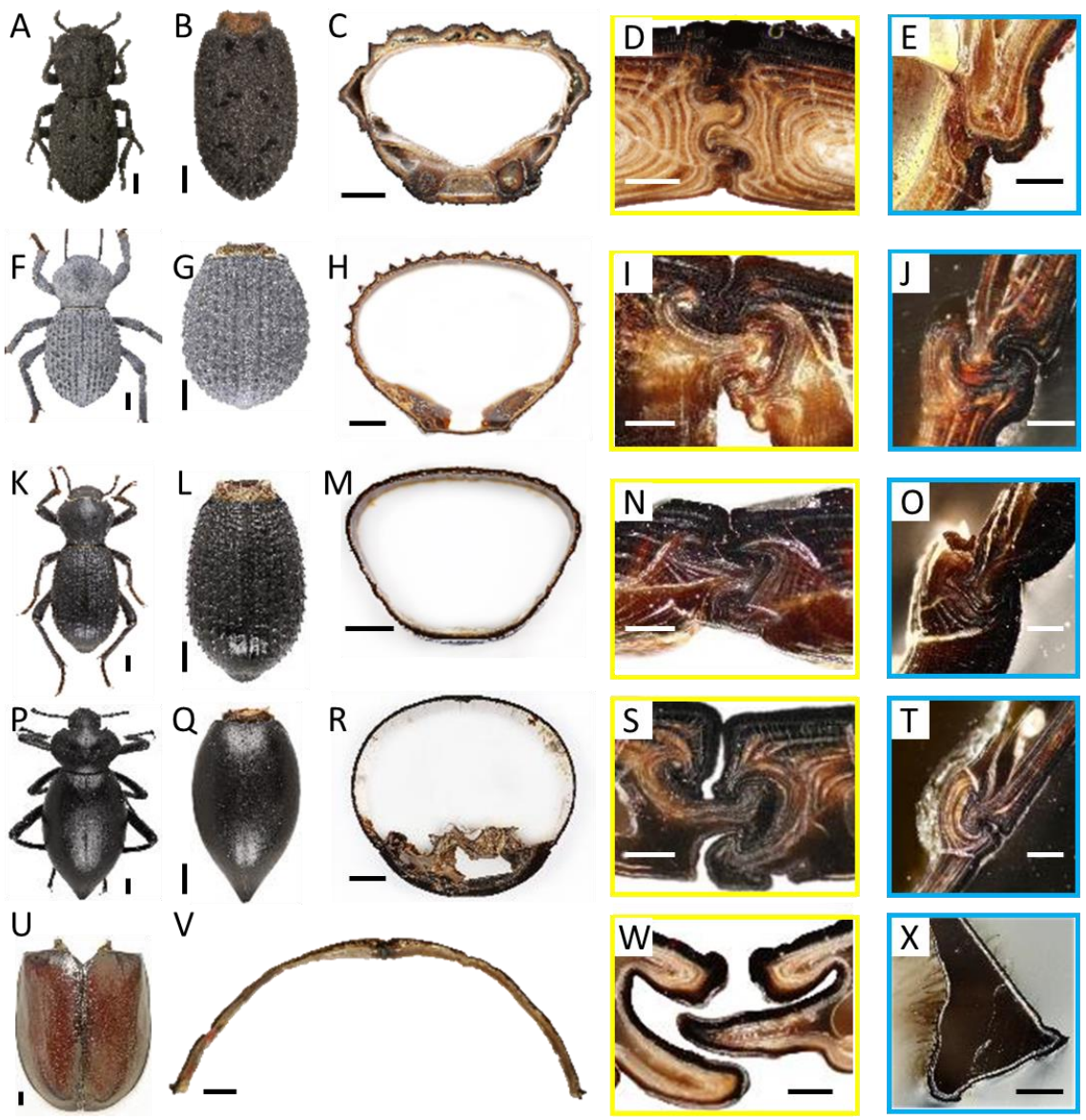

Figure 2. 3. Variations in ultra and microstructure in desert beetles and a flying beetle. Column one, overview of insect, column 2 elytra of organism, column 3 cross section scalebars 1 mm, column 4 suture binding the two elytron scalebars 100 µm, column 5 lateral support interfacing elytra to the ventral cuticle scalebars 100 µm. (top to bottom): *P. diabolicus, Asbolus verrucosus, Cryptoglossa muricate,* and *Eleodes grandicollis, Trypoxylus dichotomus* Scalebars 5 mm.

2.4.2 Elytral and ventral abdomen interfaces

To adapt in terrestrial habitats, these beetles often hide under rocks or squeeze within bark for shelter, not only to survive hot and arid environments, but also to avoid crushing or pecking predation (*66–69*). As such, they must resist external loading without damaging their internal organs (Figure 2.4 A). In fact, analysis of the DIB via Computed Tomography (CT) highlights an air-filled region under the elytra known as the subelytral cavity, located above the abdomen (black space, Figure 2.4 A) (*70, 71*). Subsequent observations of the ironclad's exoskeleton reveal three distinct lateral interfacial architectures that provide support between the elytra and ventral cuticle: interdigitated, latching, and free-standing (Figure 2.4 B). Additional CT-scans highlight that these regions merge seamlessly to one another along the length of the body. In the other terrestrial beetles, a single large interdigitation remains persistent throughout their length (Figure 2.3 J, O, and T).

Simulations of the entire exoskeleton of the DIB under compression suggest that stress is concentrated at the perimeter of the cuticle, with load transferred to the ventral portion through the first and second lateral supports (inset, Figure 2.4 C). Compression tests and finite element (FE) models of isolated sections demonstrate variations in stiffness and maximum displacement between supports (Figure 2.4 C). The first variant incorporates nearly complete sutural interdigitation, joining the elytra to the ventral cuticle and exhibiting the stiffest mechanical response. This highly integrated joint provides maximum protection to the thorax and vital organs in this region by providing a fixed support at the base of the arched elytra to resist bending moments (*72*). Mechanical testing and CT scans

confirm that the maximum cross-sectional displacement before failure occurs is proportional to the height of the subelytral cavity. There is a 40.8% decrease in regional stiffness towards the posterior of the abdomen, concurrent with an average 165% increase in the vertical distance between the elytra and the organs. Subsequently, the second and more posterior support incorporates a latching design that interlocks upon compression, facilitating 40% greater displacement with minimal stress at the interface (Figure 2.4 B middle). In engineered structures, these supports are incorporated in long bridges to allow for thermal expansion and contraction (*72*). Closer inspection of the surfaces of these interfaces reveals an extensive array of 2 µm x 2 µm rod-like elements, known as microtrichia (Figure 2.4 B inset) (*73*). Akin to the hair-like protuberances flying beetles use to arrest their wings, the microtrichia from the diabolical ironclad beetle has a smaller aspect ratio (i.e., 1:1 vs. 1:5 in flying beetles) and likely provide a frictional grip to prevent slip during loading (*74–76*). Supporting no load, the final interfacial variant (the posterior region of elytra) lacks any true mechanical connection between the elytra and ventral cuticle. The results of the 2D FE models of the cuticle cross-section at different lateral support locations (i.e., fully interdigitated, interlocking, and free standing) under compressive load indicates that the stress at lateral interfaces is more than an order of magnitude lower than those in the medial sutures (Figure 2.4 C). A three-dimensional FE model of the cuticle under compressive load provided by our collaborators confirm that the stress significantly drops at the lateral supports for the free-standing variant versus those in the interdigitated case. As such, we surmise that the role of the free-standing and interlocking supports are to enable deflection of the elytra and therefore, increase the

energy absorption during crushing loading of the entire cuticle by providing compliance, while the interdigitated supports are responsible for increasing the stiffness. Models of the entire abdomen, elytra and ventral cuticle under compression highlight the distribution of the principal stresses as the first and second support transfer stress to the ventral cuticle. Further analysis reveals a repetition of the second support at the posterior of the abdomen to prevent collapse of the elytra.

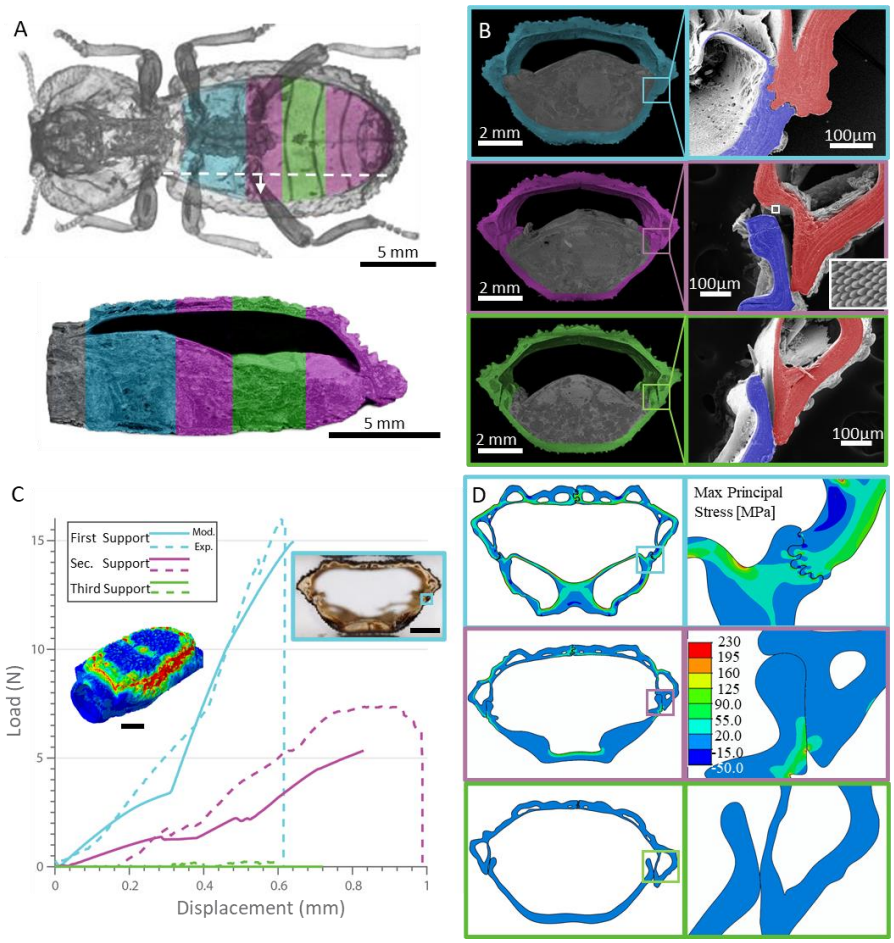

Figure 2. 4. Role of regio-specific and graded lateral supports in compression resistance of beetle. (A) Plan view and longitudinal Computed Tomographic (CT) scans of the diabolical ironclad beetle, highlighting three distinct internal regions with variable spacing between organs and elytra. (B) Cross-sectional CT scans (left) and false colored SEM micrographs (right) highlighting the distinct regional differences in interfaces between the elytra (red) and the ventral cuticle (blue). An obvious gradation is illustrated by comparing the fully interdigitated (light blue), interlocking (magenta), and free standing (green) lateral supports. (C) Compression load vs. displacement curves of fully interdigitated (light blue), interlocking (magenta), and free standing (green) lateral supports. Dashed lines represent experimental results while solid lines represent simulation results. Left inset: FEA Model from CT scan representing stress distribution across surface of elytra under compression. Right inset: Optical image of the fully interdigitated section used for compression test. Scalebars 2 mm. (D) Finite element models of the stress distributions of the varying cross sections and lateral supports during compression, highlighting the ability of the highly interlocked lateral supports to distribute load (modeling results courtesy to David Restrepo Purdue University).

2.4.3 Medial suture: role of blade geometry and number

Repurposed for terrestrial living, the elytra of *P. diabolicus'* adapted ellipsoidal shaped jigsaw blades that provide a mechanically interlocking joint between its two elytron (Figure 2.5 A). Similarly, other terrestrial beetles developed interlocking features that deviate from the tongue and groove geometry observed in their flying ancestors (*38*, *65*). These organisms incorporate a single interlocking blade with a semicircular or triangular geometry to prevent separation of the elytron (*77*). In fact, Nature has adopted both non-interlocking and interlocking sutures as a strategy to regulate energy dissipation at interfaces and improve the mechanical performance of the biological systems. Non-interlocking sutures can be identified by their smooth patterns (*78*), while interlocking sutures provide bound joints such as jigsaw blades (*79*, *80*). FE models incorporating the complex geometry of these interfacial structures in the DIB highlight a relatively uniform stress distribution across the suture due to their elliptical geometry and quantity Figure 2.5 B). In contrast, beetles possessing one prime triangular or semicircular blade show larger Principal stresses located in the necks and contact regions of these interdigitated structures. Geometric analysis of *P. diabolicus*' blades (Figure 2.5 C) reveals a 1.8:1 ratio between the semi-major axis (*b*) and the focal point (*a*), with the primary geometry of each blade parametrically represented as three identical ellipses connected to each other with a specific angle, θ (Figure 2.5C). Here, θ is defined as the angle between the centers of two adjacent ellipses and a horizontal line. In the DIB, the contact angle is 25° between ellipses, yielding a mechanical interlock that prevents separation of elytron under tension (as is seen in circular elements) (*80*). Furthermore, a uniform normal stress distribution at the blade

interfaces enhances maximum tensile and shear stiffness, strength, and fracture toughness (*25*). Thus, we surmise that the elliptical geometry and the number of blades in the medial suture of *P. diabolicus* assist to uniformly distribute stress and prevent rupture between mechanically interlocking elements.

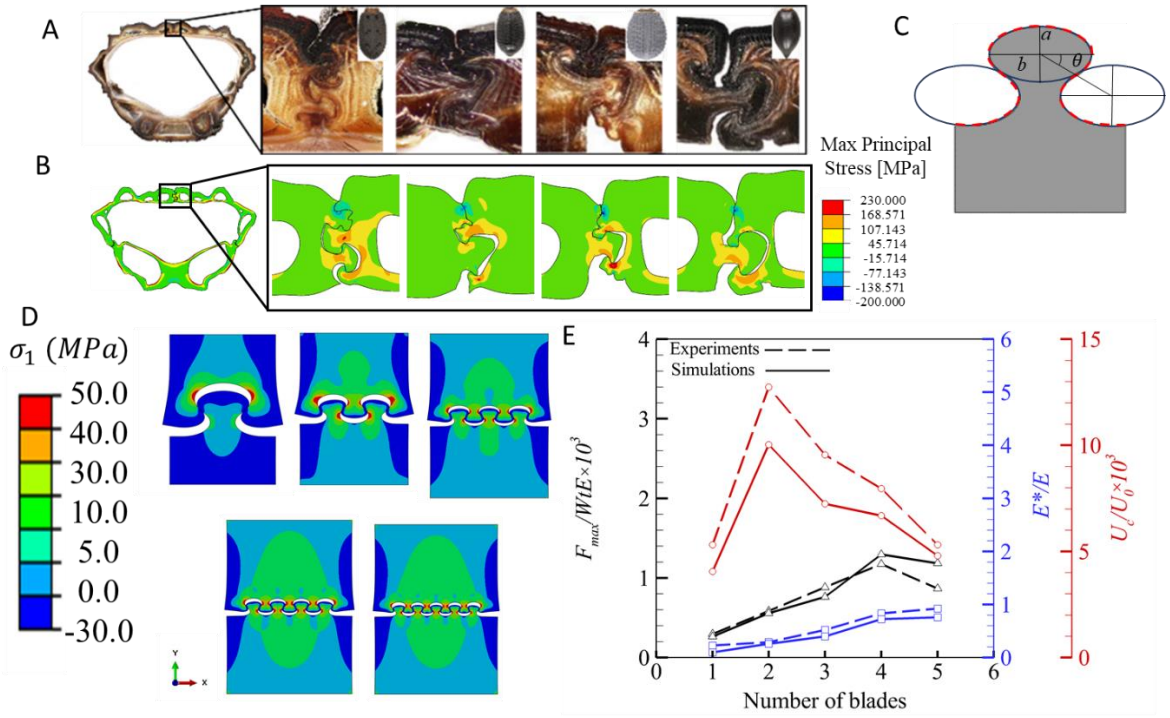

Figure 2. 5. Role of suture blade geometry on mechanical performance. (A) Optical micrographs of cross-sections of elytra from *Phloeodes diabolicus* (first and second from left), *Cryptoglossa muricata, Asbolus verrucosus* and *Eleodes grandicollis*, respectively, showing medial suture structures. (B) Finite element models of the respective beetle sutures from (A), highlighting stress distribution in medial sutures upon compression of cross section. (C) The blade geometry comprised of three identical ellipses. (D) Parametric study samples (Effect of blades geometry and number). Comparison between Normalized Peak load, Stiffness, and Toughness of Experiments and Simulations (modeling results in (B) courtesy to David Restrepo and (D, E) courtesy to Maryam Sadat Hosseini, Purdue University).

Finite element models (courtesy to Maryam Sadat Hosseini, Purdue University) were adopted along with 3D printed prototypes to evaluate variations in stiffness,

toughness, and peak tensile load based on the number and geometry of the sutural blades. To this end, two sets of parametric tests were designed. For the first set of tensile tests, Case 1 (quantity variation), the number of blades (with the naturally observed geometry) was varied from one to five blades (Figure 2.6 A). For Case 2 (capacity variation), the number of blades was increased while keeping the contact area between two elytron constant, resulting in a decrease of feature sizes (Figure 2.5 D).

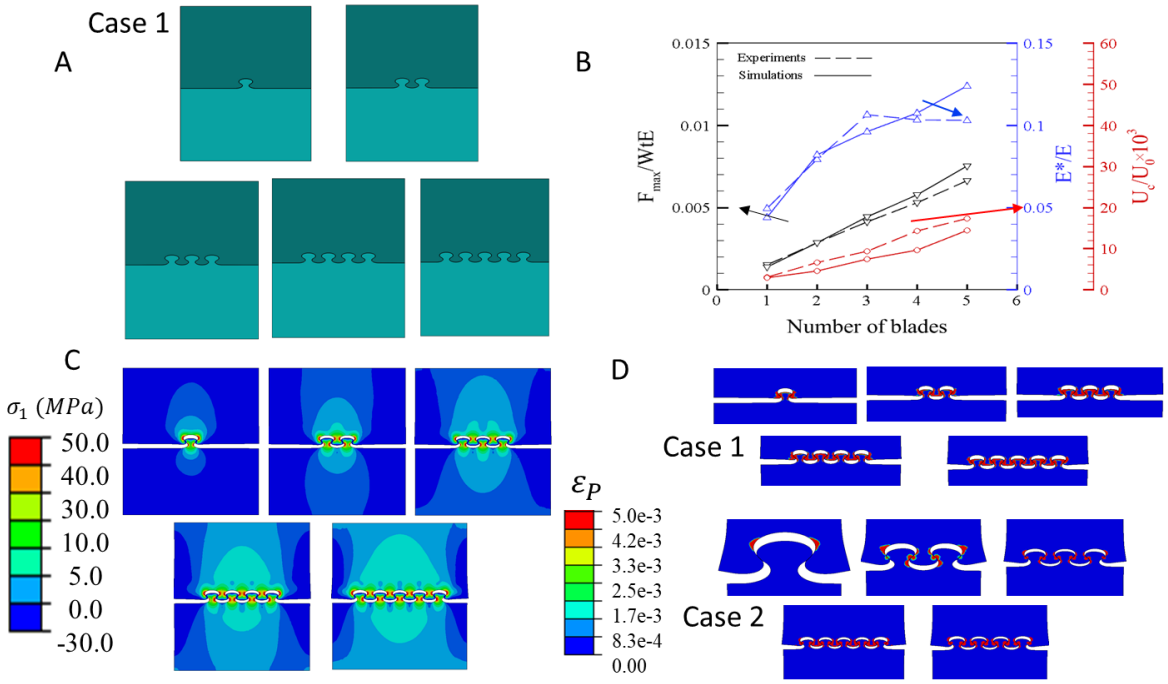

Figure 2. 6. Finite element tensile simulations of Case 1 - Sutural Quantity variation and Case 2 Sutural Capacity variation. (A) Case 1 sample geometry, (B) Comparison between Normalized Peak load, Stiffness, and Toughness of experiments and simulations. (C) Parametric study samples (Effect of blades quantity) showing stress distribution in samples of case 1. (D) Maximum stress in samples from case 1 and 2. (figure and modeling results courtesy to Maryam Sadat Hosseini, Purdue University).

Tensile tests of 3D printed specimens and FE models from Case 1 highlight a linear trend between the number of blades and the mechanical properties (i.e., increased stiffness,

toughness, and normalized peak load) of the medial suture (Figure 2.6 B). Moreover, the FE models suggest that the initial stiffness increases with the number of blades, yet the 3D printed tests result in a stiffness plateau at 3 blades. This could result from air bubbles or uncured resin weakening the relatively small 3D printed blades (*81*). Printing larger samples would most likely circumvent size-related defects resulting in the linear trend in stiffness, toughness, and normalized peak load calculated in the FE models.

The experiments in Case 2 provide insight into the competing mechanisms that exist between length scale and number of blades. Increasing the number of blades, while keeping the contact area constant, leads to a more uniform inelastic strain distribution yielding properties reminiscent of a homogenous material (i.e., higher stiffness at the cost of decreased extensibility, (Figure 2.5 E). Both tensile experiments and corresponding FE models indicate that the maximum toughness is found in sutures with two blades, while the maximum stiffness and peak load occurs in samples with five and four blades, respectively (Figure 2.5 E). As fewer blade elements are utilized, there is a reduction in the inelastic strain concentration within the neck area of the blades. This inelastic strain distribution can explain the transition from ductile-like failure (pull out with damage around the blades) to brittle-like failure (failure around the neck area) by increasing the number of the blades (or reducing the size of the blades). Additionally, a plot of maximum and minimum principal stress vectors indicates that as the number of the blades increases, there is an increase in compressive stress on the blades while a significantly large tensile stress builds within the core of the neck. The compressive stress provides confinement as the number of the blades increases and, therefore, the highest values of stiffness can be expected for the sample with

five blades. As the confinement increases, the tensile stress in the neck region increases. This leads to energy dissipation due to inelastic deformation to a point where brittle fracture at the neck becomes a competing mechanism. The sample with two blades does not display this behavior and thus exhibits the highest toughness.

Furthermore, as the volume of each element decreases, we see enhanced stiffness as the polymer chains are confined by localized contact loads at the bulbous regions (*82*). This results in diminished strain and therefore reduced toughness as the polymer chains are confined to a small volume by the adjacent blades (Figure 2.6 D). Thus, as the quantity of elements over a constant contact area decreases, we see an increase in stiffness and uniform stress distribution.

The analysis of these geometries in the sutures may prove advantageous for joining structures. For example, in wood working, which uses dovetail joints, the geometric variations in the sutures of the DIB results in a greater resistance to being pulled apart and thus may offer new designs that enhance performance of joined structures. This strategy would also be useful in joining of dissimilar engineering materials such as plastics and metals, currently joined by mechanical fastening, which adds weight and introduce stress concentrators that degrade the strength and can lead to fatigue issues, early failure and corrosion.

2.4.4 Medial suture microstructural effects

Although the 3D printed mimics and FE models provide key insight into the stress distribution and interlocking between the sutural elements under tension, they suggest the point of failure within the blades occurs at the necks. When subjected to tensile loading,

the geometry of the blades greatly affects the failure mode of the suture, resulting in either pullout or fracture of the elements (*75*, *83*). Hence, cracks would be expected to nucleate at the center of the neck where stress concentrates in the natural system. However, SEM analysis of the cross-sections of the medial suture from the DIB reveals a laminated architecture, which when placed under a tensile loading, shows failure in the matrix, revealing local delamination (Figure 2.7 B). Charge contrast SEM micrographs highlight these features throughout the blades, suggesting the laminated microstructure facilitates orchestrated stress release (Figure 2.7 C). With increased strain, CT scans highlight significant toughening as there is considerable delamination, with fiber bridging between layers (highlighted by arrows, Figure 2.7 D). In homogenous materials, the neck or the thinnest feature typically experiences failure (*79*). However, the incorporation of a laminated fibrous microstructure results in strain release and energy dissipation via delamination, circumventing catastrophic failure at the neck of the blades.

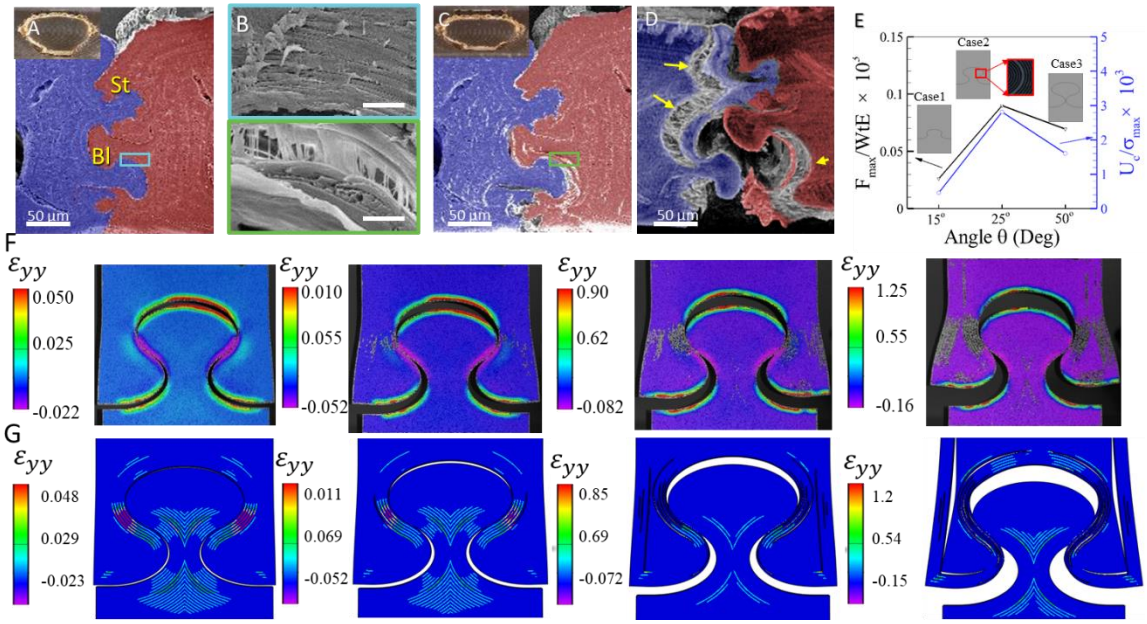

Figure 2. 7. Role of microstructure in the toughening of the medial suture during loading. (A) Uncompressed transverse cross-sectional false colored SEM micrograph of the elytra from *P. diabolicus.* (Bl = Blades and St = Stops). Inset: entire cross section of uncompressed elytra. B) Charge contrast and false colored SEM micrograph of compressed elytra, highlighting crack initiation around blade regions depicted in A. Inset: entire cross section of compressed elytra. (C) Computed tomography reconstruction of fractured suture revealing fiber bridging and delamination in failing structure. (D) SEM micrograph of fractured suture, highlighting multiple failure points. (E) Comparison between normalized peak load and toughness of three printed multilayered cases (angle θ is equal to 10°, 25°, 50° for the three case studies). Lagrangian Strain distribution of 3D printed multilayered case of angle θ equal to 25° under tensile loading, (F) Strain distribution using DIC (Digital Image Correlation), (F) strain distribution in simulations. (figure and modeling results (E, F) courtesy to Maryam Sadat Hosseini, Purdue University).

To understand the role of microstructural features and geometry of the blades, three different "jigsaw" geometries were developed by varying the angle, θ, to 15°, 25° and 50° (Figure 2.8 A) (courtesy to Maryam Sadat Hosseini, Purdue University). In all three cases, the primary aspect ratio of the ellipses are constant and set equal to 1.8:1 (Figure 2.8 B) and the 3D printed jigsaw-shaped blades incorporate the layered architecture that mimics the ironclad beetle laminated microstructure (Methods). Tested in tension, the Lagrangian

strains during loading are presented for all geometries (Figure 2.8 C). The blade representing the DIB (i.e., 25°) demonstrated relatively higher normalized values of peak load and toughness (Figure 2.7 E). Digital Image Correlation (DIC) results confirm pullout of the low angle (i.e., 15°) and nearly circular blade, with no strain or delamination occurring. However, when θ is increased to 25° (i.e., that which is found in the diabolical ironclad beetle), significant strain develops within the blade with subsequent delamination, followed by pullout. Finally, in the highly curved blade (θ = 50°) significant strain is observed at the neck, followed by fracture (with no apparent delamination). Thus, these three different prototypes can confirm the presence of competing mechanisms based on blade geometry to provide maximum interlocking, while preventing localized stresses that would cause failure at the neck. This parametric study highlights the role of delamination to relieve strain, while maximizing the interfacial strength at the suture, revealing a new competing mechanism along with pullout and failure in these jigsaw puzzle-like architectures.

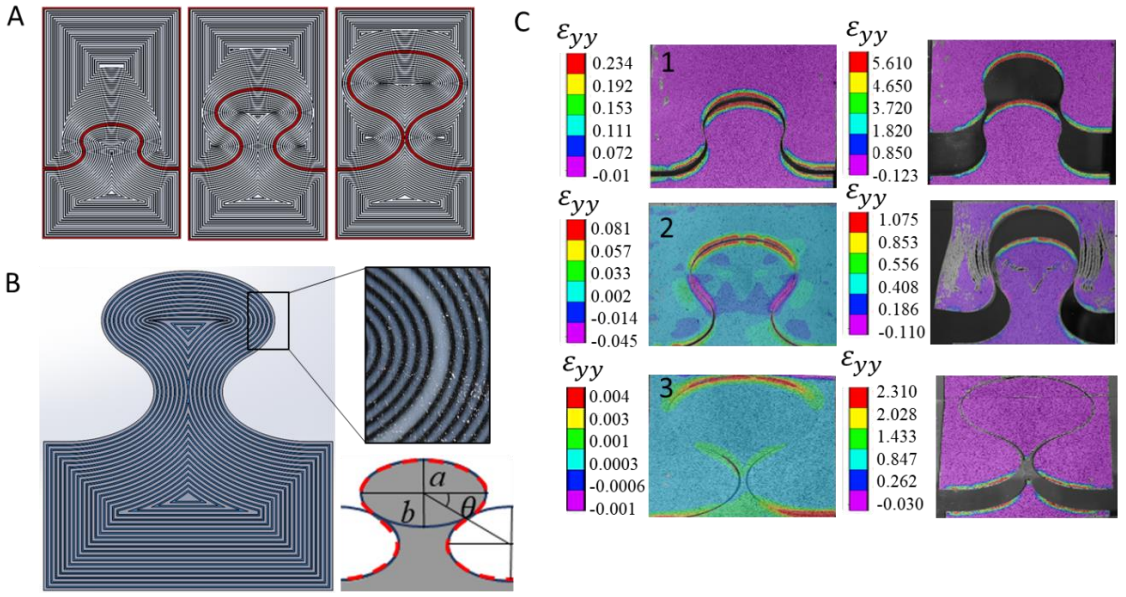

Figure 2. 8. Additive manufactured mimics of laminated blades. (A) Each of the jigsaw blades contains layers (VeroWhite Plus) with a thickness of 1.2 mm. These layers were bonded together using tango black Plus with thickness of 0.6 mm. The zoom box in A presents the architecture inside each blade. The white color presents for VeroWhite layers, while, the bonds between the layers presented in black (Tango black Plus). (C) All three samples were tensile tested along with Digital Image Correlation (DIC) technique to get better insight through the failure mechanisms such as pullout, delamination, and fracture. (figure and modeling results courtesy to Maryam Sadat Hosseini, Purdue University).

Further tensile experiments and FEM for the geometry specific to the DIB highlight the strain distribution and confirm the presence of delamination between layers before pull out (Figure 2.7 F, G). Thus, the presence of the lamellae within the blades provide a mechanism (i.e., delamination) that can be used as an additional toughening mechanism in this jigsaw-like blade geometry, delaying crack formation at thin regions (i.e., neck), relieving stress concentrators, and increasing energy dissipation. Ultimately, this geometry and microstructural combination provides an architectural design to avoid catastrophic

failure and enable survival of the ironclad beetle. With the designs provided by these laminated sutures, the failure can be more predictable, and therefore offer additional safety. Furthermore, this form of mechanical fastening can be applied to automotive or aerospace structures (e.g., landing gear fittings, aircraft control surfaces, flight control actuating systems, and air-intake areas near the engine) (*5*). Typical locations of failure (under both static loading or dynamic fatigue) of the most common mechanical fasteners are directly beneath the head(s) of rivets and at microstructural imperfections (*84*). In fact, the replacement of these fasteners, many of which are very costly, with these bio-inspired suture-like joints will not only improve the performance of the part but will also prolong their lifetime and reduce cost. Utilizing the design inspired from the laminated sutures of the DIB would avoid these failures by increased toughness by spread of damage across the entire joint, thus eliminating catastrophic failure.

To highlight the advantages of this laminated suture, we fabricated a series of biomimetic sutures using the geometry derived from the DIB and with different microstructural features (a lamellar design from the beetle, randomly oriented chopped strand carbon fiber, and a solid polymer-based blade). We subsequently performed tensile tests on these structures and compared their strain distribution and strength, as well as energy dissipation versus a standard aerospace fastener used to join metal (e.g., aluminum)-carbon composite structures (Figure 2.9) (the credit of experimental test goes to Maryam Sadat Hosseini from Purdue University). Similar to the sutures, the composite blades mimicking the DIB successfully joins two materials and exhibits significant strengthening as well as toughening (via delamination with increased strain) (Figure 2.9 A - D). Results

of the tensile tests (Figure 2.9 E) show that the fabricated composite blade is slightly stronger (ca. 19 MPa ± 1.08) than current engineering fasteners (ca. 18 MPa ± 0.73). However, the primary advantage of the lamellar microstructure derived from the suture blades of the DIB versus an aviation fastener is demonstrated in the energy dissipated during displacement (158.0 MPa-mm ± 30.4 vs. 76.5 MPa-mm ± 1.4), an increase of more than 100% in toughness. Digital image contrasting (DIC, Figure 2.9) demonstrates a uniform distribution of stress within the blade with localized delamination providing a means to avoid catastrophic failure at the neck, which is observed in both chop carbon strand and polymer-based blades. The laminated microstructure within the composite blade exhibits a more graceful failure, as delamination within the blade causes the neck of the structure to expand laterally, locking the structure instead of fracturing or narrowing and elongating before failure. Conversely, the Hi-Lok fastener demonstrates a localized strain distribution around the pin connection and results in failure and separation of the plates. Although the natural system possesses a more complex microstructure and interfacial microtrichia to increase friction upon contact, the biomimetic engineered structure offers immediate benefit, reducing weight and increasing toughness (and therefore lifetime) as well as providing predictable failure. There is, however, significant potential for further improvement via tuning material parameters, which is being pursued.

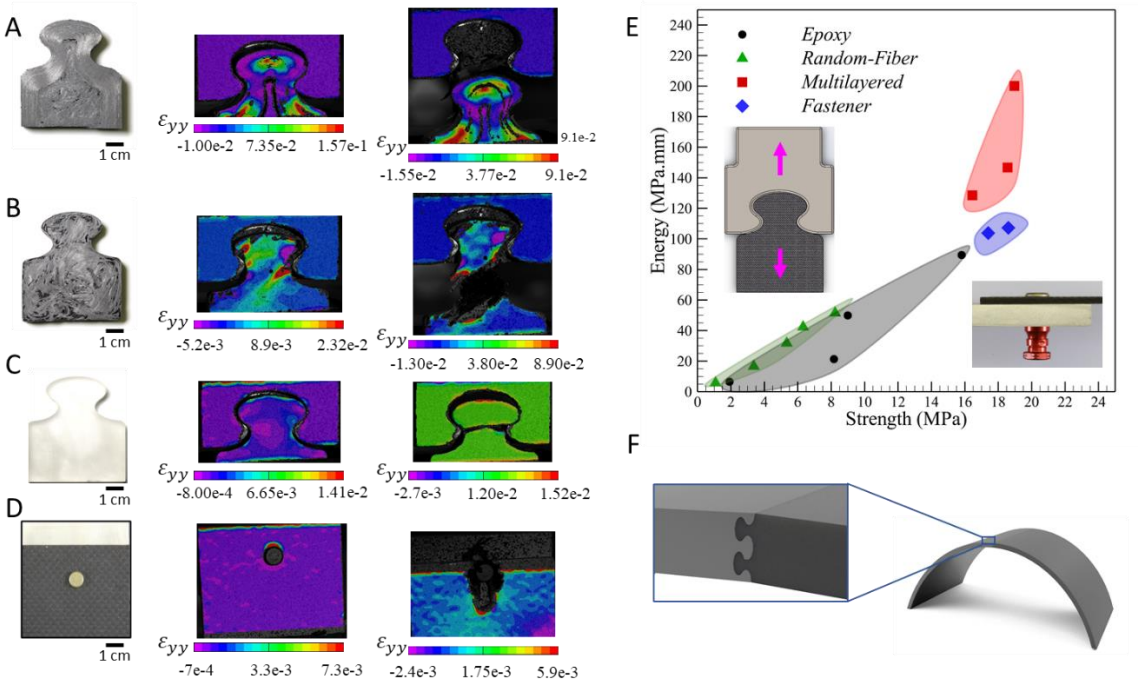

Figure 2. 9. Tensile test of composite blades and engineering fasteners. (A) (Left) Overview image of a composite blade composed of circumferentially laminated prepreg carbon fiber with a chop graphite and epoxy core. (Center) DIC of strained and (Right) fractured blade. (B) Composite blade composed of unoriented chop strand graphite fibers in an epoxy matrix (Left) and DIC of strained (Center) and fractured blade (Right). (C) Epoxy blade (Left) and DIC of strained (Center) and fractured blade (Right). D) Titanium Hi-Lok fastener binding a plane weave carbon fiber epoxy panel to a 6061-aluminum plate (Left) and DIC of strained (Center) and fractured sample (Right). (E) Ashby diagram highlighting the strength vs energy absorbed. (F) Arch structures linked by composite blades applicable to civil engineering or fuselage designs. (Experimental results courtesy to Maryam Sadat Hosseini, Purdue University).

2.4.5 Multifunctional features

In addition to developing a rugged exoskeleton, *P. diabolicus* has adapted to an arid ecosystem. Freeze fractured cross-sectional SEM micrographs (Figure 2.10 B) of the elytra reveal a bouligand-like fibrillar organization (Figure 2.10 C) typically observed in arthropods (*85*) and found to provide significant impact resistance not only in biological structures but also in engineered materials (*86–88*). These bundled layers are joined

together via z-oriented fibers (Figure 2.10 B) within the exocuticle, providing additional compressive strength and toughening (*89*). Closer analysis revealed similarly oriented pore canals which connect to 50 x 25 µm leaf-like setae (Figure 2.10 E) that cover the surface of the elytra. Typically, pore canals in antlers, teeth and bone provide transport pathways for nutrients during structural assembly and development, but have also been known to mechanically arrest crack propagation by blunting the crack tips (*90–93*). Micro CT scans expose a network of pore canals extending from the surface of the exocuticle down into the hemolymph space, a fluid transport cavity responsible for expansion of forewings during final molt stage in beetles (*94*). As it is critical that the organic matrix within the cuticle stay hydrated to maintain toughness, it is likely that these pore canals enable the beetle to maintain resilience (*95*). As discussed earlier, organic analyses of the elytra revealed the presence of lipids (~ 5 wt% lipids). These are likely localized on the elytra surface, preventing desiccation in flying beetles as well as other insects (*96*). In the elytra of *P. diabolicus*, these lipids not only prevent water loss, but may be involved in water accumulation. This may occur by creating appropriate aligned hydrophilic / hydrophobic nano and micro-channels on the setae that drive water towards the pore canal networks in the cuticle (*97*, *98*). Therefore, we suspect the ruffled leaf-like setae wick fluid into a vast network of pore canals, leading to the interconnected volume of canals known as the hemolymph space.

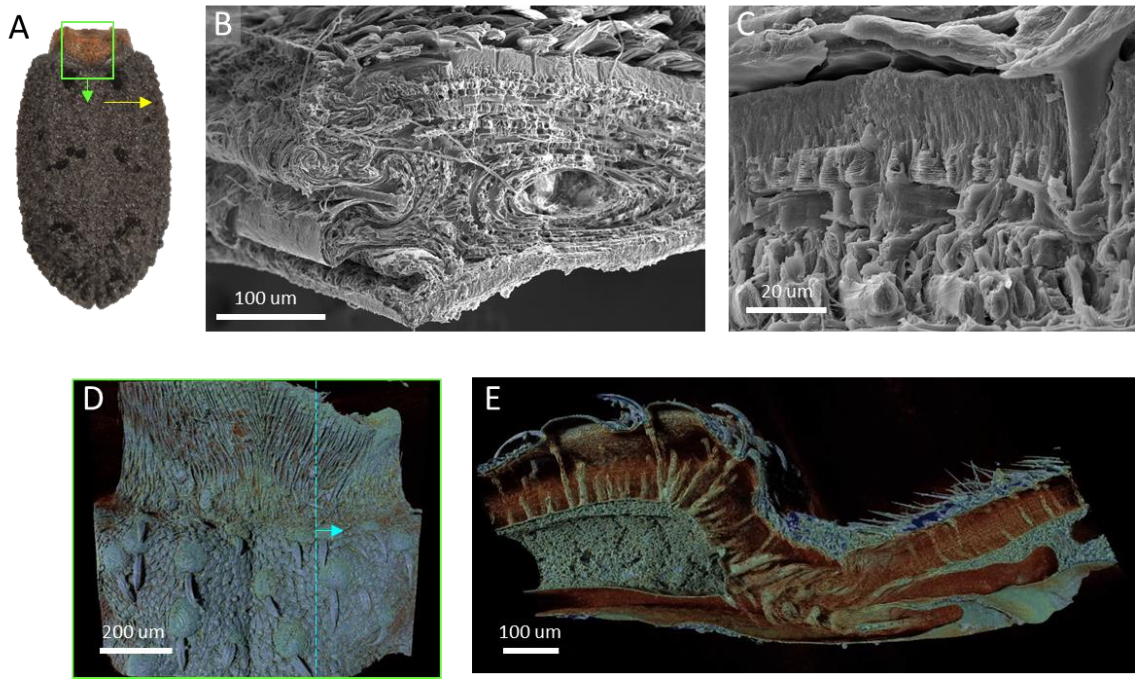

Figure 2. 10. Multifunctional exoskeletal adaptations. (A) Overview optical micrograph of the elytra. B) SEM micrograph of fractured cross section highlighting (C) microstructural features. (D) Computed tomography reconstruction of the elytra. (E) Cross sectional CT reconstruction revealing pore canals connecting the setae and the hemolymph space.

2.5 Conclusions

Our studies reveal unreported interfacial features in the elytra of the diabolical ironclad beetle, *Phloeodes diabolicus*, that assist the organism to withstand predation and other external loads. At the macroscale, the exoskeleton incorporates architecturally varied lateral supports, which yield stiffness gradients that protect vital organs and distribute load uniformly throughout the elytra. Further structural analysis and mechanical characterization of the elytra, coupled with finite element simulations, highlight the benefits of geometry, number and microstructural features of an interdigitated suture. The ellipsoidal geometry and 25° contact angle between these sutural blades provide significant

mechanical interlocking and diminish contact stress as compared to hemispherical and triangular analogues. Furthermore, a laminated microstructure provides toughening through delamination and fiber bridging at critical strains, avoiding catastrophic failure in the neck. A parametric study of blades, combining 3D printing and FE simulations, reveal that two blades provide the greatest toughness, while stress distribution, stiffness and peak load seem to be maximized with four blades. The architectural insights obtained from the study of this non-mineralized composite could be applied as design guidelines for the fabrication of multifunctional, tough and light-weight engineered materials for use in multiple applications. Specifically, biomimetic composites fabricated to mimic the DIB suture geometry and microstructure demonstrated an immediate benefit over aviation fasteners, providing enhanced strength and significant increased toughness. Finally, CT scans highlight the multifunctional nature of this exoskeleton, which contains a network of pore canals that appear to provide structural reinforcement and deter crack propagation, while facilitating paths for fluid transport. The architectural insights obtained from the study of this non-mineralized composite could be applied as design guidelines for the fabrication of multifunctional and tough engineered materials for use in multiple applications.

Chapter 3: Multifunctional adaptations of the ironclad beetle elytra

3.1 Background

Apart from serving as armor after passive (i.e., camouflage and cryptic coloration) and active defenses (i.e., fast predator avoidance behavioral responses) have failed, arthropod exoskeletons possess multifunctional properties. In the 1970's, researchers examined the elytra of the Darkling beetles (Tenebrionidae) that employ different strategies for obtaining water in one of the driest places on earth (*34, 99*). In this study, researchers found that the Namibian desert beetles climbs to the top of sand dunes and orients its abdomen to maximize collection of water from the morning frog. Further studies uncovered that hydrophilic domes on this organism's exoskeleton facilitate a coalescence of water droplets from the humid air. Upon reaching a critical size, these droplets trickle down the hydrophobic sections of the body into the organism's mouth. Results from this study sparked interest into the water collection capabilities of other insects.

The exoskeletal features of the wharf roach *Ligia exotica* serve as another prominent example of passive water transport in nature. This organism incorporates leaflike setae on its legs to harvest water for its survival (*100, 101*). By incorporating a micropattern surface the wharf roach has adapted an uptake mechanism that does not slow down with time as typical seen in the viscous regime of capillary rise. Such an adaptation results from the repetition of unit dynamics in the setae and serves beneficial do long-distance fluid transport. Yet, little is known about the individual setae since it is difficult to quantify the wettability of the microstructures in these minuscule areas and determine

the chemistry of their biological surfaces. Similar leaf like structures have been reported on other insects however their function and chemistry has not been fully explored.

Entomological work has identified leaf like setae on the extremities of terrestrial beetles. Notably, *P. diabolicus* has adapted large granular warts and leaf-like setae coating on the exterior of its exoskeleton (*50*, *52*). Previous works have used these features to classify the organism into distinct taxa and noted their variation amongst the different species. The multifunctional aspects of insect cuticles raise questions about the form and function of these features. Residing in an arid ecosystem and lacking access to a myriad of hydration sources or the agile means to travel to water-rich regions, *P. diabolicus* must tailor its exoskeleton to the climate. Therefore, it is considered that the elytra structure has co-evolved with the terrestrial nature of the organism, resulting in a sophisticated cuticle that collects, transports and stores water. Key details regarding the integration of these mechanisms have not been fully examined however recent works reveled collection and storage adaptations in other elytra.

For adult diving beetles Coleoptera: Dytiscida, the ability to collect and store air remains vital for their survival. Facilitating this, researchers have uncovered the existence of a steal tracheal gill system in the species (*102*). Such adaptation highlights the multifunctional nature of the elytra and the ability to adapt the cuticle for fluid storage. Furthermore, the incorporation of the setae reveals the multifaceted adaption to maximize collection and transport. Yet few studies have examined the internal structural adaptations of beetle elytra.

3.2 Objectives

The objectives of this work are to characterize the structural and compositional features of the diabolical ironclad's elytra that likely contribute to water collection, transport and storage. CT scans will be used to uncover any internal structures that can facilitate transport in the cuticle. Given the organism resides in an arid climate, it remains suspected that the elytra must have adapted a means to collect and store water. Identification of the structure-property relationships will provide insight into the role of external pressures towards the optimization of insect cuticles for multifunctional purposes. Initial hypothesize are that the leaf-like setae assist with water dispersion, while the granular warts facilitate water collection through a hydrophobically tuned surface. I further suspect that the elytra's internal pore canal network and hemolymph space has been repurposed to serve for fluid transport and storage, potentially to hydrate its endocuticle, which provides a robust volume for energy absorption during impact.

3.3 Materials and methods

Specimen Handling and Sample Preparation. Before experimentation, live beetles were housed in a terrarium at room temperature (25° C). Live specimens of *Phloeodes diabolicus* were acquired from the University of California, Riverside campus, and a series of local collectors.

Scanning Electron Microscopy (SEM). Elytra samples were sputter coated with Platinum / Palladium (Cressington 108 Auto, CFAMM UCR) and examined in the SEM (Mira 3, CFAMM UCR).

Exfoliated Setae. Setae was removed from the elytra by partially embedding in embedded in epoxy (System 1618, Polymer Composites, USA) resin and then removing hardened epoxy with forceps.

Contact angle measurements. Contact angle was visualized using a mechanical stage on Bose ElectroForce 3200 Series III Test Instrument and adapted Cannon 5D camera system with a macro lens, and a μL dispensing setup. Contact angle was determined using image processing function in MATLAB (MathWorks, USA).

Micro Computed Tomography. Micro-Computed Tomography scans were conducted at the Advanced Light Source at Lawrence Berkeley National Laboratory (BL 8.3.2, Berkeley, CA). Samples were imaged (continuous mode, 1025 projections, 180° rotation) using a monochromatic X-ray energy of 17 keV with a 10 mm sample to scintillator distance and a 700 ms exposure. The 1x and 10x objectives were used, resulting in a pixel size of 6.5 μm and 0.65 μm, respectively. Volumes were reconstructed using the Xi cam software developed at the Advanced Light Source facility. Scans were visualized using CT Vox (Bruker) and Amira (Thermo Fisher Scientific).

Topography and roughness. Surface Roughness and topography maps were obtained using the scan mode in the VK-X150 (Keyence)3D laser scanning microscope.

Thermal measurements. Recently decided beetle samples were equipped with 30-gauge K type thermocouples to evaluate any variations in temperature. An Omega M-CP-QUADTEMP 2000 data logger was used to record the internal surface and source temperature during the test. Experiment uses a voltage controlled ceramic heat source

raised to 60°C and located one foot away from the sample. Samples were exposed to the heat source for three minutes and the temperatures were recorded.

3.4 Results and discussion

3.4.1 Surface wettability

Optical microscopy was used to examine the macrostructural features of the elytra and abdomen of *P. diabolicus.* As reported in literature the surface was coated in leaf like setae and granular warts. Interrogating the properties of these features, contact angle experiments were conducted to observe the surface wettability of the exoskeleton (Figure 3.1 B, C). A 20 µL droplet of water was placed on the ironclad's elytra. Interestingly, the water did not coalesce, but rather diffused across the elytra. This highlights the diffusive properties of the surface. Control experiments on a native terrestrial beetle, *Eleodes grandicollis,* demonstrated hydrophobic behavior as water droplets did not wet (forming an approximate contact angle of 90°) (Figure 3.1 C). To validate diffusion through capillary action, hydration experiments were performed where *P. diabolicus* was suspended vertically. Water from a 20 µL droplet placed on the base of the abdomen traveled upwards and outwards until it saturated the elytra revealing a wicking process (Figure 3.1 E, F). Therefore, the rough texture, overlapping nature, and chemical composition of surface features on the elytra most likely facilitated water transport via capillary forces. Yet, this raises questions into the mechanism for this transport and how the organism benefits from this adapted.

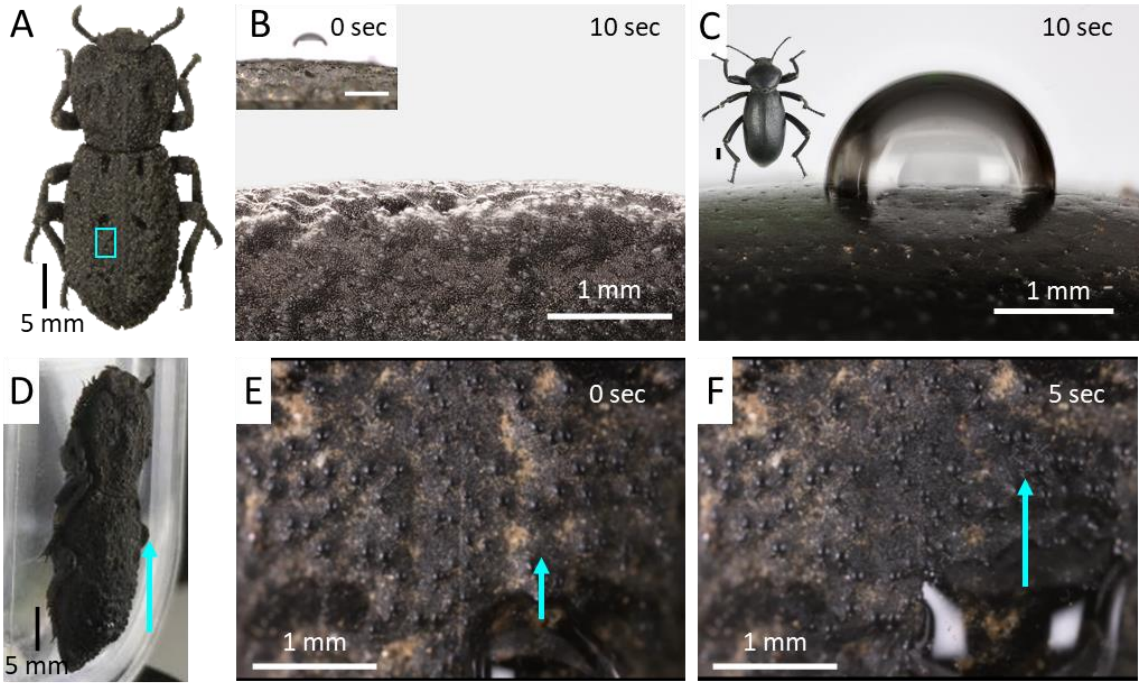

Figure 3. 1. Diffusion of water on the surface of the elytra. (A) Overview of the Diabolical ironclad beetle, *P. diabolicus.* B) Inset, a water droplet is initially placed on the elytra of the ironclad beetle. Diffusion of water 10 seconds after the droplet is placed on the elytra. (C) Control experiment with *E. grandicollis*. (D) Capillarity test setup with *P. diabolicus* suspended vertically as E) a drop of water is placed on the base of the elytra. (F) Water beginning to move upwards due to capillary forces.

3.4.2 Micro and nano-structural characterization

Interrogation of the elytra surface reveals a hierarchical roughness in the region. Laser profilometry scans highlight a 173 µm variation in height between the surface features of the elytra (Figure 3.2 A). This topography resulting in an average SA roughness of 27.6 µm when examining a square mm region. Upon increasing magnification, we can see a second order of topography as the dense overlapping of the setae that have a SA roughness of 6.52 µm for the region (Figure 3.2 A). Examining these features with greater detail, electron microscopy (Figure 3.2 C) highlights 50 µm x 25 µm leaf-like setae coating the surface of the elytra with sporadically located gradual warts that have an elongated 100 µm x 25 µm seta emanating from the base. Further analysis revealed aligned channels ranging from the micron to nanoscale (Figure 3.2 D, C). Folds on the setae remain more prominent towards the posterior section that leads to the base of the structure. This may suggest a structural method for guiding flow or a way to promote transport (*103*, *104*). Additionally, nano ridges on the seta may promote capillary imbibition to allow water to flow into the larger ridges (*105*, *106*).

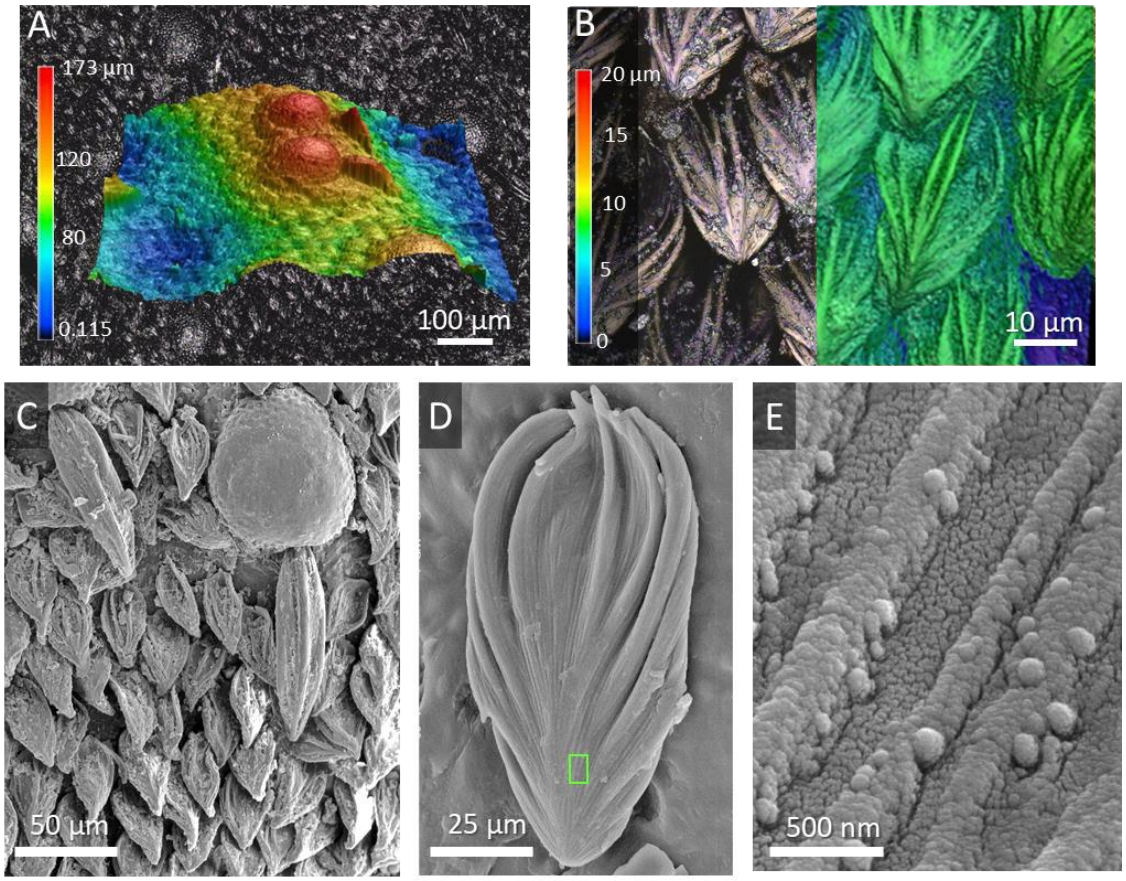

Figure 3. 2. Observations of elytral surface features. A) Laser profilometry scans of the elytra from *P. diabolicus*, highlighting its surface topography. B) Increased magnification scans reveal the localized features of the leaf-like setae. C) SEM of leaf like setae and granular warts coating the exterior of the elytra. D) Micro and E) nano ridges on the surface of the setae that assist to wick water.

CT scans of separate sections of the elytra highlight structural variations that account for a different optical appearance. The dark spots on the elytra result from vertically oriented patches of setae that result in an increased density of features per area (Figure 3.3 A – C). Following the Wenzel equation for wetting, an increasing the roughness on a hydrophobic surface increases its hydrophobic nature. Therefore, the surface setae can disrupt the cohesive forces of water through a structural or chemical process attracting and dissipating the fluid across the elytra (*107*, *108*). To confirm this, we exfoliated the setae through the application and removal of epoxy resin (Figure 3.3 D). Subsequent contact angle experiments show water coalesced on the surface, (contact angle = 61°), highlighting the hydrophilic nature of the underlying epicuticle (likely rich in lipids) and thus suggesting that the setae increase the hydrophilicity through the incorporation of setae with micro-channels and nano, to serve as a fluid dispersion system (*109*). To further examine the surface properties of the elytral features, the large warts were removed and had their surface wettability assessed. Inset in Figure 3.3 E, shows the hydrophilic nature of these features as water was immediately drawn to its surface and maintained a cohesive nature as it was retracted. This further highlights the hydrophilic nature of the elytra but raises questions as to the function of this adaptation.

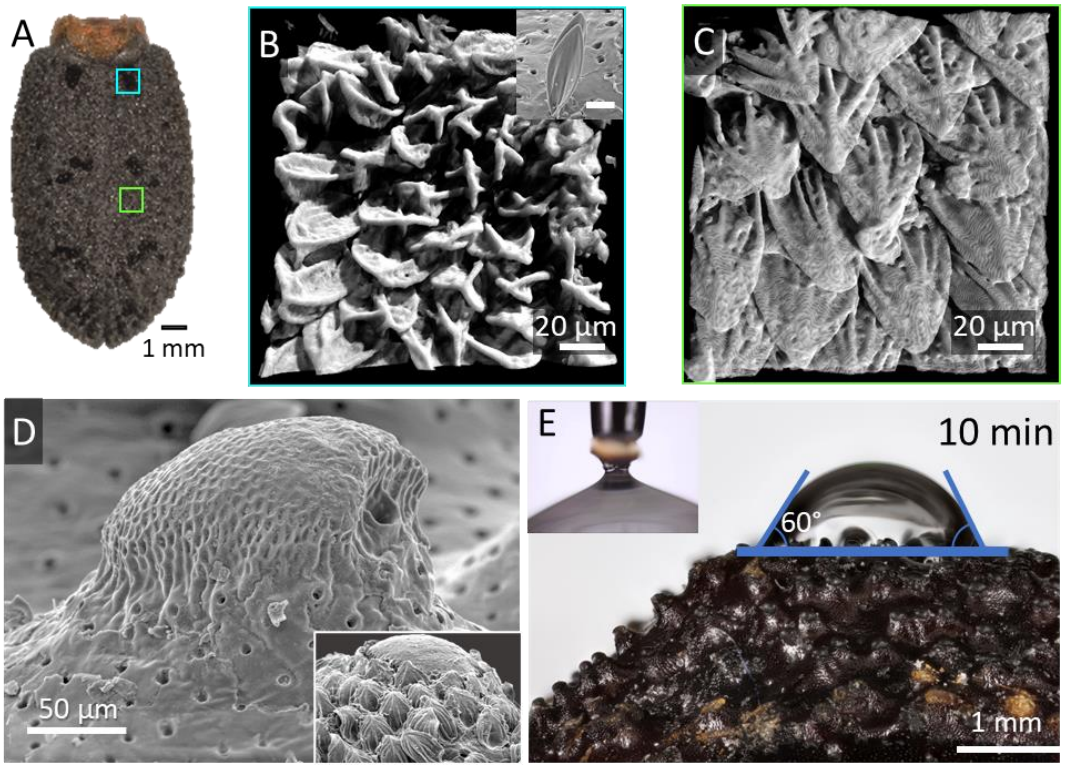

Figure 3. 3. Variation of setae and their effect on wettability. (A) Coronal image of the elytra from *P. diabolicus*. (B) Laser profilometry scans of the elytra, highlighting its complex surface topography. (B) CT reconstruction of the dark patches on the elytra highlighting a vertical orientation and a tighter packing of setae. Inset, SEM micrograph of single vertical setae. Scalebar 20 µm. (C) CT reconstruction of the lighter regions of the elytra showing the horizontal arrangement of the setae. (D) SEM micrograph of an exfoliated elytra (i.e., setae removed) highlighting multiple pores (site of setae base) and the surface roughness of a wart. Inset: elytra before exfoliation. (E) Contact angle experiment on an exfoliated elytra, highlighting its hydrophobic behavior and the loss of its diffusive nature. Inset: image of a native, immobilized wart in direct contact with water, validating the hydrophilic nature of its surface.

3.4.3 Fluid collection and storage

Scanning electron micrographs highlight possible avenues for water transport and storage. Fractured cross section of the elytra (Figure 3.4 A) shows the external setae (green), waxy epicuticle (red), exo and endo cuticle (yellow and blue respectively and hemolymph space (purple). Closer observation of the fractured surface highlights the setae are rooted to the cuticle and remain oriented to seemingly funnel fluid into the structure (Figure 3.4 C, D). Volumetric analysis was employed to understand the connection of these pathways.

Computed Tomography reconstructions of the elytra highlighted not only its fibrous structure, but a dense network of interconnected pores (Figure 3.4 E, F), which are linked to the setae. These pore canals (5 – 7 μm in diameter) extend from the base of the exocuticle down to the hemolymph space (an internal cavity of the elytra that remains from the organism's expansion of its forewings during its final molt to its adult stage) (Figure 3.4 G, H) (*62*, *110*). Typically, these pores provide transport pathways for nutrients during development, but have also been known to mechanically arrest crack propagation by blunting the crack tip through tubule fracture, as seen in antlers, teeth and bone (*111*, *112*). Furthermore, the interconnected pores can enhance the hydration of the endocuticle, which leads to a more mechanically tough structure (*113*). Closer observation of the pore canals reveals a network of branched structures that decrease in diameter as they move towards the exocuticle surface. CT scans reveal the pore canals begin to terminate as they approach the exocuticle (Figure 3.4 F). This may result from the bifurcation of these canals decreasing their feature size or incorporation into the spaces between the fiber bundles.

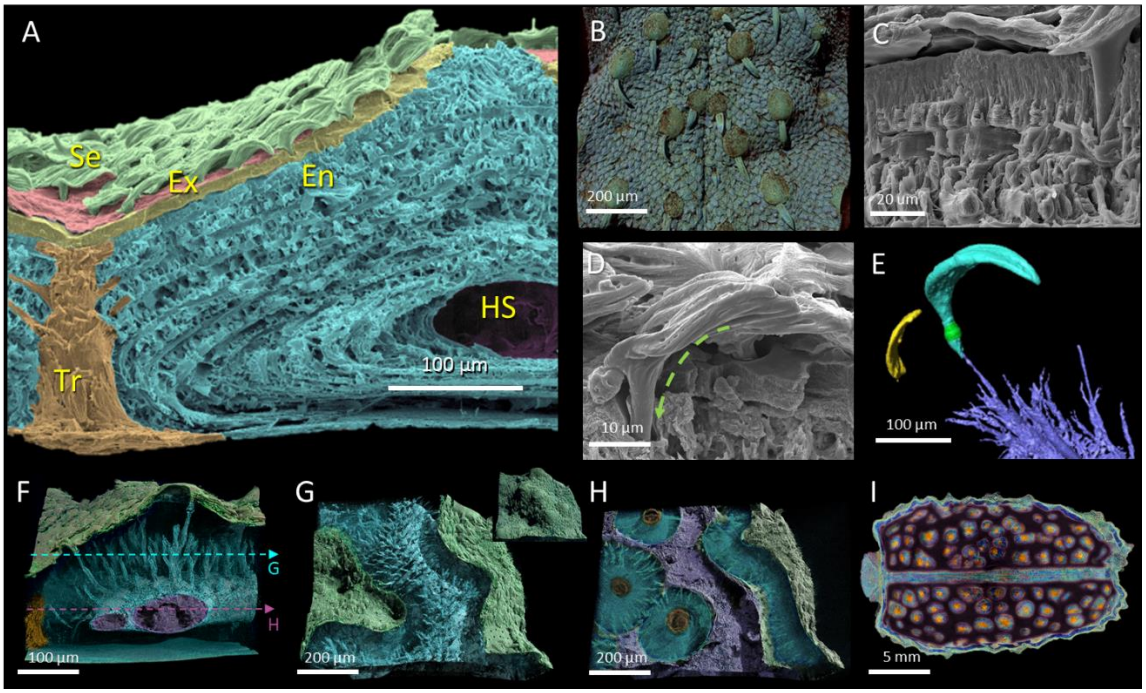

Figure 3. 4. Elytral microstructure and fluid transport pathways. (A) False colored SEM micrograph of fractured cross section of elytra, highlighting leaflike setae (Se, green), epicuticle (red), Exocuticle (Ex, yellow), Endocuticle (En, blue), Trabecula (Tr, orange) and Hemolymph space (HS, purple). (B) CT Reconstruction of elytra surface, highlighting the dense coating of leaf setae and granular warts. (C) SEM micrograph of Macro setae emanating from a wart. (D) SEM of the base of the setae revealing pathway to the pore canals. (E) CT scan of pore canals connected to macro setae. (F) Micro Computed tomography reconstruction of elytra revealing internal pore canal network. G) Coronal section of CT scan, highlighting extensive network of pore canals that lead to (H, I) an internal network of hemolymph space (highlighted in purple).

Further CT analysis highlights an alternative set of pore canals that may be used to expel fluid. Upon examination of the wart we see a set of 500 nm pores that unite to the hemolymph space (Figure 3.5 A). SEM micrographs of the warts highlight the pore exit locations on the surface (Figure 3.5 B). Averaging 0.74 ± 0.36 µm in diameter at the wart surface these pores travel for 80.3 ± 2.66 µm until conglomerating into a 9.85 ± 1.08 pore that connects to the hemolymph space. These branching structures are reminiscent to the roots and branches on a tree that promote fluid motion through transpiration.

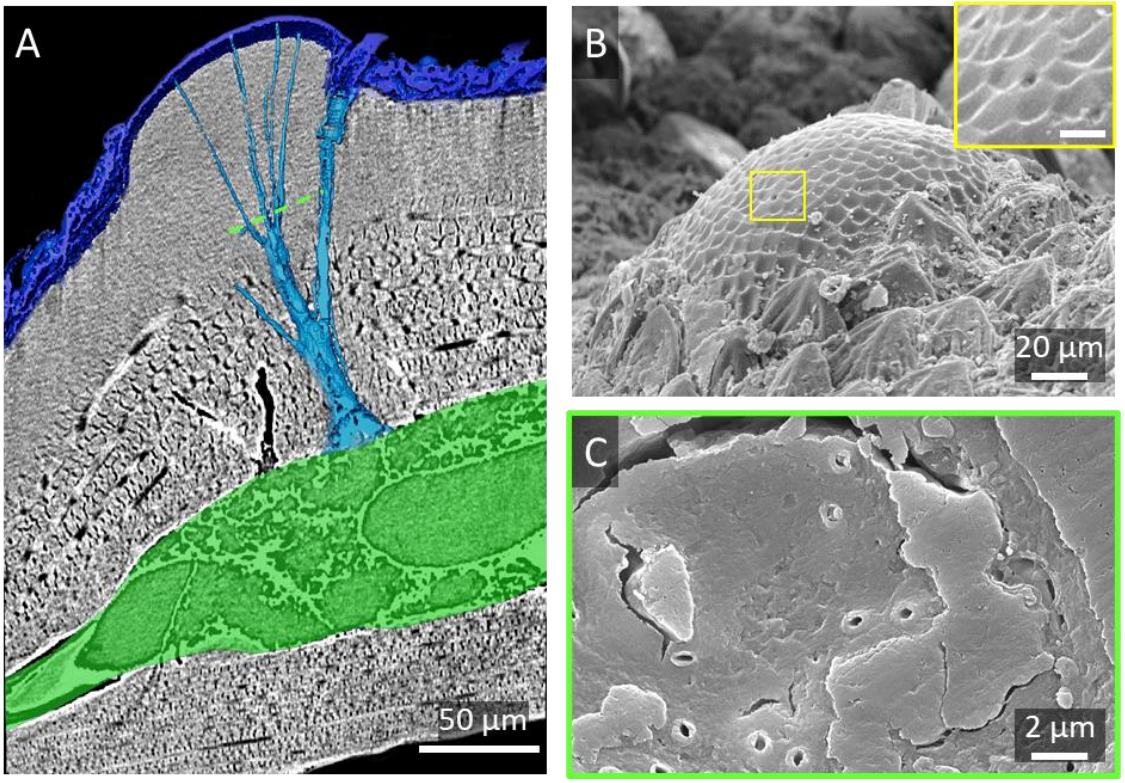

Figure 3. 5. Elytral wart pore canal pathways. (A) CT reconstruction showing branching pathways (Light blue) coming from the hemolymph space (green) and exiting through the wart. (B) SEM micrograph of the termination of the pore canals on the wart surface. Inset scalebar 1µm. (C) Polished coronal section of the wart showing the internal pore canals.

To understand the wetting and mechanical properties of the structure, we conducted a chemical analysis of the elytra. Organic component analyses revealed that chitin, protein, and lipid contents in elytra from *P. diabolicus* were approximately 37.9, 57.4, and 4.7 wt%. The relatively high protein content found in the ironclad's elytra is likely correlated to its significantly thick endocuticle, which enables crush resistance. In the elytra of *P. diabolicus*, lipids may be involved in water accumulation by creating appropriate hydrophilic or hydrophobic surfaces on the leaf-like structure that drive water to a pore canal network within the cuticle (*114*). Therefore, the ruffled leaf-like setae likely wick

fluid across the elytra and into a vast network of pore canals leading to the interconnected volume of canals known as the hemolymph space. Yet, there remains questions about the thermal regulation benefits of these features.

3.4.4 Thermal Regulation

Assessing the value of the ironclads adaptation we examined the internal response to external temperature variations. Serving to regulate internal temperature, some terrestrial beetles possess an arid volume under their elytra and above the abdomen known as the sub-elytral cavity (Figure 3.6 A) (*68*, *115*, *116*). This region was the ideal location to probe for any temperature reduction effect of the elytra. For the temperature experiments, K-type thermocouples were placed on the surface of the elytra and in the sub elytral cavity of the recently deceased beetles. Four recently deceased beetles were tested in this study along with a dried ironclad abdomen. The abdomen of the organisms was heated by a 60 °C ceramic source 3 min while their external and internal temperature were logging. Results from this study showed the hydrated ironclad elytra served as the best thermal barrier providing the greatest variation between the external and internal temperature (Figure 3.6 B). Notably during the test, the elytra of both *E. Grandicollis* and *A. laevis* showed an increase in sheen while under the heat source. This most likely is attributed to the glass transition of their waxy epicuticle regions and may suggest a benefit for the incorporation of leaflike setae to help shade this vital layer.

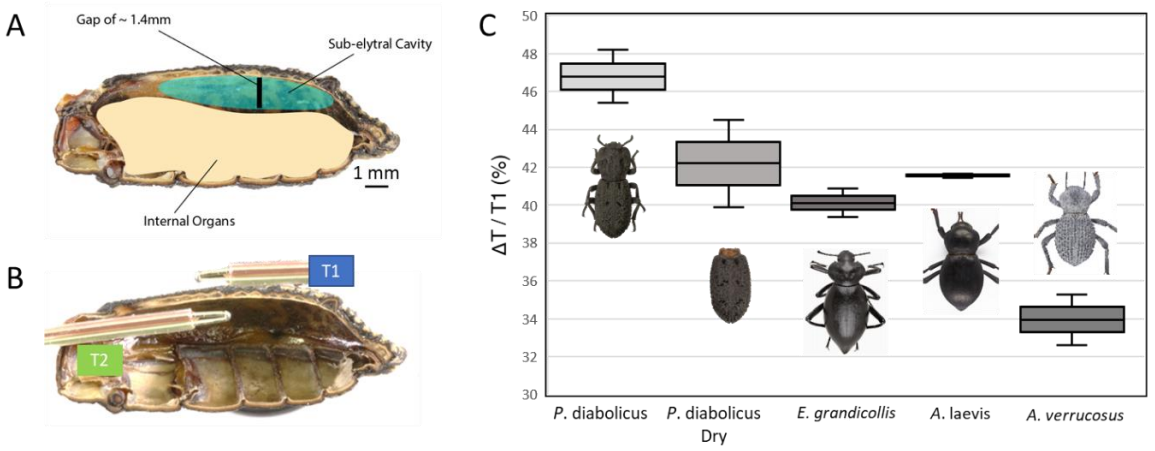

Figure 3. 6. Elytral thermal response. (A) Ironclad cross-sectional schematic highlighting the internal features of the abdomen. (B) Thermal test setup with a vacant cuticle to highlight position of temperature probes. (C) Plot of the change in temperature divided by the external temperature revealing the thermal barrier contribution of the elytra of different beetles.

3.5 Conclusions

In this study we characterize the ultrastructural and microstructural features that allow the ironclad beetle to reside and thrive in an arid climate. The deviation from traditional hair like setae to leaf like structures on this desert beetle raises questions of possible adaptations for water collection and storage based on prior literature (*102*, *103*, *117*, *118*). A super hydrophilic nature on the surface of this elytra was observed, in which a miniscule water droplets were quickly diffused due to hierarchical roughness of the setae. Questions quickly arise as to the role of this super hydrophobic nature and the means for transport. Following the Wenzel equation, we can see the advantage of increasing the roughness in a hydrophilic material as augmenting the surface are increases the hydrophilic nature. Furthermore, the incorporation of the micropatterned features with structural gradients has been shown to allow efficient imbibition of liquids that do not succumb to slowing down over time (*119–121*). The feature overlap and gradients in micro and nano

ridges on the setae likely lead to the complex imbibition on a microscopic scale where the fluid front proceeds to the next seta only after the first is almost saturated resulting in a linear dynamics. Yet, most fluid collection has been normally tailored funneling to the mouth of the organism instead of storing fluid (*103*, *118*).

The resulting adaptation to collect and store water reflects the evolutionary history of this organism and the need to resist desiccation. The need to modify setae and the internal pathway to the hemolymph space has been previously seen in the diving Dytiscida beetles (*122*). This reincorporation of the pore canals used development shows an evolutionary trend for multifunctionality that is further echoed in the elytra of *P. diabolicus*. There remain questions as to the mechanism to prevent desiccation by having open pores in the wart region and the possible use of these features for active cooling. Such features would require and active vale system to regulate output possibly driven by the chemistry of the pore walls.

Overall, there is still many lessons that can be learned from the bounty of diverse elytra of Coleoptera. There remain few works that have explored the multifunctionality of terrestrial beetle elytra and with over one hundred thousand distinct species there remain many model organism to study. Additional studies will benefit from knowledge of phylogeny and the ecological pressures that spurred evolutionary demands ultimately in the hopes that this work may provide insights into the fabrication of multifunctional engineering materials.

Chapter 4: Evolutionary adaptations and structure-mechanical property relationships of beetle elytra

4.1 Background

Insect cuticles have been widely studied for their unique and elegant architectures that fulfill the organism's numerous needs for survival (*51*, *123*). In Coleoptera, a transformation of their delicate forewings into protective hind wings (elytra), which occurred about 350 million years ago (*124*), facilitated an evolutionary diversification that resulted in an excess of 350,000 distinct species including flying, terrestrial and aquatic variants (*125*, *126*). With this wide spread habitation, regional ecological pressures have driven significant architectural deviation among the elytra of different taxa(*42*). Previous examination of beetle elytra have provided insight into mechanical properties and microstructural features of these biological composite that have served as inspiration for engineering structures (*127–129*). However, most of these studies focus on the structure-function relationships of elytra from flying beetles(*50*, *130*) with similar analysis of their terrestrial counterparts limited (*49*, *54*). Currently, there are few studies focusing on the structural and mechanical variations of flying and terrestrial elytra with some recent work providing insights into microstructural variation, yet exclude their mechanical response(*49*). Therefore, to adapt these macro and microstructural features into engineering structures we must understand the structural and mechanical deviation of flying and terrestrial beetles. Here, we investigate two species of beetles from vastly different habitats and describe how variations in their exoskeletal architecture and composition allows them to accommodate and thrive in their relative environments. We focus on the elytra of the

flying beetle, *Trypoxylus dichotomus*, a sap feeding forest dweller inhabiting East Asia, and the terrestrial beetle, *Phloeodes diabolicus*, an oak dwelling fungivore residing on the western coast of North America (*50*, *131*, *132*). Since both *Trypoxylus dichotomus* (rhinoceros beetle) and *Phloeodes diabolicus* (diabolical ironclad beetle), are part of the same suborder, they provide a good opportunity to investigate a comparative structure-function analysis as their robust elytra have been respectively tuned for flight and predator resistance (*124*).

The elytra ultimately serve as a protective cover for the underlying delicate hindwings. Beetles typically actuate their elytra to extend their hindwings and fly yet, for some beetles their elytra have fused to together resulting in an inability for such action. Therefore, these terrestrial variants have adapted alternative responses to deter predation such as active camouflage(*96*), advanced musculature(*133*), chemical secretions(*36*, *134*), aggressive mandibles(*135*), or a robust exocuticle(*75*). For *P. diabolicus*, this inability to actuate its elytra has resulted in a structurally robust cuticle capable of withstanding predator strikes. However for terrestrial and flying beetles the elytra is typically composed of alpha chitin fibrils embedded in a protein matrix(*136*). Therefore, the variation in chemical and structural organization of these composites is critical for performance and allows for diverse mechanical responses in stiffness, strength, and toughness across the same family of organisms (*35*). Details however, pertaining to the relationship between the hierarchical microstructure and chemical composition between flying and terrestrial variants, and their subsequent mechanical responses, has yet to be examined(*137*). Previous work highlighted the robust nature of elytra from the terrestrial *P. diabolicus* and flying *T.*

dichotomus yet, very little has been done to explore the variation in structure property relationships of these terrestrial and flying elytra.

In this study, we endeavor to compare the structure-mechanical property relationships of the elytra from both *T. dichotomus* and *P. diabolicus* by examining the changes in macroscopic architecture, composition, cuticle density and fiber orientation. Comparison between the structure and function of these organisms will not only provide insight into how architectural and compositional factors influence the mechanical response of these biological composites, but also potentially provide design guidelines for next generation composite materials with specific performance requirements.

4.3 Materials and methods

Specimen Handling and Sample Preparation. Before experimentation, live beetles were housed in a terrarium at room temperature (25° C). Live specimens of *Phloeodes diabolicus* were acquired from Riverside, California, and a series of local collectors. Specimens of *Trypoxylus dichotomus* were acquired from collaborators at the entomology department of the Tokyo University of Agriculture and Technology. Elytra from both organisms were obtained from recently deceased specimens. For optical characterization, samples were embedded in an epoxy (System 1618, Polymer Composites, USA) resin, sectioned using a Techcut 4 low speed saw with a diamond blade (Allied), and polished progressively down to a 0.05 μm roughness using a diamond abrasive (Allied). Cross sections were obtained in transverse and longitudinal directions. Fractured samples of the elytra were prepared by breaking with forceps.

Organic component analyses. Elytra obtained from *P. diabolicus* and T. *dichotomus* were dried at 60°C for 24 hours and subsequently weighed. Lipids were extracted from dried elytra by immersion in 1 ml of ethyl ether for 24 hours at room temperature. This treatment was repeated 3 times. After removal of solvent, elytra were air dried for 3 hours at room temperature and were re-weighed. Deproteinization was conducted by placing elytra in a 1M sodium hydroxide solution for 1 hour at 85°C. This process was repeated several times until the protein concentration in the extracted solution was below the detectable limits (as determined using a BCA assay). The resulting elytra, which had turned white, were dried for 24 h at 60°C in air. The final weight was used to determine the chitin content in the elytra. The lipid content was calculated from the mass difference between untreated dried elytra and dried elytra after lipid extraction. Protein content was determined from the mass difference between dried elytra after lipid extraction and dried deproteinized elytra.

Scanning Electron Microscopy (SEM). Fractured and polished samples were sputter coated for 30 seconds (Cressington 108 Auto, CFAMM UCR) with a Platinum / Palladium layer and examined in the SEM (Philips XL 30, CFAMM UCR).

Elytral Mechanical Testing. Three-point bend tests were conducted on newly deceased and dehydrated samples using a Bose ElectroForce 3200 Series III Test Instrument in compliance with ASTM D790 standards. Samples were tested in displacement control mode at a rate of 0.01 mm^{-1} until the maximum strain in the outer surface of the test specimen reached 0.05 mm/mm or a break occurred. Five samples from each species of beetle were tested. Flexural stress (σ) and strain (ε) were calculated using the following equations from ASTM D790:

$$\sigma = \frac{3Fl}{2wt^2}$$

and

$$\varepsilon = \frac{6\delta t}{l^2}$$

Where *F* corresponds to the applied bending force, *l* represents the span length, *w* is the width of the beam, *t* is the thickness of the beam and δ is the midspan deflection.

Tensile tests were conducted on Bose ElectroForce 3200 Series III Test Instrument at a rate of 0.01 mm / sec. and forces were recorded. Specimens were tested under displacement-controlled conditions at a rate of 0.001 mm s-1. The applied load relative to the nominal specimen cross sectional area was used to calculate the engineering stresses.

Micro Computed Tomography. Micro-Computed Tomography scans were conducted at the Advanced Light Source at Lawrence Berkeley National Laboratory (BL 8.3.2, Berkeley, CA). Samples were imaged (continuous mode, 1025 projections, 180° rotation) using a monochromatic X-ray energy of 17 keV with a 10 mm sample to scintillator distance and a 700 ms exposure. The 1x and 10x objectives were used, resulting in a pixel size of 6.5 μm and 0.65 μm, respectively. Volumes were reconstructed using the Xi cam software developed at the Advanced Light Source facility.

Full specimens were studied using X-ray micro-tomography in a SkyScan 1076 at 250 μA and 40 kV with no filter. N-Recon Software (Bruker) was used for reconstruction. Scans were visualized using CT Vox (Bruker) and Amira (Thermo Fisher Scientific).

Indentation. Recently deceased samples were embedded in epoxy (System 1618, Polymer Composites, USA), cured for 16 hours at room temperature, cut to a 5 mm thickness , and adhered to a steel AFM puck using cyanoacrylate adhesive and polished to 0.05 µm roughness using diamond polishing media. Indentation was performed on polished flat cross-sections of the exoskeleton at room temperature using a TI 950 Triboindenter (Hysitron, USA). Detailed indentation maps were performed using a low load transducer with a Berkovich tip. Indentation maps were performed in the regions of interest. Displacement controlled tests were performed using a 300 nm depth and a load function consisting of a 5 s load, followed by a 2 s hold, and a 5 s unload. Values for reduced elastic modulus and hardness were calculated using the Oliver and Pharr method (*58*). Spatial maps of reduced modulus and hardness were subsequently plotted using the scatter function in MATLAB (MathWorks, USA).

Fourier Transformed Infrared Spectroscopy. FTIR spectroscopy was performed using an Agilent Cary 620 FTIR Microscope. Samples were scanned from 800 - 4000cm^{-1} with 128 scans in a 64x64 micron map. Spectra were processed using Resolutions Pro FTIR Software and MATLAB.

Fiber-reinforced composites processing. Reinforcement used in the composites consisted of dry unidirectional 12K carbon fiber sheets with areal weights of 3.7 $oz./yd.^2$ (ACP Composites, Inc., USA). The non-woven unidirectional fibers are held in position by a fine spider web of polymer fibrils that coat the surface. Two-part epoxy (Max CLR, Polymer Composites, Inc., USA) (modulus of 12.88 MPa) and urethane (TAP Quick-Cast, TAP Plastics, USA) resins were used as the matrix materials (modulus of 7.86 MPa). Three

different helicoidal panels, featuring continuous inter-ply rotation angles of 7.5°, 15°, and 30°, as well as one quasi-isotropic control panel, which features 0°, ±45°, and 90° ply orientations, were fabricated for each of the two unique reinforcement-matrix composite combinations, yielding 8 unique composite designs. Three sets of unique composite panel, each measuring approximately 215 mm long by 215 mm wide, were fabricated, from which two test coupons, each measuring approximately 102 mm long by 152 mm wide, were obtained.

All composites were fabricated using a wet layup technique, in which dry reinforcement was laid down while wet resin was deposited and squeegeed across the fiber surface. This process was repeated layer-by-layer until all plies were laid up. The wet laminates were placed on top of a layer of non-perforated release film and then covered with a layer of nylon release peel ply and a layer of breather cloth (Fiberglast Developments Corp., USA). The panels were then vacuum-bagged (<25 in. Hg) and cured in an oven at 60°C for 3 hours. After curing, test coupons measuring approximately 102 mm long by 152 mm wide were machined from the composite panels using a waterjet.

Drop weight impact testing. Prior to testing, the dimensions (thickness and width) of all composite test specimens were measured in multiple areas using calipers, averaged, and recorded. Impact testing was performed in accordance with ASTM D7136 [34], using an instrumented drop weight impact testing system (Dynatup, Instron, USA) equipped with hemispherical indenter tip. For the instrumented drop tower test, the striker was equipped with a load cell to record force as a function of time during the impact event. The kinetic energy of the impactor just before it contacts the specimen is defined as the impact energy

E and remains as the energy transferred into the composite/holder. The drop height and mass were adjusted to deliver an impact energy of 90 J. During testing, test specimens were fixed in place to a rigid steel base, with a 76 mm x 127 mm rectangular hole in the center, using toggle clamps at the four corners. The energy transferred to the composite / holder system is measured by the difference in kinetic and potential energy of the striker from initial to final contact. The governing equations are defined by ASTM D7136/D7136M [34]. After impact, the dent depth of each test specimen was measured using a depth gauge and recorded. The energy transferred to the composite/ holder system was measured by the difference in kinetic and potential energy of the striker from initial to final based on the equation set forth by ASTM D7136/D7136M.

4.4 Results and discussion

4.4.1 Optical microscopy and morphological features of elytra

Initial observations (Figure 4.1 A, F) reveal that the elytra of *P. diabolicus* is significantly smaller and more elongated (15.3 ± 1.4 mm long by 8.5 ± 1.3 mm wide) relative to that of *T. dichotomus* (30.6 ± 1.2 long by 25.3 ± 2.1 mm wide) for *T. dichotomus*. Laser profilometry scans of the elytra surface of *T. dichotomus* (Figure 4.1 B) reveals a relatively smooth (roughness of 9.77± 2.47μm) and shiny surface with a sparse coating of setae. This smooth and waxy-looking coating prevents excess moisture from condensing on its surface and deterring flight(*95, 138*). Conversely, the elytra of *P. diabolicus* that has a higher degree of topography with dull, matt-like appearance and a roughness of (27.26 ± 2.77μm). This is due to an extensive coating of leaf-like setae and large tubercles which

may serve as storage for nutritive material(*139*). These exterior setae can also serve as camouflage as the dark coloration matches with the appearance of small rocks and bark. Furthermore, the elevated topography likely assists in distributing any biting or pecking forces from predators, similar to how arches or domes distribute normal forces. The addition of undulations for load dissipation has been observed in other arthropod exocuticles such as the carinae in the telson of the mantis shrimp(*140*).

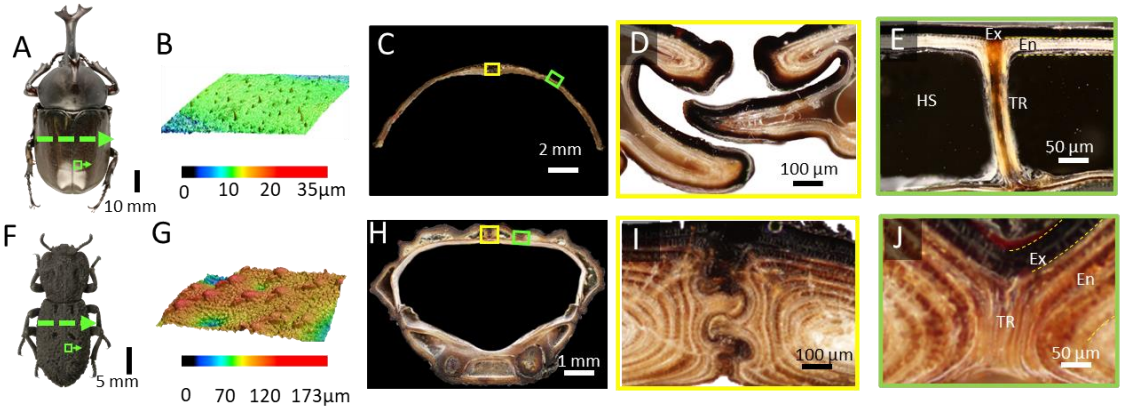

Figure 4. 1. Overview and cross-sectional exoskeletal features of the flying, *T. dichotomus* and terrestrial, *P. diabolicus* A) Optical micrograph (coronal perspective). B) Laser profilometry scan of the relatively smooth elytra surface. C) Polished transverse cross section highlighting D) the medial suture (yellow box) and E) bulk elytra showing a cross section of a trabeculae (green box). F) Coronal optical micrograph. G) Laser profilometry scan of the elytra surface. H) Polished transverse cross section highlighting I) the medial suture (yellow box), J) trabecula cross section and bulk elytra (green box).

To observe the internal architectural features from both elytra, polished transverse cross sections were prepared and investigated with optical microscopy. Figure 4.1 C, H, shows the cross sections from *T. dichotomus* and *P. diabolicus* while highlighting distinctions between two key elytral regions: the medial suture (D, I) and bulk cuticle (E, J) respectively. The bulk region of the elytra encompasses the exocuticle, endocuticle, trabecula and hemolymph space, while the medial suture spans the length of the abdomen and represents the interface between the hardened forewings joining the elytron(*38*). For

T. dichotomus the suture adopts a rectangular geometry of interfacing protrusions deemed blades that facilitate actuation and flight, while the terrestrial *P. diabolicus* has bulbous interlocking blades that resist separation. Similarly, the interfacial regions between the elytra and the ventral cuticle in *P. diabolicus* are significantly interlocked to facilitate load distribution through the exoskeleton (Nature Paper). In contrast, there is no interlocking between the elytra and the abdomen in *T. dichotomus* since this region separates from the abdomen to facilitate actuation. Previous work studying these lateral interfaces in flying beetles and found the incorporation of large aspect ratio setae to dampen motion upon closing of the forewings (*128*). Examination of the bulk region shows the relatively thin nature of the flying elytra (170 ± 31.0 μm, Figure 4.1 E) compared to that of *P. diabolicus* (253 ± 68.9 μm, Figure 4.1 J). Further analysis reveals similar construction as the darker exocuticle (Ex) and a lighter endocuticle (En) connected to a columnar structure (trabecula) that separates the dorsal and ventral regions of the elytra. This separation enables the formation of large void regions (hemolymph space, HS) created by the loss of hemolymph after resorption (*60*). The function of this HS is to provide nutrients during development and inflate the elytra after eclosion from its pupal state, (*60*, *141*).

4.4.2 Ultrastructural analysis

Micro computed tomography (μ-CT) reconstructions of both elytra highlight internal structural features of these biocomposites. CT scans of *P. diabolicus* reveal a network of pore canals in the dorsal cuticle that lead into the hemolymph space, to maintain hydration and enhance toughness (*35*, *142*, *143*). Similar features are seen in the elytra of

flying beetles but may be a remnant from development (*62*, *63*). Analyzing the volume of the hemolymph space we see this region encompasses 55% of the volume in the elytra of *T. dichotomus* while only occupying 11% in that of *P. diabolicus*. The empty nature of the elytra results from a thin endocuticle and a large separation of the dorsal and ventral regions of the elytra facilitated by the trabecula (Figure 4.2 B). This separation increases flexural stiffness of the elytra while maintaining a high strength to weigh ratio (*144*). Examining the distribution of trabecula we see a spacing of 402 um ± 0.12 um in the elytra of *T. dichotomus* and a larger spacing of 478 um ± 0.13 um for *P. diabolicus*. Closer observation of these trabecula reveals flared nature to the structures induced by a greater number of wrapped endocuticle layers. Like engineering structures, a flared nature at the top of columns allows for a greater spacing between support beams (*145*). An examination of the 2-dimensional geometrical arrangement of these columnar supports uncovers their triangular arrangement in the elytra Figure 4.2 E, F. Triangular distributions such as this may facilitate the natural curvature of the elytra while maximizing its structural rigidity (*146*, *147*).

Chemical analysis of the elytra of *P. diabolicus* revealed a mixture of approximately 32.6 wt% chitin, 52.2 wt% protein, and 15.1 wt% lipid. In contrast, the elytra from the flying beetle, *Trypoxylus dichotomus*, contained 42.0 wt%, 43.4 wt%, and 15.0 wt% of chitin, protein and lipid, respectively. The relatively high protein content found in the elytra of *P. diabolicus* is likely correlated to its significantly thicker endocuticle as well as the amount of matrix between chitin fibrils(*43*), which not only plays a key role in the elytra morphogenesis[16] and microstructural formation[17], but also enables

significant energy absorption. Unlike crustaceans, which add mineral to their cuticles to provide strength, stiffness and hardness, arthropods (e.g., insects), rely on the chemical modification of proteins (e.g., tanning/sclerotization) to stiffen and harden the exoskeleton(*148*) (see Nanoindentation section below). The degree of this cross-linking is directly correlated to the modulus of the cuticle(*149*).

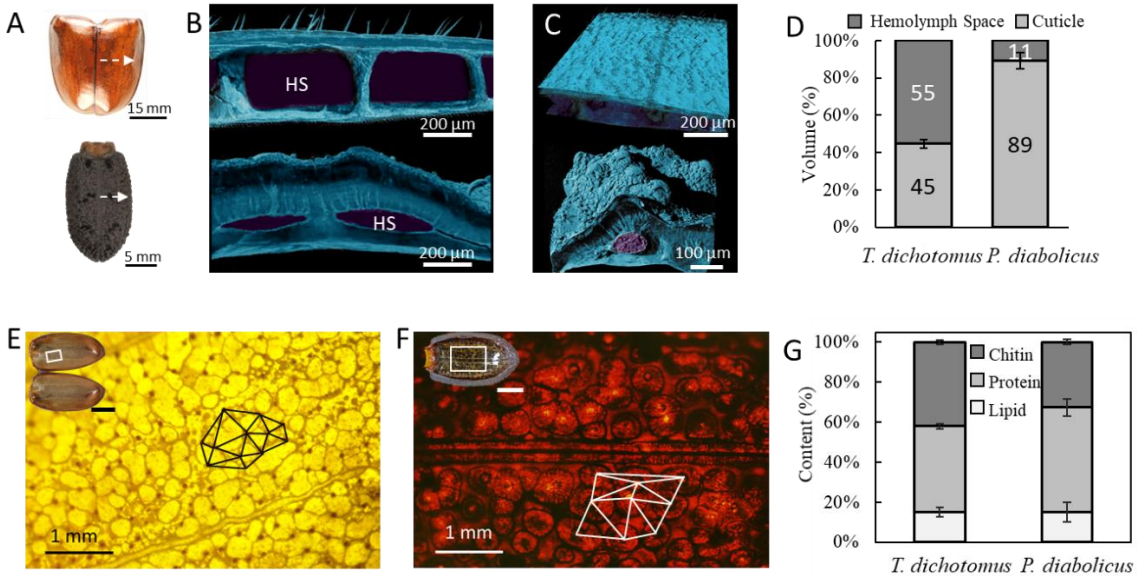

Figure 4. 2. Comparison of architectural features and chemical composition of elytra from *T. dichotomus* and *P. diabolicus*. A) Optical micrographs from *T. dichotomus* (top) and *P. diabolicus* (bottom). B, C) Computed tomography (CT) reconstructions of transverse and oblique cross-sections revealing D) volume fractions of the cuticle and hemolymph space. E) Ventral view of elytra from *T. dichotomus* and F) *P. diabolicus*, highlighting the 2D geometric distribution of trabeculae. G) Compositional variation of the elytra.

4.4.3 Microstructural features

SEM micrographs of polished transverse cross sections highlight the layered composite nature of both elytra and reveal three primary section, the epicuticle, exocuticle and endocuticle (Figures 4.3 A - C). The epicuticle is the outermost waxy coating on the

exterior of the organisms that prevents desiccation (*95*, *150*). The first structural layer, the exocuticle is composed of lamellae of non-mineralized alpha chitin fibrils surrounded by a protein matrix and organized in a periodic arrangement. Finally, there is the endocuticle that has a thicker dorsal and thinner ventral region separated by the hemolymph spaces and joined by the trabecula (Figures 4.3 D, F). The thicknesses of the exocuticle for both organisms is relatively similar (i.e., 18.0 ± 2.4 μm and 16.2 ± 7.0 μm, for flying and terrestrial beetles, respectively). However, the endocuticle is significantly thicker for *P. diabolicus* (148.5 ± 16.3 μm) versus that of *T. dichotomus* (31.4 ± 8.1 μm). This increase in thickness corresponds with a larger number of endocuticle lamellae (21.2 ± 4.3 layers for *P. diabolicus* vs. 7.2 ± 0.4 layers for *T. dichotomus*). Notably, the addition of endocuticle layers should provide increased energy absorption through microcracking between features.

In both organisms, the endocuticle has a hierarchical structure, consisting of lamellae that contain parallel fiber bundles, balkens, of unidirectional microfibrils (*42*). Each lamellae possesses a shift in fiber orientation with each successive layer, providing isotropy to the elytra (*90*, *151*). This rotating structure represents a Bouligand arrangement and remains prominent in arthropod cuticles (*112*, *152*, *153*) and has also been observed in fish scales (*154*). Examining fractured samples, fiber direction and angle appear to shift by 30° in the endocuticle of *P. diabolicus* and vary by 90° in the elytra of *T. dichotomus.* The incorporation of a greater angular variation between lamellae is likely adopted to maximize isotropy in the flying elytra with minimal number of layers. Further examination highlights the balkens in the endocuticle of *T. dichotomus* adopt a rectangular nature and

measure 4.4 ± 1.0 µm x 8.8 ± 0.9 µm. In contrast inter ply penetrating microfibers strands (i.e., z-pinning fibers) that join the neighboring layers in the endocuticle of *P. diabolicus* result in ovular balkens measuring 6.2 ± 0.8 µm x 4.9 ± 0.8 µm (Figure 4.3 G). These Z-pinning fibers add vertical support through successive layers and provide stiffening to the non-mineralized structure while augmenting interlaminar resistance to shear (*155*). Similar to those observed in tooth enamel and ram horns, these through thickness fibers infer common microstructural design themes used for compression resistance (*156*, *157*). Comparable through thickness fibers remain absent in the endocuticle of *T. dichotomus* suggesting a greater flexibility in the elytra (*8*). Examining further microstructural features, polished SEM micrographs of both elytra highlight that the trabecula represent an invagination of the exocuticle and consist of unidirectional, vertically aligned chitin fibers wrapped by endocuticle layers. For *P. diabolicus* a significant increase in the number of endocuticle layers wrapping around the trabecula core was observed (Figure 4.3 B). This fortification should allow the structure to withstand greater compressive load, similar to the incorporation of thicker columns in engineering structures (*158*).

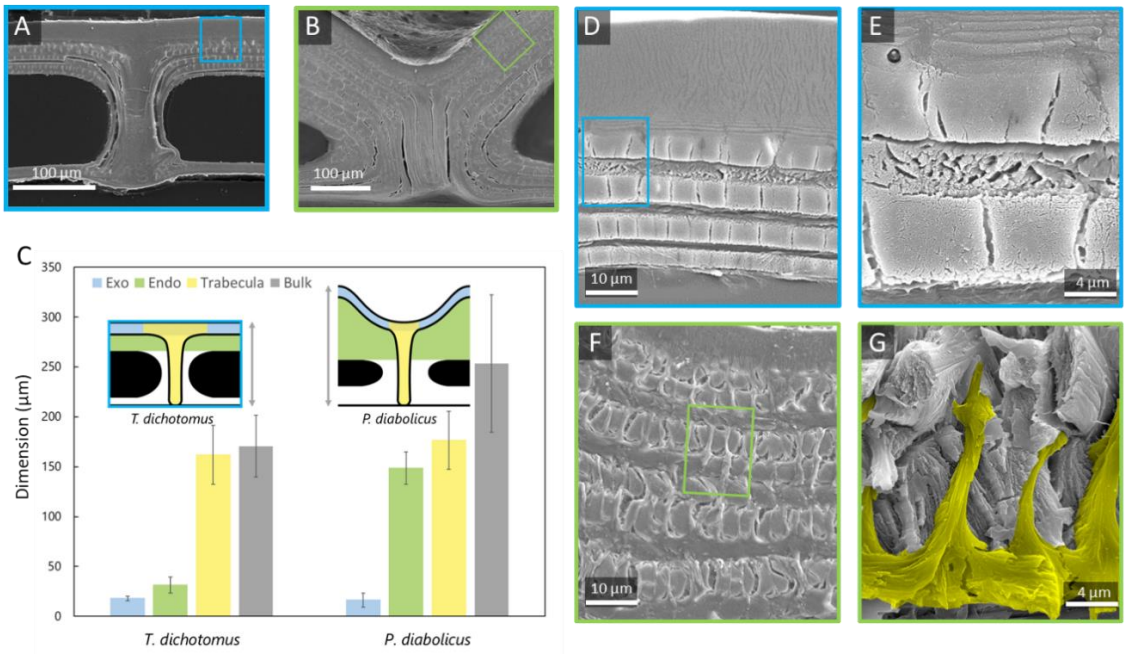

Figure 4. 3. Microstructural features of *T. dichotomus* and *P. diabolicus.* A) SEM of polished cross-sections of the bulk region in *T. dichotomus* and B) *P. diabolicus.* C) Variation in feature dimensions between the two the elytra. D) Cross-section of the exo and endocuticle of *T. dichotomus* highlighting the E) endocuticle. F) Cross section of the exo and endo cuticle of *P. diabolicus* highlighting the G) Z-pinning fibers between balkens.

4.4.4 Bulk mechanical testing

Flexural tests were performed to compare the strength and stiffness of the bulk sections of the flying and terrestrial elytra. Stress-strain curves (Figure 4. B) show an approximately linear response for both elytra yet the flexural strength was 338 ± 48.6 MPa and 26.1 ± 1.21 MPa, for *P. diabolicus* and *T. dichotomus* respectively, in the longitudinal direction. Similar values for flexural strength (376 ± 135 and 26.1 ± 9.50 MPa) were observed in the transverse direction yet show increased variance suggesting slight anisotropy due to the fiber orientation. Stress-strain curves highlight the order of magnitude difference in flexural modulus of the flying (0.52 ±0.03 GPa and 0.69 ± 0.15 GPa) and terrestrial elytra (7.80 ±1.49 GPa and 8.32 ± 2.17 GPa) in the longitudinal and transverse

orientation, respectively. Variations likely result from the natural curvature of the elytra in the transverse direction or the slight increase in thickness near the suture (*128*). For the ironclad beetle we see a stronger and stiffer response in the elytra as it fractures before reaching five percent strain. This response likely results from increased sclerotization and the addition of z-pinning fibers in the endocuticle of *P. diabolicus*. In contrast the elytra of *T. dichotomus* saw very little fracture at similar strain suggesting the microstructure incorporates a compliant matrix to withstand higher levels of strain with minimal stress. Such properties can be attributed to a lower degree of sclerotization in the endocuticle facilitating increased compliance as seen by varying the matrix in some engineering composite materials (*159*). During natural loading conditions the elytra of *T. dichotomus* must withstand cyclic loading imposed by actuation and flight and therefore would benefit from an elastomeric matrix. Similar demands in other organisms have been meet by the addition of elastomeric proteins such as resilin (*41*).

Tensile tests were used to evaluates the maximum stress and stiffness of fresh elytra samples. Figure 4.4 C highlights the brittle behavior for *T. dichotomus* and a ductile response of *P. diabolicus*. The average tensile strength and modulus of the elytra was 63.5 ± 3.38 MPa and 3.0 ± 0.91 GPa for *P. diabolicus*, compared to 56.4 ± 3.91 MPa and 2.4 ± 0.21 GPa for *T. dichotomus*. SEM micrographs of the posttest cross sections reveal uniform fractures in the elytra of *T. dichotomus* Figure 4.4 D, E with delamination between the in-plane balkens and fracture in the out of plane balkens. In contrast, the elytra of *P. diabolicus* reveals jagged fracture and delamination between layers with visible remains of the z pinned fibers at the bottom of Figure 4.4 F, G. Examining the stress strain graphs, the

ironclad beetle shows the greater initial stiffness and plastic deformation before failure. This likely results from the increased volume percentage of the endocuticle and the addition of z pinning fibers in this region. These through thickness fibers likely prevent reorientation of the balkens and upon critical strain fracture resulting in stress release shown as plastic deformation Figure figure4 C (*144*, *154*). Alternatively, the tensile response of the flying elytra shows a shallow initial slope that stiffens with additional strain implying a lower degree of crosslinking in the endocuticle facilitating the reorientation of the balken fibers in the tensile axis before fracture (*154*).

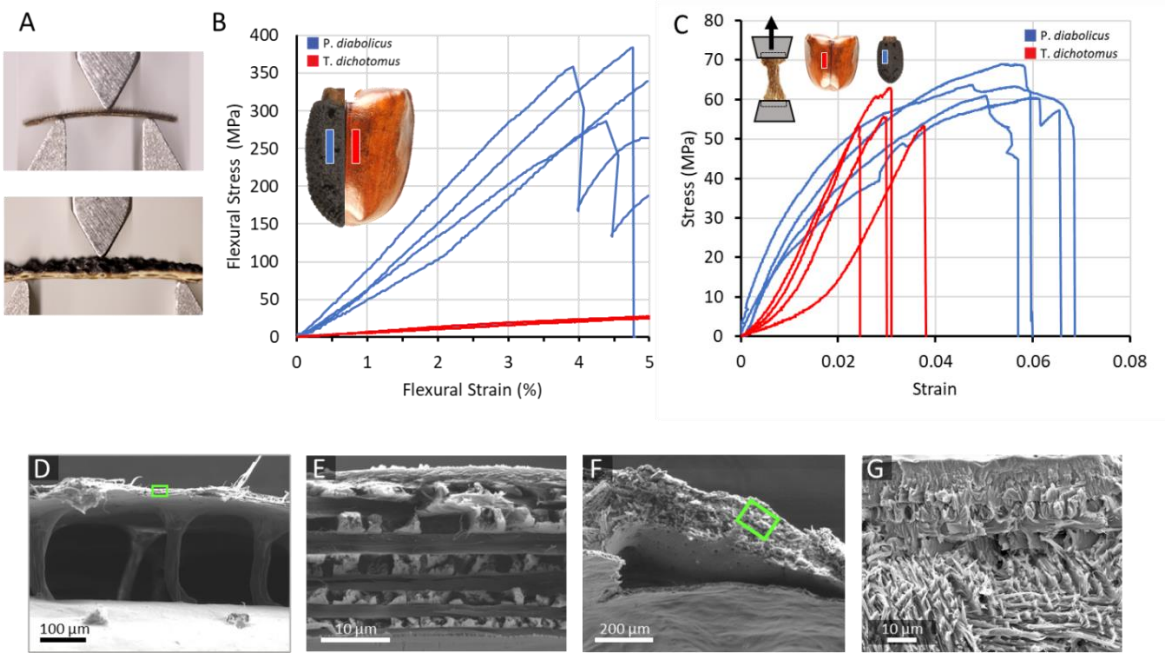

Figure 4. 4. Flexural and tensile response of flying and terrestrial elytra, *T. dichotomus* and *P. diabolicus*. A) Three-point bend test setup. B) Stress vs strain plot highlighting the flexural response of both elytra in the lengthwise direction. C) Stress strain curves highlighting the tensile response of the elytra. D) SEM of posttest fractured cross section of *T. dichotomus* highlighting E) the fractured microstructure. F) SEM of posttest fractured cross section of *P. diabolicus* revealing G) the fractured microstructure.

4.4.5 Puncture and nanomechanical properties

Puncture tests (Figure 4.5) were conducted on fresh elytra samples of both beetles to gauge their resistance to piercing or biting forces that occur in their natural habitats. The elytra of *P. diabolicus* had a greater resistance to puncture (24.7 ± 4.02 N) compared to *T. dichotomus* (8.76 ± 3.17 N). These results were fairly expected as the terrestrial nature of *P. diabolicus* demand a thicker, stiffer cuticle able to withstand the stresses from biting or pecking predators (*48*). Load vs. displacement data (Figure 4.5 B) highlight the relatively brittle response in the ironclad cuticle compared to the extensible flying elytra. This stiff behavior suggests the z pinning fibers and degree of crosslinking in the terrestrial endocuticle allows it to resist deformation. Furthermore, the elytra of *P. diabolicus* remains interfaced with the ventral cuticle and can transfer load to the structure (Nature Paper). This suggest the elytra is not necessarily tuned for energy absorption as compliance is incorporated in the overall architecture of the abdomen. Further analysis reveals post fracture cracks are visible along the center of the puncture region for *P. diabolicus* Figure 4.5 C top. In contrast we see deformation around the puncture region for *T. dichotomus* and failure reminiscent of tearing along the circumference Figure 4.5 C bottom. Again, this highlights the extensible nature of the flying elytra as we see failure do to shear stresses at the perimeter of the puncture pin instead of the central deformation and cracking of the biological composite.

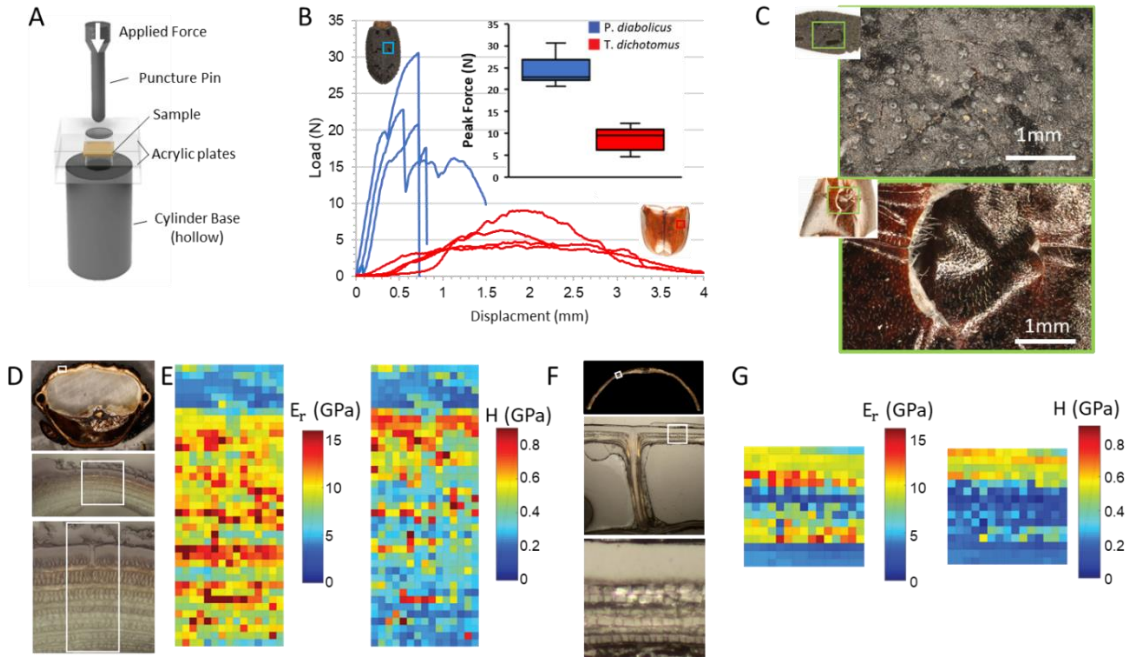

Figure 4. 5. Puncture and nanoindentation response of elytra sections. A) Puncture test setup. B) Plots of puncture response in of elytra and peak puncture force (inset). C) Dorsal view of the flying elytra after puncture. D) Optical micrographs transverse cross section of *P. diabolicus* (top), bulk cuticle (middle) and indentation location (bottom). E) Nanoindentation maps of reduced elastic modulus (left) and hardness (right) of *P. diabolicus*. F) Optical micrographs transverse cross section of *T. dichotomus* (top), bulk cuticle (middle) and indentation location (bottom). G) Nanoindentation maps of reduced elastic modulus (left) and hardness (right) of *T. dichotomus.*

Interrogating the regional hardness and modulus of the elytra, nano indentation maps were conducted on polished transverse cross sections. Indentation maps moving down the exo to the endocuticle of *T. dichotomus* and *P. diabolicus* are shown in Figure 4.5 E, F. The exocuticle of *P. diabolicus* has a hardness and reduced elastic modulus of 0.59 ± 0.15 and 9.85 ± 2.19 GPa, respectively, that drops to an average value of 0.37 ± 0.16 and 9.28 ± 3.37 GPa, when moving into the endocuticle. The nanomechanical properties within the exocuticle of *T. dichotomus* (Figure 4.5 G) remain similar to those seen in the terrestrial elytra but vary upon reaching the endocuticle. For *T. dichotomus*

hardness and reduced elastic modulus of the exocuticle average 0.53 ± 0.08 and 9.54 ± 1.70 GPa respectively yet drop in the endocuticle to an average of 0.20 ± 0.09 and 6.15 ± 3.30 GPa. The nanoindentation maps of both organism highlight a drop in hardness when moving from the exo to the endocuticle and further suggest a variation in sclerotization (Figure 4.5 E, F). Particularly for the endocuticle, the reduced elastic modulus depends heavily on fiber orientation of the balkens as we see a deviation among rows in both indentation maps.

Fourier-transform infrared spectroscopy (FTIR) along the elytra cross section of the flying and terrestrial beetle confirms that the exocuticle in both organisms has a higher degree tyrosine, 1260 cm^{-1} (broad peak between 1300-1200 cm^{-1} and a sharp peak around 1260 related) knows for being part of crosslinking process (*160–162*). Figure 4.6 highlights, a concentration decreases moving deeper into the cuticle. While this is consistent for both elytra, there is a clear gradient in the indentation data for the terrestrial beetle that may suggest a need for varying stiffness to gradually resist deformation and protect against possible impact events. Overall, the nanomechanical properties of these organisms results from a variation in fiber orientation and the degree of crosslinking in the protein matrix surrounding the fibers.

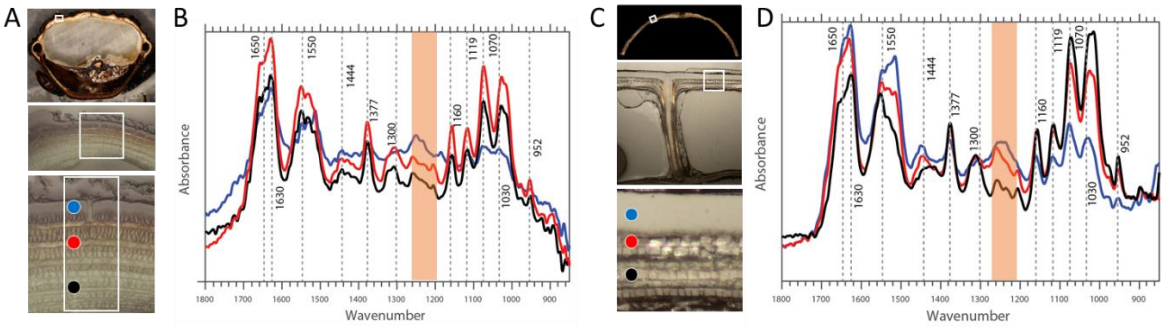

Figure 4. 6. FTIR spectra of elytra cross-sections. A) Optical micrographs transverse cross section of *P. diabolicus* (top), bulk cuticle (middle) and spectra location (bottom). B) FTIR spectra along the cross section of *P. diabolicus* corresponding to the locations in (A) bottom. C) Optical micrographs transverse cross section of *T. dichotomus* (top), bulk cuticle (middle) and spectra location (bottom). D) FTIR spectra along the cross section of *T. dichotomus* corresponding to the locations in (C) bottom.

4.4.6 Bioinspired Composites

Serving as a protective composite, the elytra of flying and terrestrial beetles provide two alternative means of survival. To examine these potential mechanical advantages based on variations of matrix material, a series of helicoidal carbon fiber composites that used epoxy and urethane matrix material were fabricated and tested in drop weight impact (90J). Post impact evaluation of surface damage (Figure 4.7 A-D) demonstrated the urethane composites mimicking the flying beetle elytra suffered no permanent deformation or prevalent internal damage (Figure 4.7 E-H) compared to their epoxy counterparts. Subsequent examination of the load vs time plots revealed the epoxy composites mimicking the terrestrial beetle were an order of magnitude stronger than the urethane counterparts as seen by the peak loads in Figure 4.7 I, J. The plateau of energy vs time plot (Figure 4.7 I) further highlights that energy is being dissipated through deformation and fracture in the epoxy sample opposed to viscoelastic forces as seen in the urethane samples

that all almost return to zero (Figure 4.7 J). This response highlights that the urethane-based composites are storing potential energy due deformation of the material and can release it at a minimal loss due to fracture of the composite. Compression after impact test show a 62% improvement in residual strength of the 30° helicoidal composites compared to the quasi isotropic design and an order of magnitude improvement over the urethane composites. In contrast the helicoidal urethane composites saw diminished performance over the quasi isotropic design highlighting a benefit to the adoption of a larger fiber orientation. These variations in matrix material and fiber orientation provide valuable insight into the fabrication of strong energy absorbing materials. Yet, there remains a wide potential to tune these composite parameters for specific applications.

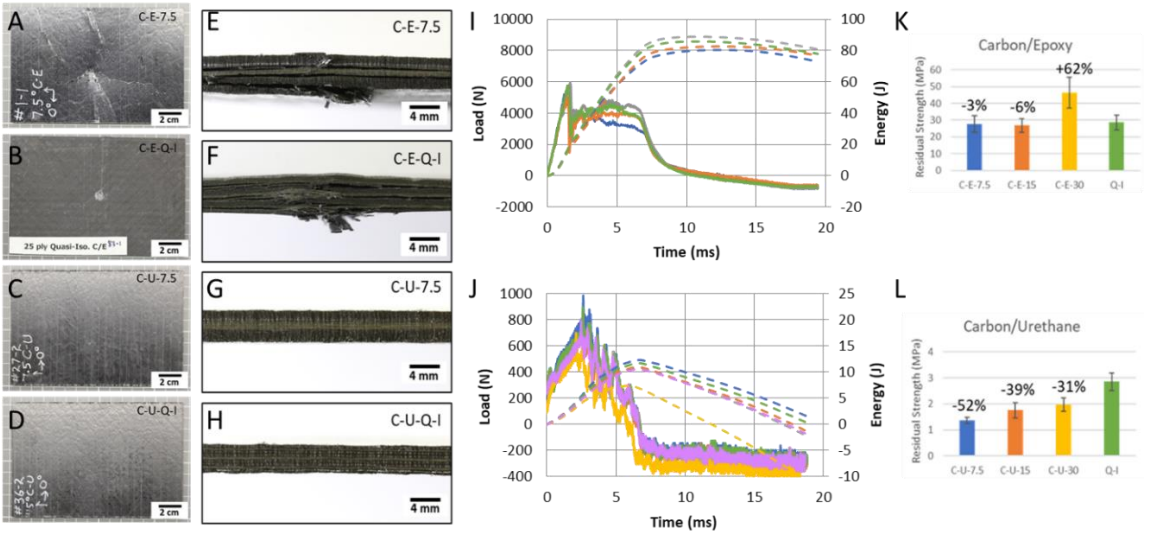

Figure 4. 7. Drop weight impact test of bioinspired helicoidal carbon/epoxy and urethane/epoxy composites. A) Post impacted representative 7.5° helicoidal carbon/epoxy composite and B) quasi isotropic control. C) Post impacted representative 7.5° helicoidal carbon/urethane composite and B) quasi isotropic control. C) Transverse cross section of representative 7.5° helicoidal carbon/epoxy, F) quasi isotropic carbon/epoxy, G) 7.5° helicoidal carbon/urethane and quasi isotropic carbon/urethane composite. I) Representative Load and energy vs time plot for 7.5° helicoidal carbon/epoxy and J) .5° helicoidal carbon/urethane panels. K) Residual strength of composites after impact for carbon/epoxy and carbon/urethane composites

4.5 Conclusions

This This work characterizes and compares the mechanical response, hierarchical multiscale structure, and chemical composition of beetle elytra from two evolutionarily specialized species: the flying *T. dichotomus* and terrestrial *P. diabolicus*. The structure mechanical property relationships of these elytra were derived to compare and understand the architectures and chemical properties responsible for allowing enhanced stiffness and strength. The elytra of *P. diabolicus* revealed superior flexural stiffness and strength when compared to that of *T. dichotomus.* This response results from a thicker more heavily crosslinked endocuticle that incorporates z pinning fibers that stiffen the cuticle to resist predator interrogation. Conversely the flying elytra incorporated few endocuticle layers and an elastomeric matrix to facilitate actuation and the cyclic demands imposed by flight.

Deviations among microstructural features and chemical compositions invoke questions to the contribution of cuticle thickness, number of endocuticle layers, hemolymph space volume, on the local mechanical response of the bulk cuticle. Evident deviations in the failure modes of the both elytra were observed, with the terrestrial beetle showing a stiff yet ductile tensile response, and the flying elytra showed greater extensibility in both puncture and flexure. Initial deviations may arise from the internal microstructure of the endocuticle. One hypothesis remains that a more predator resistant endocuticle must adapt structural means to stiffen the cuticle and selectively release energy. Z-pinning fibers along with chemical gradients in the terrestrial elytra may constrict movement or reorientation of fiber bundles when strained causing an initially stiff response in tension. Upon reaching a higher strain these linkages may succumb to localized fracture

relieving stress and toughening the structure. Conversely in the flying beetle, an absence of these features along with an extensible matrix material would result in an initially compliant response as the fiber bundles are free to move Figure 4.4 E. Similar reorientation effects have been seen in other biological fibrous composites to increase toughness (*154*). The further lack of chemical gradients and endocuticle layers would facilitate a compliant response in the flying elytra. Upon observing the transverse cross sections of the terrestrial beetle, we see a clear evolutionary adaptation to unite the elytral elements by a medial suture and lateral interfaces. For *P. diabolicus*, lateral interfaces connecting the elytra to the ventral cuticle facilitate load transfer to the abdomen of in this organism allowing it to withstand relatively higher forces as seen in chapter 2. This may explain why the ironclad beetle shows relatively lower puncture resist when compared to some cockroach species since this experiment fails to consider the load transferring benefits of the whole cuticle structure (*47*). A synergistic exoskeleton and a tailored endocuticle may have evolved to respond to increased interrogation by local predators.

These chemical and structural adaptations and corresponding mechanical properties echo the evolutionary lineage of Coleoptera and the tailored nature of the elytra. Unable to readily evade predators, terrestrial beetles must adapt forms of active deterrents (chemical secretions) or heavily fortified cuticles to deter predation. Conversely, flying counterparts ideally maintain relatively light weight robust elytra to facilitate the demands of aerial locomotion. Therefore, composite designs mimicking the areal variants would serve as valuable candidates for the incorporation in unmanned aerial vehicles while the stronger

terrestrial inspired designs would be more suited for structural engineering or personal protective materials.

There remain many species in this prolific order that we can continue to study in hopes of gleaming insight into their structural diversification. The ironclad family remains relatively unstudied for their mechanical porous and microstructural features (*50*, *54*). With such a varying set of ecological pressures additional research remains to increase our understanding of the external forces that drive evolutionary adaptations in the hopes of applying these structural insights into the creation of engineering materials.

The results of this work compare the variations in structure mechanical property relationship of the hardened forewings, elytra, in a prolific taxa of flying and terrestrial beetles. Structural and mechanical analysis of the terrestrial elytra reveal a greater flexural stiffness and hardness at the cost of extensibility and a light-weight design able to sustain flight. Fortifications to this elytra result from ultrastructural topography, a denser cuticle, through ply pinning fibers and gradations of crosslinking in the polymer matrix. The adaptation to forgo flight lead to behavioral but also structural adaptations that fortified the terrestrial elytra of this organism to resist predation and thrive in its native habitat. This work provides several design guidelines applicable to the manufacturing of light weight rugged composite materials with avenues for damage tolerance and multifunctionality.

Chapter 5: Arthropod inspired biomimetic composite materials

5.1 Background

Combining high strength and toughness, fiber reinforced composites (FRC) have been adopted in a variety of industry applications due to their impressive strength to weight ratio (*5*, *163*). These structures incorporate a woven or unidirectional fabric reinforcement material embedded in matrix. Altering the fiber and matrix material provides considerable versatility in tensile strength and modulus in composites, facilitating their adoption for widespread automotive and aerospace structural frames (*164*). Analogous to natural composites, these engineering materials provide a good framework for application of bioinspired architectures composed of alpha chitin fibers in a proteinaceous matrix.

In Nature the helicoidal arrangement of fibers provides several toughening mechanisms, leading to enhanced damage tolerance and energy absorption. Because of the anisotropic stiffness of chitin nanofibers, which are stiffer in the long axis (*165*), the helicoidal architecture provides inherent elastic modulus oscillation resulting from the periodic nature of the helicoidal microstructure. Such modulus oscillation has been identified via nanoindentation in cross sections of osteonal bone (*166*), lobster cuticle (*136*), and the mantis shrimp dactyl club (*152*). The gradient thus results in reduction in local driving force for crack propagation between layers. Moreover, the modulus difference between the weak interface and the mineralized fibers allows for extrinsic toughening in the form of crack deflection at the fiber interface. Application of these architectures using engineering materials provides an opportunity to increase the toughness and impact resistance of engineering composites.

Helicoidal fibrous architectures such as those identified by Bouligand have been identified as advantageous designs for biomimetic structural materials. Many groups have begun to create analogues using FRC based on the helicoidal geometry due to their impressive ability to dissipate energy and reduce through thickness damage (*87*, *151*, *167*, *168*). Grunenfelder et al. fabricated sets of 48 plies biomimetic helicoidal carbon fiber/ epoxy composites featuring small, medium and large rotation angles of 7.8°, 16.3° and 25.7° respectively (*87*). The impact response of theses panels was compared to unidirectional and quasi-isotropic industry standards to evaluate the mechanical properties of a helicoidal architecture and uncover optimum rotation angles for impact resistance. After a 100 J drop tower impact, the medium angle bioinspired panels displayed a 50% reduction in surface damage and dent depth when compared to the industry standard. Furthermore, the large and medium angle composites showed a 20% and 49% reduction in dent depth over the quasi-isotropic panels, respectively. Ultrasonic post impact analysis highlights the ability of helicoidal structure to dissipate energy through lateral crack propagation, thus promoting toughening in the composite and deterring catastrophic failure (*169*, *170*).

Our work endeavors to investigate the fracture behavior of bioinspired helicoidal composites while determining the limiting sample thickness for maintaining strength and toughness. Biomimetic composite materials were manufactured based on the architectures of arthropod cuticles, consisting of carbon fiber reinforcement embedded in a polymer matrix. Their mechanical properties were further acquired and compared to industry

standards. This research provides design guidelines for the manufacturing of composite materials with higher impact resistance and fracture toughness.

5.2 Objectives and hypotheses

Here we fabricate and test flat panel fiber reinforced helicoidal composites inspired by the arthropod cuticles to evaluate the strength and toughness of the architecture. These biomimetic composites were fabricated for Charpy impact test using a variety of techniques including industry layups of unidirectional carbon fiber and additive manufacturing of fiber reinforced carbon/ nylon and Kevlar/ nylon. Different from conventional quasi isotropic layup, impact test revealed the helicoidal architecture effectively dispersed the impact energy throughout the material leading to large delamination that mitigated through thickness fracture. This work provides insight into the energy absorbing capability and impact failure modes resulting from variations in the architecture of composite materials.

5.3 Materials and methods

Prepreg Fiber-reinforced composites processing. Reinforcement used in the manufacturing of the composites consisted of unidirectional carbon fiber, 85 grams per square meter (GSM) and 150 GSM out of autoclave toughened epoxy pre-impregnated carbon fabric (AX-6201XL-C-85GT700-24" RC34, and AX-6201XL-C-150GT700-24" RC34, Axiom, USA). The layup architecture used a 16.3° inter-ply rotation angle and either 12, 24, 48, or 96 layers resulting in three final thicknesses of 1.5, 3, and 6 mm, respectively. Five sets of composite panels, each measuring 305 mm long and 305 mm wide, were fabricated with 48 prepreg layers that were laid up with different ply orientations. The 16.3°

angle between successive layers was chosen based on previous studies on helicoidal composites (*169*). Samples were cured using the manufactures specified procedures. The panels were sectioned to meet the ASTM standards with five duplicates of each produced for statistics of mechanical testing and structural characterization.

Wet layup Composite fabrication: After layup, samples were vacuum bagged (> 28² Hg) and debulked for 4 hours at room temperature to remove trapped air. After the room temperature vacuum hold, samples were cured according to the manufacturer's recommended cure cycle.

All samples were subjected to a freestanding post-cure cycle consisting of a ramp at 2° C/min to 71° C. This lower temperature rate was employed to avoid crossing the instantaneous glass transition temperature of the resin and optimized for out of autoclave production. The samples were held at 71° C for 8 hr. Samples were finally cooled back to room temperature at 3° C/min.

Charpy Sample Fabrication. Charpy V-notch (ASTM E23) were made using epoxy Prepreg carbon fiber (AX-6201XL-C-150GT700-24" RC34, Axiom, USA) and fiber reinforced additive manufacturing (Mark forge, USA). The 52-ply Carbon fiber prepreg Charpy panels were manufactured using 0° and 90° fiber orientations as well as 16.3° and 45° inter-ply rotation angles (Table1) with conventional vacuum bagging techniques. Samples were cured in the manufactures specified cycle: one-hour ramp from room temperature to 121° C, one hour hold and then ramp down to room temperature. The panels were sectioned to meet the ASTM standards with five duplicates of each produced for statistics of mechanical testing and structural characterization.

The additive manufactured Charpy samples were prepared in a Fusion360 3D printer, imported into Markforged Eiger slicing software and prepared for additive manufacturing on a Mark Two (Markforged). Samples were orientated with the ground plane (vertically opposed from V-notch) touching build surface with the following common parameters: 2 Plastic Walls (Shells), 2 Roof and Floor Layers (visible surfaces on top/bottom faces). Solid infill (plastic material inside shells) was selected for consistent distribution inside part geometry. Fiber reinforcement was utilized with the default layer height (0.1mm for Kevlar, 0.125mm for Carbon Fiber) determined by fiber diameter. Fiber arrangement (angle) was laid down every other layer according to the test specifications with the first fiber reinforced layer occurring on layer (3) immediately (following two lower floor layers) and the last deposed one print layer before the beginning of the V-Notch (about 7.9mm avg. height measured from base).

Optical and scanning electron microscopy. Cross-sectional imaging of the panels before and after testing was achieved by first polishing the edges of the samples using progressively finer grit silicon carbide sandpaper down to a grit of 1200 (15 μm). The sample cross-sections were then imaged using an optical microscope (Axio Imager.A2m, Zeiss, Germany) and a scanning electron microscope (MIRA3 GMU, TESCAN, USA) operated at 10 kV accelerating voltage.

Impact testing. Prior to testing, the dimensions (thickness and width) of all composite test specimens were measured in multiple areas using calipers, averaged, and recorded. Impact testing was performed in accordance with ASTM D7136 using an instrumented drop weight impact testing system (Dynatup, Instron, USA) equipped with hemispherical

indenter tip with a diameter of 16 mm. The drop height and mass were adjusted to deliver an impact energy of 12J, 20J, 35J, and 70 J. During the tests, specimens were fixed in place to a rigid steel base, with a 76 mm x 127 mm rectangular holder with a 40mm hole in the center. After impact, photographs of each sample were obtained to examine external damage. The dent depth was measured using a depth gauge. Internal damage was probed using a non-destructive Computed Tomography technique (CT-scans) at 50 µm using a SkyScan 1076 at 250 µA and 40 kV with no Filter (SkyScan 1076, Bruker, USA).

5.4 Results and discussion

5.4.1 Microstructural inspiration for fabrication of biomimetic composites

The helicoidal architecture is a common design motif often found in a variety of arthropod cuticles (*112*, *170*, *171*). Figure 5.1 provides an overview of the helicoidal micro-structure and laminated architecture of some beetle cuticles and its application in the fabrication of composite materials. Previous studies characterized the angular variation between successive layers of aquatic arthropods and found a gradation in pitch varying from 1.6° to 6.2°, yet used larger angles when fabricating engineering composite mimics (*169*). This previous works highlighted a medium angle showed the greatest reduction in dent dept and provides a strong grounds for application. Therefore, we incorporated a 16.3° rotation angle between successive plies to reduce the minimum number of layers needed to complete a helicoidal rotation and materials cost.

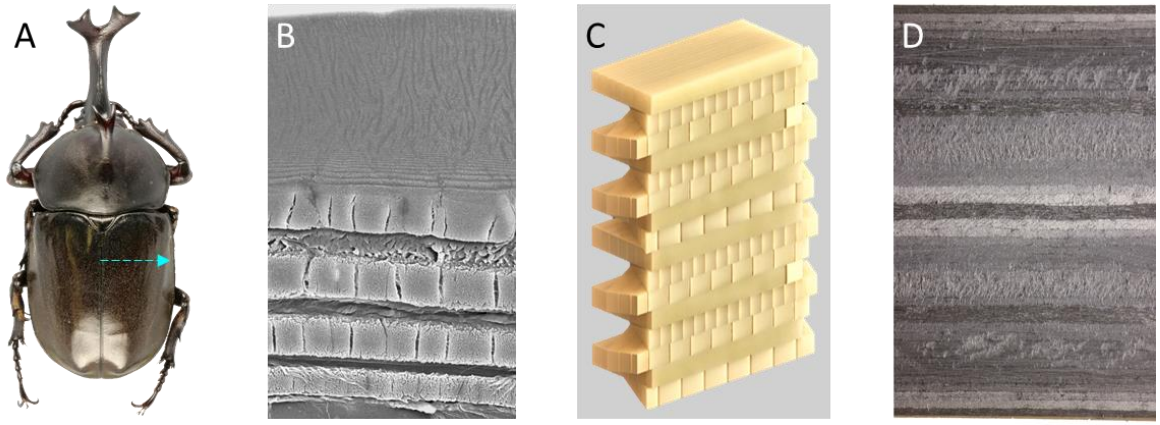

Figure 5. 1. Overview of laminated fibrous architecture within arthropod cuticles. (A) Optical overview of *T. dichotomus.* (B) SEM micrograph of the fibrous architecture found in the beetle cuticle. (C) Model of the Bouligand structure composed of rotating staked fibrous layers. (D) Cross section of a carbon fiber reinforced compotes highlighting the application of the biological architecture in the fabrication of composite materials.

5.4.2 Biomimetic composites fabrication

To increase the number of rotations while maintaining a consistent thickness, biomimetic composites were fabricated using two different thicknesses of carbon fiber. Figure 5.2 highlights how number of layers and ply thickness affects the final dimensions of the final composite. Test samples were fabricated for Charpy impact, drop weight impact, and flexural test using prepreg carbon fiber and industry standard vacuum bagging techniques highlighted in section 5.3. Details regarding layup geometries and fiber orientation of bulk laminates sectioned for their respective test are shown in Table 5.1 with a graphical representation found in Figure 5.3 and 5.4, respectively.

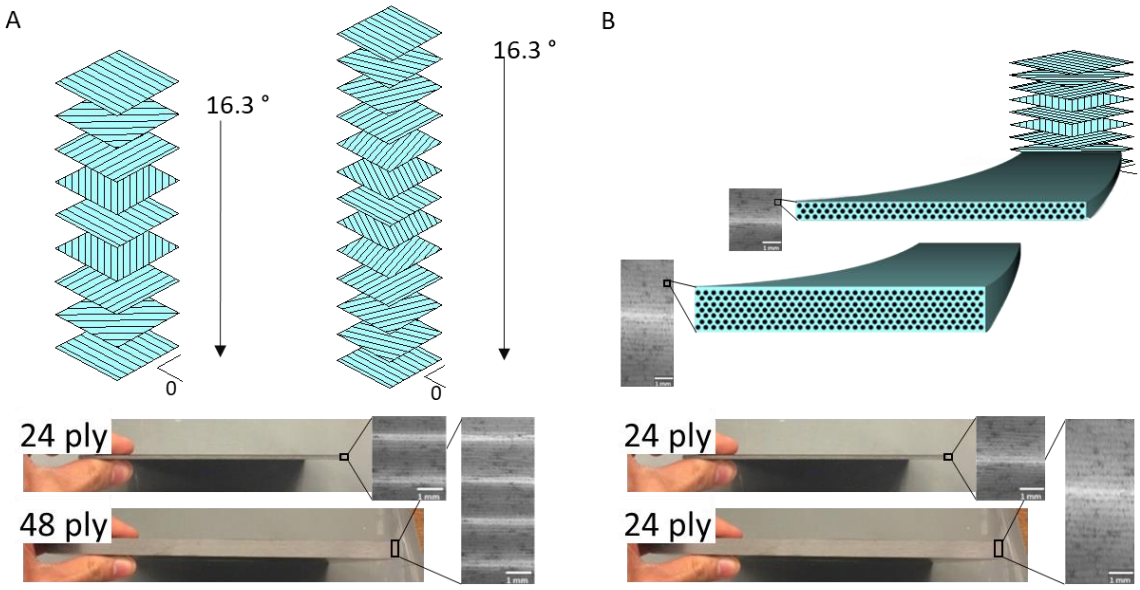

Figure 5. 2. Variation of thickness in composite materials. (A) Method of varying thickness by increasing the number of layers in the composite. (B) Variation of thickness by increasing the thickness of lamella while keeping the same number of layers.

After fabrication, cross sections of the samples were examined to ensure the quality and inspect for any voids or defects. Optical micrographs of cross sectioned Charpy impact samples are shown in Figure 5.3. The high degree of contrast in the composite panels results from the shifting orientation of the individual fiber layers with bright regions corresponding to in-plane fibers and dark regions corresponding to out-of-plane fibers. The composite samples showed fully dense nature with no visible voids. Additional helicoidal Charpy impact composite samples were fabricated using additive manufacturing as an alternative technique and showed a uniform outer appearance across all test specimens with a representative sample seen in Figure 5.3 C.

Table 5.1. Fiber layup orientations for Charpy impact samples.

Panel Design	Layup
Zero	[0/0/.../0]
Ninety	[90/90/.../90]
Helicoid	[0/16.3/.../180]
Quasi - Isotropic	[0/45/90]

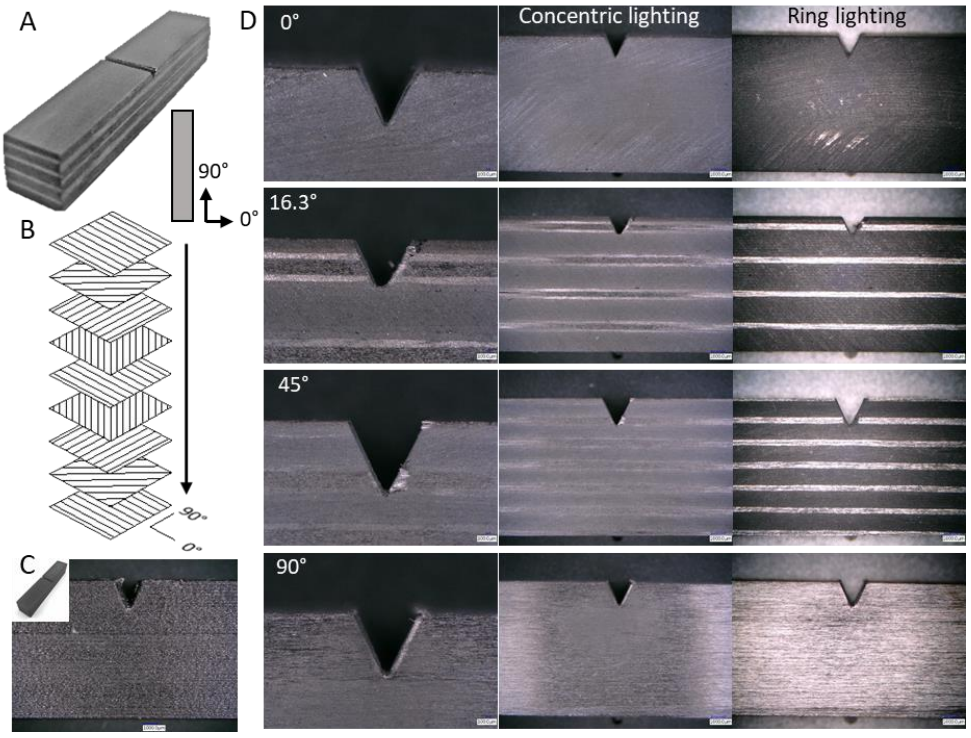

Figure 5. 3. ASTM E23 Charpy V-notch impact test samples. A) Optical micrograph of a 52-ply carbon fiber/ epoxy helicoidal sample. (B) Schematic of fiber architecture in a helicoidal composites. (C) Optical lateral view of additively manufactured Carbon/ Onyx composites. Inset, isometric view of the sample. (D) Optical micrographs of cross sections of prepreg samples showing the V-notch and the shifts in fiber orientation between the different variations in fiber angle.

Samples for flexural and drop weight impact tests were fabricated and examined using the same methods. Cross-sectional analysis of the composites was performed to assess the quality and check for any voids or defects. Optical microscopy of the test specimens as well as cross-sections of representative panels are shown in Figure 5.4. Again, the periodic variation in orientations between successive fiber layers results in the characteristic striated bands in the cross-sections. Composites varied in thickness from between 1.5 mm, 3 mm and 6 mm. In general, composites fabricated using 85Gsm fabric tended to have higher post- cured thicknesses showing an average increase of 6.8%. This may result from the increased number of layers needed to maintain the Helicoid and the fact that the uncured fabric was slightly larger than half the thickness of the 150GSM counterpart. Panels show good infiltration of the matrix resins into the reinforcement; yet few small voids where air may have become trapped and were present in the 6 mm, 96 and 48-ply composites.

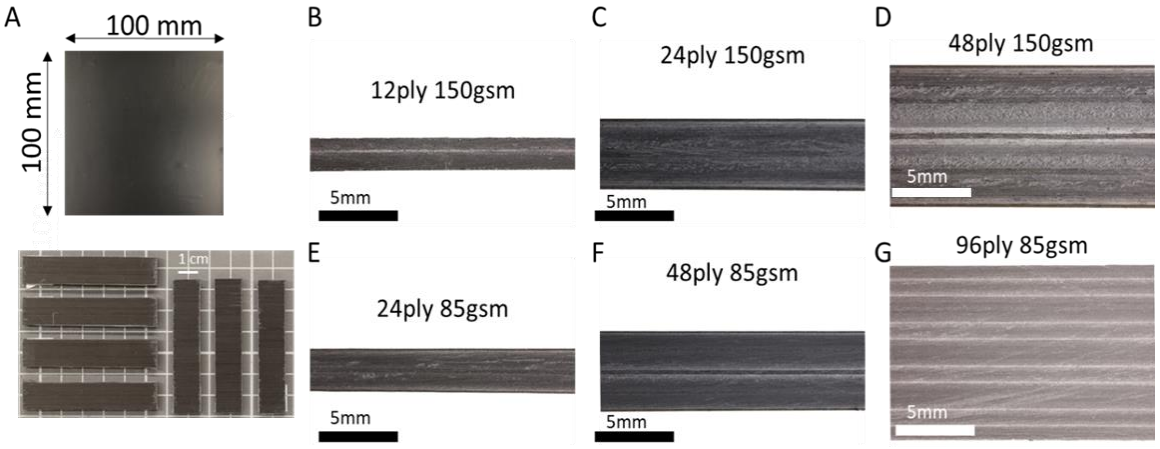

Figure 5. 4. Optical microscopy and cross-sections of carbon fiber, epoxy composite panels manufactured for flexural and drop weight impact test. (A) A representative intact as-fabricated composite laminate (top) and sectioned flexural test specimens (bottom). (B) Cross-section of carbon 12-ply 1.5 mm helicoid. (C) Cross-section of carbon 24-ply 1.5 mm helicoid. (D) Cross-section of carbon 48-ply 3 mm helicoid. (E) Cross-section of carbon 24-ply 3 mm helicoid. F) Cross-section of carbon 48-ply 6 mm helicoid. (G) Cross-section of carbon 96-ply 6mm helicoid.

5.4.4 Drop weight impact tests of biomimetic helicoidal FRCs

For the instrumented drop tower test, the striker was equipped with a load cell to record force as a function of time during the impact event. The kinetic energy of the impactor just before it contacts the specimen is defined as the impact energy E and remains the energy transferred into the composite. A percentage of this impact energy is absorbed by the composite through heat generation, material damage and other phenomena (*172*). The velocity and displacement were calculated by dividing the recorded force by the mass of the impactor and integrating with respect to time and the initial impact velocity (equation 1 and 2).

$$v(t) = v_i + \mathrm{g}\, t - \int_0^t \frac{F(t)}{m}\ dt \quad (1)$$

Where *v*, represents impact velocity at time *t* (m/s), *t* is time during the test where *t* = 0 is when the impactor initially contacts the sample and *F*, is the measured impact contact force at time *t*, (N).

$$\delta(t) = \delta_i + v_i t + \frac{\mathrm{g}t^2}{2} - \int_0^t \left(\int_0^t \frac{F(t)}{m} dt \right) dt \quad (2)$$

Where δ, represents impactor distance at time *t*, (m) and δ_i is impactor displacment from reference point at time *t* =0, (m).

Integration of the acceleration and velocity curves based on initial conditions allows for the derivation of the force displacement curve. This plot comprises the loading and unloading phase with area between these two segments representing the system hysteresis and indicating the total energy dissipated in the impact process. Therefore, the area should be minimal for pure elastic samples and substantially noticeable for inelastic.

Samples measuring 100 × 100 mm were subjected to 11, 20, 35, 70 J of impact energy using a drop tower. The damage modes of the panels were characterized after the impact tests using CT scans. Figure 5.5 highlights the load versus time response of representative helicoid panels of each thickness. Overall, sampels with the increased number of layers showed similar stifness yet reach greater peak loads compared to sampels of similar thicknes. This suggest fiber fracture, cracks and plastic deformation occur with greater prevalence in samples with less periods of rotation. Therefore, increasing the period should increase the damage tolerance of the composites. Comparing peak load among all

samples show an expected increse with laminate thickness and failure at all loads in the thinner sampels.

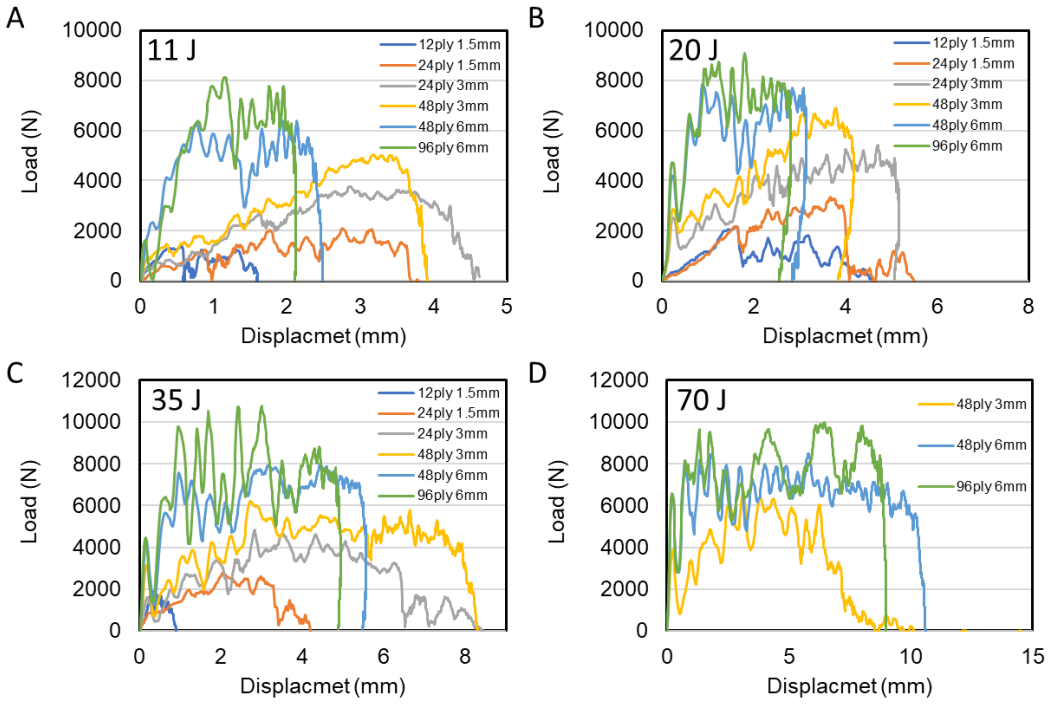

Figure 5. 5. Representative impact load versus displacement plots of biomimetic composites at four different impact energies. A) Representative load vs displacement plots for helicoidal composites impacted at 11J, B) 20J, C) 35J and D) 70J.

A comparison of the maximum energy absorbed in all compsite materials is shown in Figure 5.6. The term "absorbed energy" refers to the energy transferred to the composite/ holder system and is measured by the difference in kinetic and potential energy of the striker from initial to final contact. The governing equation for this as set forth by ASTM D7136/D7136M is shown in equation 3. Where E_a, v and δ refer to the absorbed energy (J), impactor velocity (m/s) and impactor displacement (m) all at time t. Furthermore, v_i and g represents impact velocity (m/s) and gravity (m/s^2).

$$E_a(t) = \frac{m(v_i^2 - v(t)^2)}{2} + mg\delta(t) \quad (3)$$

Equation 3 relates the loss of velocity and depth of penetration during impact to the energy lost by the striker. Notably, the potential energy term ($mg\delta(t)$) relies on displacment and is used to account for the elastic energy of the sample. In a perfectly rigid composite this term will remain zero while in a perfectly elastic sample this term would peak at maximum deformation before returning to zero upon unloading of the composite.

For the 11J impacted sampels Figure 5.6 highlights a relatively low peak energy in both 1.5 mm pannels signaling a rupture of the composites. In contrast, starting with the 24-ply varient all composits absorbed nearly the full impacted energy. Fot the 3 mm composites subject to a 35J impact, rupture was observed in the 1.5 mm and the 24-ply 3 mm composite however the 48-ply 3 mm sample experienced no rupture and showed a 36% improvement in energy absroption in respects to its counterpart (Figure 5.6 bottom right). This is likey attributed to increased crack diflection due to the additional periods of rotation guiding a torturous crack path (*151*). When examining the 6 mm pannels, no rupture of the composites was noticed for any impact load tested. However, variations in dent dept were observed for the 6 mm pannels with the 96-ply composite deforming 0.70 ± 0.09 mm, compared to 0.88 ± 0.1 mm in the 48-ply variant subject to a 35J impact. Yet, further caracterizarion will highlight the internal damage.

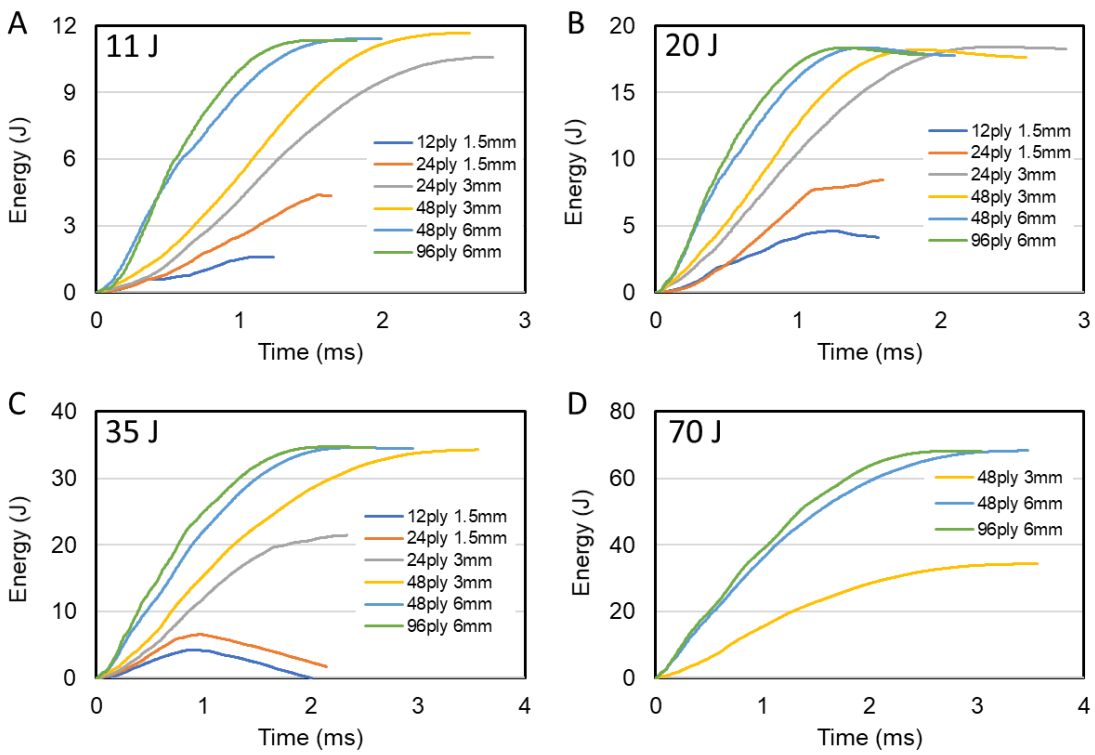

Figure 5. 6. Instrumented drop tower Energy vs time plots for biomimetic composites with varying number of layers at four different impact energies. A) Representative Energy vs time plots of helicoidal composites impacted at 11J, B) 20J, C) 35J and D) 70J highlight improved energy absorption for thicker composites with more periods of rotation.

Computed tomography (CT) scans were used to assess internal damage of the composites post impact. Figure 5.7 and 5.8 show representative cross sections that provide insight into crack propagation and fiber fracture. For the 12J impact, minimal internal damage to the 3 mm and 6 mm samples was observed. While in the 1.5 mm thick composites show rupture in the 12-ply variant with a large degree of deformation at the impact sight and prominent delamination between layers. Examination of the 24-ply variant shows delamination of the ventral region of the composite and a relatively smaller dent depth in the dorsal region. This behavior highlights the improved resistance to

penetration gained by the additional periods of rotation that assist to dissipate energy by guiding crack propagation and prevent damage in the through thickness direction.

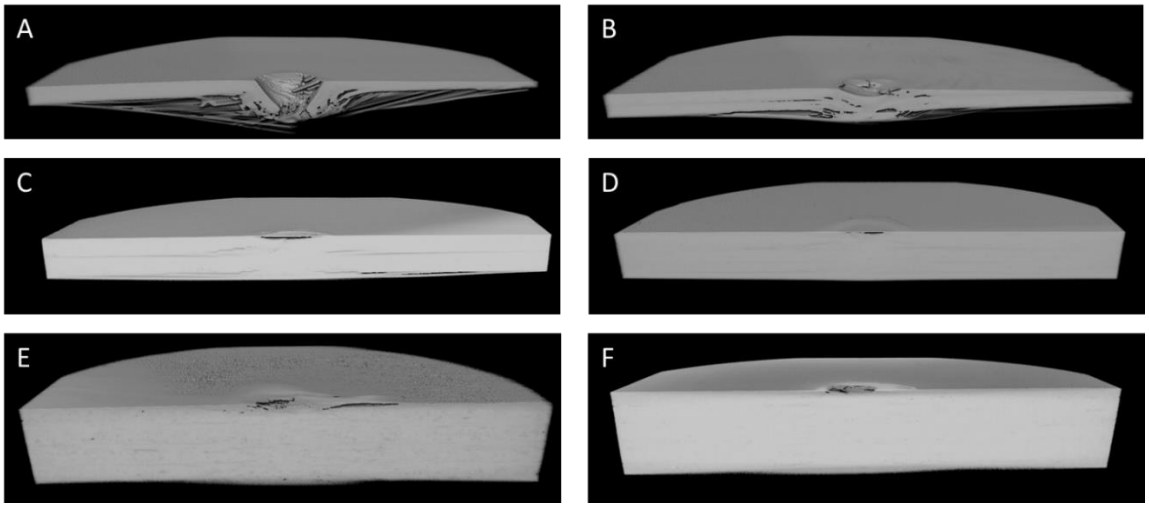

Figure 5. 7. Computed tomography reconstructions of 12J impacted panels. (A) Post impact CT reconstruction of 12-ply 1.5 mm, (B) 24-ply 1.5 mm, (C) 24-ply 3 mm, D) 48-ply 3 mm, (E) 48-ply 6 mm, and (F) 96-ply 6 mm composites highlighting surface deformation and internal damage.

CT reconstructions of the 20J impacted composites revival similar trends with rupture and delamination in prevalent in the 1.5 mm samples, delamination present in the 3 mm samples and dents visible in the 6 mm samples (Figure 5.8 A-F). Further examination highlights ruptures occur in both 1.5 mm thick samples with the 24-ply variant showing grater delamination than the 12-ply sample. Similarly, the 3 mm samples show a greater dent depth and more widespread internal delamination in the variants with fewer periods of rotation. Finally, the 6 mm composites show a minimal through thickness damage with a small degree of delamination visible at the dorsal region of the 48-ply variant. This highlights the benefit of an increased number of periods of rotation to mitigate through thickness damage by loading a larger area of the elastic matrix component in the composite.

Figure 5.8 G shows the whole energy profile of laminates and highlights the energy exchange between the impactor and the composites. This plot was derived from the kinetic energy of the striker before impact and equation 3. Since impact energy should be completely absorbed by the composite when perforation takes place, the penetration threshold of the sample can be identified by the equality of the impact energy and absorbed energy (*172*). Results of all the composites tests are shown in Figure 5.8 G, with the data points represented by solid circles accompanied by fitting lines. Typically, as impact energy increases the absorbed energy also increases until perforation (rupture) occurs. The equal energy line highlights the point where penetration takes place and the impact energy is almost completely absorbed by the composite in the form of damage. Once rupture occurs the excess impact energy is retained as kinetic energy in the impactor resulting in a diminished absorbed energy. This highlights the perforation threshold of the composite and is shown by a leveling out of the curves Figure 5.8 G. Examining the impact response of the composites further highlights a higher penetration threshold for samples with greater periods of rotation. Therefore, decreasing the fiber size to increase the periods of rotation allows for a greater distribution of energy that helps reduce through thickness damage and increase survivability of the composites.

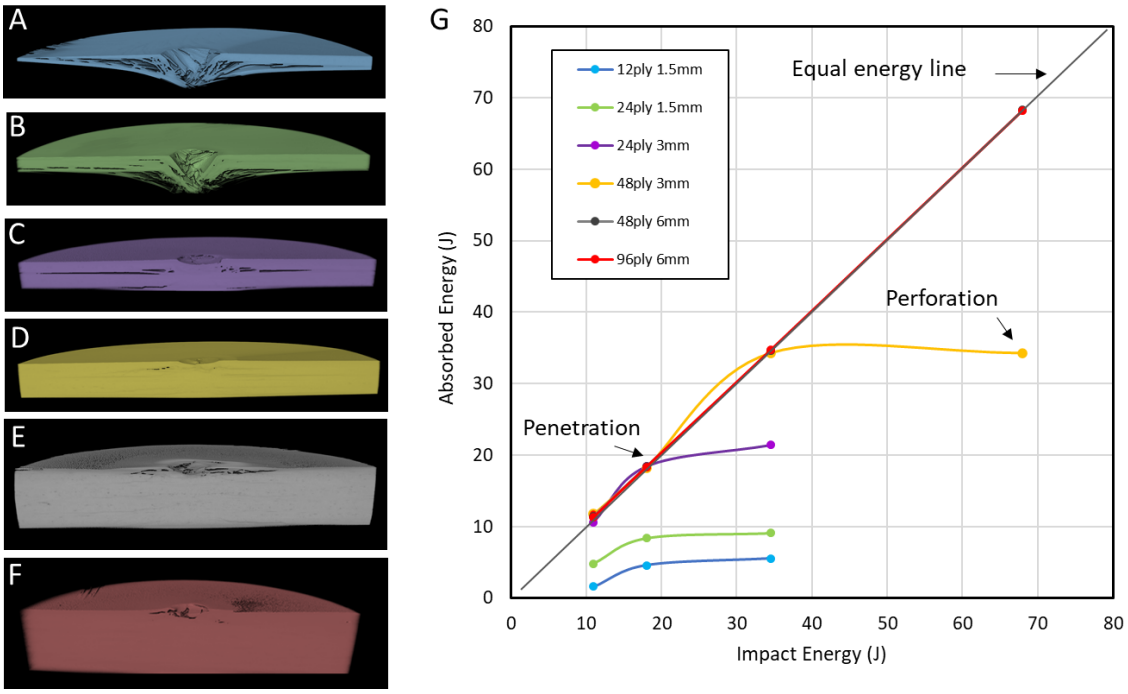

Figure 5. 8. Impact energy profile for all test and computed tomography reconstructions of 20J impacted panels. (A) Post 20J impact CT reconstruction of 12-ply 1.5 mm, (B) 24 ply 1.5 mm, (C) 24-ply 3 mm, (D) 48-ply 3 mm, (E) 48-ply 6 mm, and (F) 96-ply 6 mm composites. (G) Energy profile plot showing the absorbed energy vs impact energy for all composites.

5.4.5 Flexural test of helicoidal FRCs

Helical flat panel composites with thickness of 1.5, 3, and 6 mm, consisting of unidirectional carbon fiber/ epoxy were tested under three-point bending to assess their flexural performance. Figure 5.9 highlights the test setup and stress strain curves of the samples tested in the lengthwise and crosswise orentations. Ovrall, the sampels tested had similar peak flexural stress except for the 12 ply samples. This can be attributed to the incllusion of only one period of rotation with no counter rotation to increas isotropy. Sample dimensions and fiber orientations also play a critical role as samples with a majority their fibers in the shorter axis exhibit lower peak loads and greater extensibility.

Examining the flexural response of the 12-ply 1.5 mm samples in the cross wise orientation reveals an elevated stiffeness as the majority of fibers are oriented in the long axis of the composite. In contrast for the cosswise orientation we sees the greatest compliant in this sample as the fibers are oriented primarily in the short axis leading to properties more characteristic to the polymer matrix. This behavior can be diminished by adding additonal periods of rotation to the composite as displayed by the flexural response of the 24-ply 1.5 mm sample. In summary, samples with fewer layers show greater peak stress.

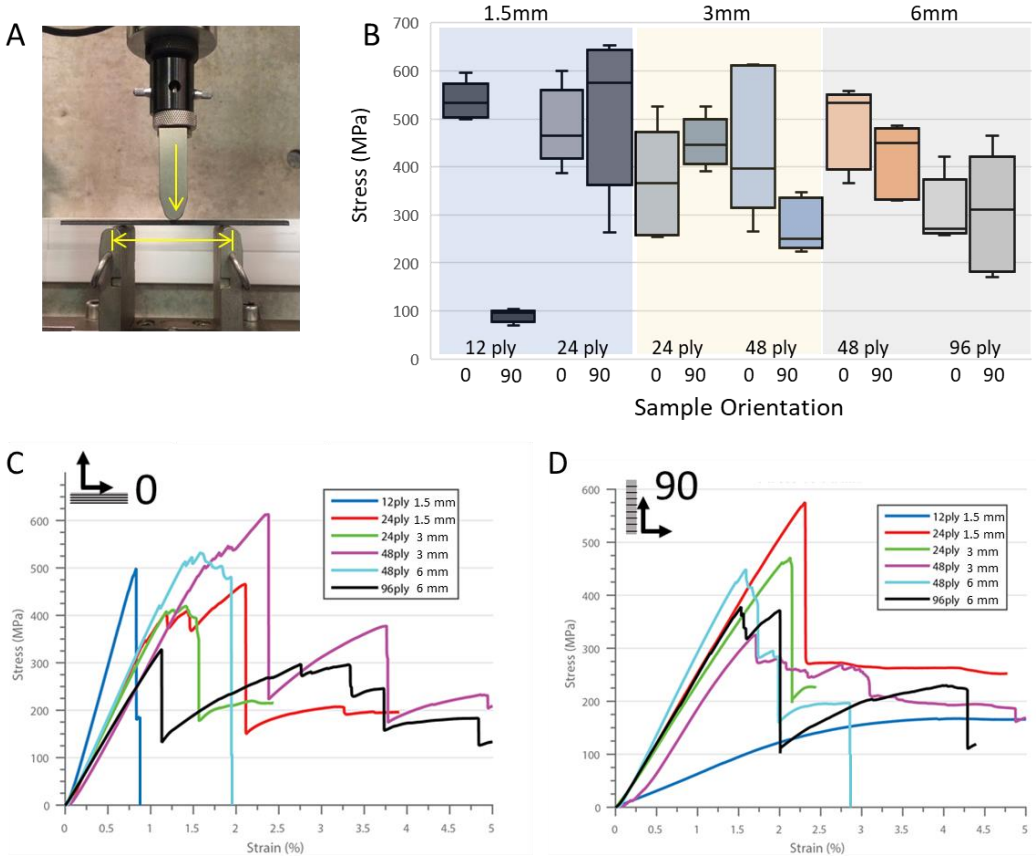

Figure 5. 9. Flexural response of biomimetic composites of number of layers thickness. (A) Mechanical test setup. (B) Variation in flexural stress based on thickness and section orientation of composites. (C) Representative stress versus strain plots of crosswise and (D) lengthwise samples.

Further analyses of the flexural performace highlights the variation modulous between these biomimetic composites (Figure 5.10). It is shown that a trend of improved flexural modulous of the crosswise samples highlighting the benefits of fiber orientation in the composite. Due to the rectangular sample dimensions fiber orientation plays a prodominat role in the modulous of the compsite as the samples with the most fibers in the long direction show the stiffest response.

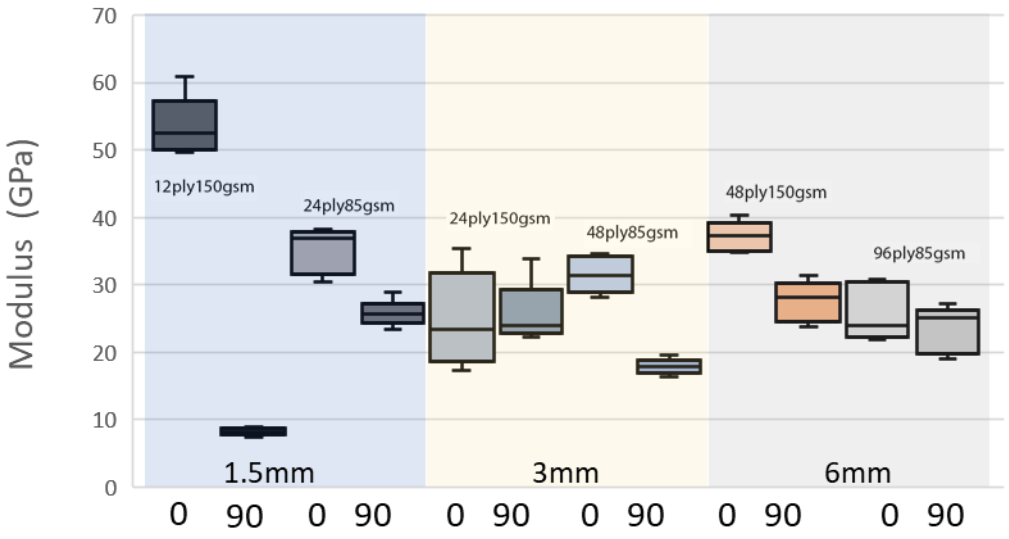

Figure 5. 10. Flexural modulus and toughness of biomimetic composites. Plot highlighting variation in flexural modulus based on thickness and section orientation of composites.

The fracture behavior of the composites were further studied during the flexural test. Figure 5.11 highlights the fracture patterns in the composites under five percent flexural strain. This effect correlates to the decreased toughness and stiffness in the lenghtwise composites. Furthermore, we observe a large delamination in the 12-ply 1.5mm composite in the crosswise orientation and no visible damage in the lengthwise,

highlighting the stiff response of the matrix material as a majority of fibers are placed in the length wise orientation. For these helicoidal composites, the boundary conditions and the depth of the sample resulted in the large delamination as the architecture drives the crack laterally in a twisting motion leading to periodic failure in the 0° axis of the composite. As samples increased in width this effect becomes exacerbated and we see a greater discrepancy in toughness of the length wise and crosswise composites. An alternative test with increased boundary conditions should highlight the benefits of the crack twisting properties of the helicoidal architecture and move past these boundary condition effects.

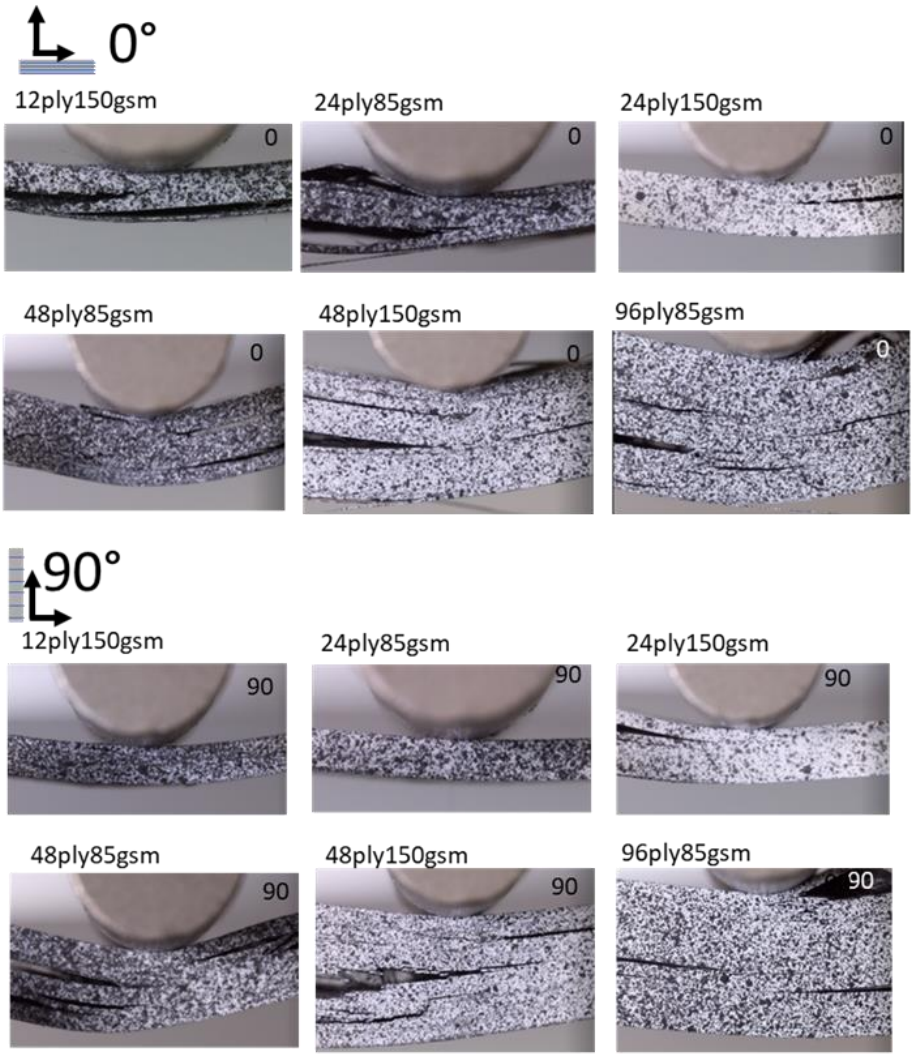

Figure 5. 11. Optical images of fracture of fracture in biomimetic composites at five percent strain. Crosswise orientation samples (top) highlight delamination between layers while lengthwise samples (bottom) show minimal fracture except of the 48 ply variants.

5.4.6 Charpy impact

Composites described in section 5.4.2 were subjected to Charpy impact with 400 J of energy. Figure 5.12 highlights the variance in energy absorbed across three sets of composite panels: prepreg carbon fiber/ epoxy, carbon/ Onyx, and Kevlar/ Onyx. The prepreg panels absorbed the greatest amount of energy followed by the Kevlar/ Onyx and finally the carbon/ onyx for their respective fiber orientation. This can be attributed to the higher degree of fiber density in the prepreg samples and the relatively higher elastic modulus of the epoxy matrix compared to the Onyx material comprised of fiber reinforced nylon. The fracture patterns across the different architectures remained consistent. Serving as a control the 0° and 90° samples show cracks propagate through the material. In contrast, the helicoidal samples propagate energy laterally causing a large degree of delamination.

A comparison of the energy absorbed based on the architectural variation between specimen sets is depicted in Figure 5.12. Prepreg samples with a 90° fiber orientation showed the greatest energy absorption. This was expected as the fibers are oriented perpendicular to the impacting direction causing more energy to fracture the fibers. Yet, this results in a through thickness crack in the composite (Figure 5.12 B). Similarly, the 0° sample shows a bifurcation of the composite as the fiber orientation is parallel with the impacting direction causing a crack to propagate through the material. Unlike the previous sample, fracture occurs due to the failure of the matrix resulting in the lowest amount of energy absorption. The 45° sample absorbed the second greatest amount of energy yet localized the fracture to the center portion of the sample, leading to delamination and separating the top and bottom sections of the composite but not fracturing the left and right

halves (Figure 5.12 B). In contrast, the 16.3° helicoidal sample delaminated to one side but did not fracture into separate parts (Figure 5.13 A). The helicoidal architecture prevented a great degree of fracture in the fibers as seen in the 90° sample and assisted to redirect the crack laterally leading to delamination in one side of the sample. The boundary conditions in the depth of the sample resulted in the large delamination as the architecture drives the crack laterally in a twisting motion leading to periodic delamination in the 0° axis of the helicoid. An alternative impact test with increased boundary conditions should highlight the benefits of the crack twisting behavior of the helicoidal architecture.

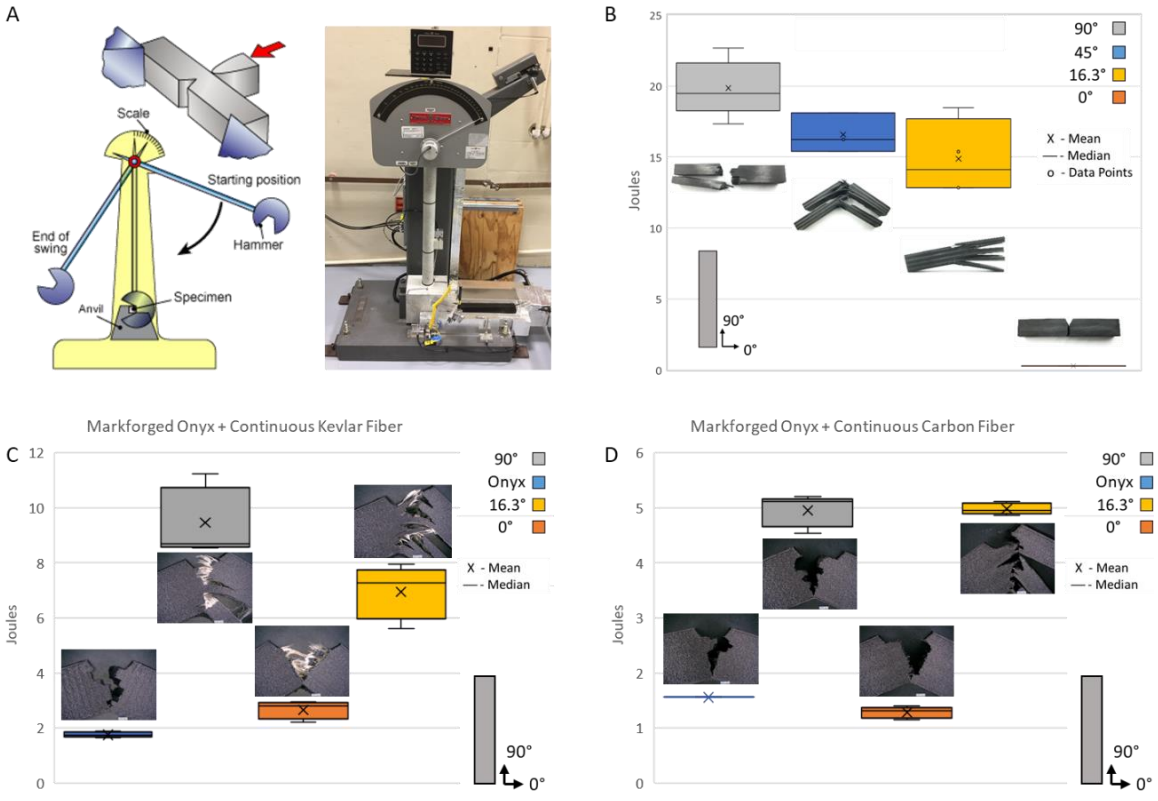

Figure 5. 12. Test setup and Charpy impact results (A) Experimental setup and Tinius Olsen test equipment. (B) Absorbed energy results from fractured prepreg carbon/ epoxy samples. (C) Impact results from additively manufactured Kevlar fiber/ Onyx and (D) Carbon Fiber/ Onyx.

A similar trend in fracture and energy absorption with the 90° sample absorbing the greatest amount of energy and the 0° absorbing the least is observed in samples fabricated with additive manufacturing (Figure 5.12 C-D). Trends deviate when examining the prepreg composites, as the base Onyx material preforms better than the 0° oriented sample (Figure 5.12 D). This results from the printing orientation of the base material and the relatively minimal amount of matrix material in the 0° sample. Since the carbon fibers are relatively brittle and primarily organized in the 0° orientation, the bulk of the energy is absorbed by the failure of the matrix, resulting in the additional amount of Onyx material in the control samples accounting for the small variations in energy absorbed. In contrast, the Kevlar fiber reinforced samples have higher energy absorption than the base Onyx material due to Kevlar's resistance to shear and fracture. This is evident as we observe strands of Kevlar bridging in the 0° samples opposed to the carbon variant where no fibers bridge the two halves (Figure 5.13 D-F). Kevlar's improved energy absorption over carbon is therefore due to these bridging capabilities as the fibers do not fail in shear and bridge the polymer layers instead of fracturing like the carbon.

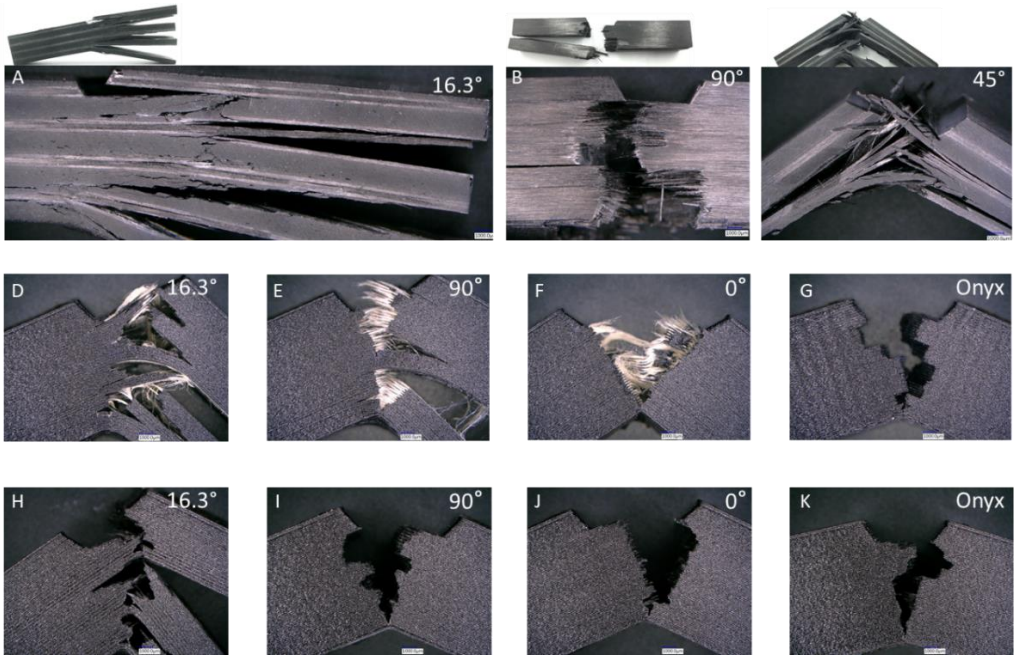

Figure 5. 13. Charpy V-notch post impact fractured samples. (A-C) Carbon/ epoxy samples showing high degree of delamination for the helicoid, fiber fracture for 90° and fracture and delamination for 45°. (D-G) Additively manufactured Kevlar fiber reinforced samples showing fiber bridging in reinforced specimens. (H-K) Additively manufactured Carbon fiber reinforced samples revealing the varying fracture patterns based on fiber orientation. (Scalebars 1mm)

In terms of architecture, the energy absorption is greater in 90° samples than 16.3° helicoidal. It is shown that the energy absorption in the Kevlar samples have larger deviation than that in the carbon. The brittle nature of the carbon and the amount of fiber to matrix results in a small deviation in energy absorbed across architectures as the fracture of the fibers in the 90° sample is offset by the larger degree of delamination present with the 16.3° architecture (Figure 5.13 H-K). This is contrasted in the Kevlar samples, as we see fiber bridging between layers causing a greater amount of energy to be absorbed in the 90° composite compared to delamination in the helicoidal sample. The helicoidal architecture primarily causes failure of the matrix with less through thickness fracture of the fiber structure leading to a larger damage area but less penetration.

5.5 Conclusions

In this work, we examined the potential for fabricating biomimetic composites inspired by the helicoidal fibrous architecture found in arthropod cuticles. We investigated flexural and impact behavior of composite samples with three different mechanical tests: three-point bending, drop tower impact and Charpy impact tests. It is shown the peak stress, energy absorption and fracture effects depend on the number of layers.

For drop weight impact tests, composites with an increased number of periodic rotations showed larger amount of energy absorption than composites with less layers but the same thickness. Analyzing internal damage, CT scans revealed relatively lesser delamination in the samples with a greater number of rotations per thickness. This result highlights the ability for the helicoidal architecture to effectively transfer impact load to the surrounding matrix material and thus prevent structural failure throughout the samples.

In the flexural test, the modulous and peak stress are highly dependent on the fiber orientations. Composites with more periods of rotation per thickness show larger toughness. Three-point bending remains a non-ideal characterization method for the helicoidal architecture due to the sample geometry. This rectangular geometry provides a non-uniform boundary condition that favors fibers in the long axis of the sample. The ability of the helicoid to transfer load laterally further becomes mitigated by a confined boundary. Moving forward a more comprehensive test with larger boundary conditions need to be conducted. Ideally this architecture would be applied to curved structures that would provide increased boundary condition allowing the visualization of wide damage spread.

For Charpy impact tests, prepreg composites showed the highest energy absorption upon impact compared to the additively manufactured samples, an expected result due to the fiber density of the composite. Examining the effects of architecture, the 90° samples absorbed the greatest amount of energy yet fractured in the center. In contrast, the helicoidal composites prominently delaminated due to the architecture redirecting the crack path in a twisting direction. Moreover, the additive manufactured samples showed similar fracture results but absorbed a lower amount of energy. Kevlar samples performs better than carbon due to their resistance to shear. For the helicoidal composites, facture results highlight a decrease in through thickness damage resulting from a consistent fracture of the matrix leading to greater survivability of composites. These results provide valuable information regarding the role of architecture and the effects modulus mismatch that drives crack propagation providing a useful avenue for the helicoidal architecture in delocalizing damage and improving energy absorption.

Chapter 6: Summary, Conclusions and Future Work

6.1 Summary and conclusions

The objective of this study was to characterize the structural and compositional features of the diabolical ironclad beetle *P. diabolicus*, measure the resulting mechanical responses that contribute to compression resistance and translate this knowledge to the development of light-weight tough composites. Initially the bulk compression response of the organism was assessed to identify its resistance to predation. Result showed that *P. diabolicus* was able to withstand the greatest load per mass. Since beetles are typically composed of alpha chitin fibers embedded in a proteinaceous matrix this signified a variations in the chemical and or microstructural architecture in the organism. Microscopy characterization at the key interfacial regions of interest highlighted jigsaw interfacial features that assisted to toughen the joints. The geometry and number of these features assisted to evenly distribute localized stresses in the region and increases toughness. Laminated in nature, these interfacial features provided an alternative failure mode prominently delaminating to relieve stress. These design strategies were applied to the fabrication of interfacial composite materials that showed improve toughening over current engineering fasteners.

Residing in an arid environment of southern California, the ironclad must hydrate itself and its cuticle to maintain its mechanical properties. Initial contact angle experiments highlight the super hydrophilic response of the ironclad elytra as water immediately wicks throughout its surface. Microscopy analysis of this region highlights a dense concentration of leaflike setae with micro and nano channels that facilitate water collection and transport

through capillary forces. Micro computed tomography scans of the internal structure highlight a series of pore canals connected to the setae. This pore canal network funnels into a larger volume inside the elytra known as the hemolymph space serving as a storage point for the collected fluid. The addition of this reservoir of fluid and pore canal network ensure the hydration of the cuticle maintaining the structures tough mechanical properties. Further analysis highlights the ability for the elytra to serve as an affective thermal barrier. Ultimately the adaptation of leaf like setae and a vast pore canal network allows *P. diabolicus* to collect transport and store water in an arid environment.

Examining evolutionary variation in the elytra of flying and terrestrial beetles we begin to see key ultra and microstructural features that allow these organisms to thrive in their relative environments. Leveraging the previous study, we compare the macro and micro-structural mechanical property relationship of the flying *T. dichotomus* (rhinoceros beetle) and terrestrial *P. diabolicus* (diabolical ironclad beetle) elytra by examining the changes in composition, cuticle density, fiber orientation, and degree of matrix cross-linking in these biological composites. Optical microscopy highlights regional variations in the medial suture, bulk cuticle, and lateral interfaces. Focusing on the bulk structure we see an arid nature in elytra of the flying beetle with CT scans highlighting only 45% of the volume is occupied by structural material. In contrast we see a 11% porosity in its terrestrial counterpart. This variation highlights an optimization for flight in one species while the other is more suited to engage predators. Upon examination of the microstructural features we see an incorporation of z pinning through thickness fibers in the endocuticle layers of the terrestrial beetle. Three-point bend test highlight the ability for these fibers to stiffen

the structure while tensile test suggest that these features prevent reorientation of the fiber bundles and provide additional toughening. Upon examining the puncture response of the elytra, we see microstructure on the ironclad allows for a stiff response with little deformation and the opposite response for the flying elytra. Examining the cross-sectional features, indentation maps and FTIR analysis further highlight gradations in stiffness and sclerotization moving deeper into both cuticles. This work provides key insights into the fabrication of composite materials as it provides a blueprint for the chemical and structural variation needed to tune a fibrous composite for flight or impact resistance.

Applying the design insights gleaned from previous chapters, biomimetic carbon fiber epoxy composites were fabricated and tested to determine their strength and toughness based on number of layers and sample thickness. Helicoidal samples used a 16.3° rotation angle between successive layers and were fabricated using two different areal weights of fibers in three final composite thicknesses, 1.5 mm, 3 mm and 6mm, resulting in six sample variations, 12-ply 1.5mm, 24-ply 1.5mm, 24-ply 3mm, 28-ply 3mm, 48-ply 6mm, 96-ply 6mm. Drop weight impact showed a consistent trend as composites with more periods of rotation per thickness absorbed a greater amount of energy before failing. Similar trends continued as flexural test saw the samples with more periods of rotation consistently haver greater toughness. Yet in both test these samples exhibited lower flexural modulus suggesting a favorability due to fiber orientation. These test highlight the ability for the helicoidal architecture to dissipate energy in the matrix material leading to delamination of the composite instead to fracture of the fibers. Charpy impact further highlights this as the helicoidal samples saw prominent delamination, failure of the

surrounding matrix material, instead of fiber fracture seen in the unidirectional and quasi isotropic controls. This work provides key insights into the incorporation of helicoidal architecture into engineering composite materials and the importance of additional periods of rotation in the laminate.

Ultimately this work presents an encompassing study of the structure function relationship of *P. diabolicus* and the incorporation of biological architectural designs into composite materials to increase toughness.

References

1. M. C. Roco, The long view of nanotechnology development: The National Nanotechnology Initiative at 10 years. *J. Nanoparticle Res.* **13**, 427–445 (2011).

2. NSTC, Materials Genome Initiative for Global Competitiveness. *Genome* (2011) (available at http://www.whitehouse.gov/sites/default/files/microsites/ostp/materials_genome_initiative-final.pdf).

3. J. W. C. Dunlop, P. Fratzl, Biological Composites. *Annu. Rev. Mater. Res.* **40**, 1–24 (2010).

4. R. O. Ritchie, The conflicts between strength and toughness. *Nat. Mater.* **10**, 817–822 (2011).

5. M. Holmes, Global carbon fibre market remains on upward trend. *Reinf. Plast.* **58**, 38–45 (2014).

6. M. Vozoff, J. Couluris, SpaceX products - Advancing the use of space. *Sp. 2008 Conf.*, 1–9 (2008).

7. G. Savage, in *SPE Automotive and Composites Division - 8th Annual Automotive Composites Conference and Exhibition* (ACCE 2008 - The Road to Lightweight Performance, 2008), vol. 1, pp. 109–139.

8. J. M. Robert, *Mechanics of Composite Materials* (Scripta Book Company, ed. 2, 1975).

9. X. Jiang, C. Guo, X. Cao, Z. Lu, Design of the lightweight structure and its mechanical properties. **461**, 57–62 (2014).

10. M. Endo, *High-Performance and Specialty Fibers* (Springer Japan, Society of., 2016).

11. D. D. Edie, The effect of processing on the structure and properties of carbon fibers. *Carbon N. Y.* **36**, 345–362 (1998).

12. C. Guo, W. W. Song, Z. D. Dai, Structural design inspired by beetle elytra and its mechanical properties. *Chinese Sci. Bull.* **57**, 941–947 (2012).

13. M. A. Meyers, P. Y. Chen, A. Y. M. Lin, Y. Seki, Biological materials: Structure and mechanical properties. *Prog. Mater. Sci.* **53**, 1–206 (2008).

14. P. Y. Chen, J. McKittrick, M. A. Meyers, Biological materials: Functional adaptations and bioinspired designs. *Prog. Mater. Sci.* **57**, 1492–1704 (2012).

15. P. Fratzl, R. Weinkamer, Nature's hierarchical materials. *Prog. Mater. Sci.* **52**, 1263–1334 (2007).

16. S. E. Naleway, M. M. Porter, J. McKittrick, M. A. Meyers, Structural Design Elements in Biological Materials: Application to Bioinspiration. *Adv. Mater.* **27**, 5455–5476 (2015).

17. M. Connections, REVIEW Structural Biological Materials: Critical Mechanics-Materials Connections, 773–780 (2013).

18. P. Chen, J. Mckittrick, M. André, Biological materials : Functional adaptations and bioinspired designs. *Prog. Mater. Sci.* **57**, 1492–1704 (2012).

19. Q. Chen, N. M. Pugno, Bio-mimetic mechanisms of natural hierarchical materials : A review. *J. Mech. Behav. Biomed. Mater.* **19**, 3–33 (2013).

20. F. P. Dunlop, John W.C., Biological Composites. *Annu. Rev. Mater. Res.*, 1–24 (2010).

21. U. G. K. Wegst, M. F. Ashby, The mechanical efficiency of natural materials. *Philos. Mag.* **84**, 2167–2186 (2004).

22. J. Sun, B. Bhushan, Hierarchical structure and mechanical properties of nacre: a review. *RSC Adv.* **2**, 7617 (2012).

23. U. G. K. Wegst, H. Bai, E. Saiz, A. P. Tomsia, R. O. Ritchie, Bioinspired structural materials. **14**, 23–36 (2015).

24. F. Barthelat, H. D. Espinosa, An experimental investigation of deformation and fracture of nacre-mother of pearl. *Exp. Mech.* **47**, 311–324 (2007).

25. I. A. Malik, F. Barthelat, Bioinspired sutured materials for strength and toughness: Pullout mechanisms and geometric enrichments. *Int. J. Solids Struct.* **138**, 118–133 (2018).

26. Y. Shao, H. P. Zhao, X. Q. Feng, H. Gao, Discontinuous crack-bridging model for fracture toughness analysis of nacre. *J. Mech. Phys. Solids*. **60**, 1400–1419 (2012).

27. J. Najem, S. A. Sarles, B. Akle, D. J. Leo, Biomimetic jellyfish-inspired underwater vehicle actuated by ionic polymer metal composite actuators. *Smart Mater. Struct.* **21** (2012), doi:10.1088/0964-1726/21/9/094026.

28. Y. Yamamoto *et al.*, Mimicking photosynthesis with man-made leaves. *Chem. Sci.* **5**, 639–648 (2014).

29. J. Tong, J. Sun, D. Chen, S. Zhang, Geometrical features and wettability of dung beetles and potential biomimetic engineering applications in tillage implements. *Soil Tillage Res.* **80**, 1–12 (2005).

30. J. Nickerl, M. Tsurkan, R. Hensel, C. Neinhuis, C. Werner, The multi-layered protective cuticle of Collembola : a chemical analysis. *J. R. Soc. Interface*. **11**, 20140619 (2014).

31. S. Deville, Freeze-casting of porous ceramics: A review of current achievements and issues. *Adv. Eng. Mater.* **10**, 155–169 (2008).

32. U. G. K. Wegst, H. Bai, E. Saiz, A. P. Tomsia, R. O. Ritchie, Bioinspired structural materials. *Nat. Mater.* **14**, 23–36 (2015).

33. A. Tanay *et al.*, Tough, Bio-Inspired Hybrid Materials. *Science (80-.).* **322**, 1516–1520 (2008).

34. L. Drive, Fog Basking by the Namib Desert beetle, Onymacris unguiclaris. *Nature*. **262**, 284–285 (1976).

35. J. Lomakin *et al.*, Mechanical properties of the beetle elytron, a biological composite material. *Biomacromolecules*. **12**, 321–335 (2011).

36. K. Peschke, T. Eisner, Defensive secretion of the tenebrionid beetle, Blaps mucronata: Physical and chemical determinants of effectiveness. *J. Comp. Physiol. A*. **161**, 377–388 (1987).

37. S. W. Nicolson, S. A. Hanrahan, Diuresis in a desert beetle? hormonal control of the malpighian tubules of Onymacris plana (Coleoptera: Tenebrionidae). *J. Comp. Physiol. B*. **156**, 407–413 (1986).

38. R. A. Crowson, *The Biology of the Coleoptera* (Academic Press, New York, 1981).

39. B. W. Cribb *et al.*, Hardness in arthropod exoskeletons in the absence of transition metals. *Acta Biomater.* **6**, 3152–3156 (2010).

40. R. Dennell, The structure and lamination of some arthropod cuticles. *Zool. J. Linn. Soc.* **58**, 159–164 (1976).

41. J. F. V Vincent, U. G. K. Wegst, Design and mechanical properties of insect cuticle. *Arthropod Struct. Dev.* **33**, 187–199 (2004).

42. Z. DE Architektur von Käferelytren Thomas Van Kamp, H. Greven, On the Architecture of Beetle Elytra. *Entomol. heute*. **22**, 191–204 (2010).

43. J. Sun, B. Bhushan, Structure and mechanical properties of beetle wings: a review. *RSC Adv.* **2**, 12606 (2012).

44. Z. Fu, G. Hang, T. Jin, Z. Jiang, M. Yunhai, Research on elytron section microstructure of four species beetles and biomimetic models (2011), doi:10.3969/j.issn.1002-6819.2011.06.019.

45. J. F. V Vincent, Arthropod cuticle: A natural composite shell system. *Compos. Part A Appl. Sci. Manuf.* **33**, 1311–1315 (2002).

46. C. He, Q. Zu, J. Chen, M. N. Noori, A review of the mechanical properties of beetle elytra and development of the biomimetic honeycomb plates. *J. Sandw. Struct. Mater.* **17**, 399–416 (2015).

47. K. Jayaram, R. J. Full, Cockroaches traverse crevices, crawl rapidly in confined spaces, and inspire a soft, legged robot. *Proc. Natl. Acad. Sci.* **113**, 1–8 (2016).

48. A. J. Clark, J. D. Triblehorn, Mechanical properties of the cuticles of three cockroach species that differ in their wind-evoked escape behavior. *PeerJ.* **2**, e501 (2014).

49. T. van de Kamp, A. Riedel, H. Greven, Micromorphology of the elytral cuticle of beetles, with an emphasis on weevils (Coleoptera: Curculionoidea). *Arthropod Struct. Dev.* **45**, 14–22 (2016).

50. I. A. Foley, A Review of the Ironclad Beetles of the World (Coleoptera Zopheridae: Phellopsini and Zopherini) (2006).

51. N. P. Lord, Systematics within the zopherid complex (Coleoptera: Tenebrionoidea), 409 (2013).

52. M. García-París, M. M. Coca-Abia, G. Parra-Olea, Re-evaluation of the genera Phloeodes, Noserus and Nosoderma (Coleoptera: Zopheridae) with description of a new species of Nosoderma from northern México. *Ann. la Société Entomol. Fr. (Nouvelle série)*. **42**, 215–230 (2006).

53. I. A. Foley, M. Ivie, *A phylogenetic analysis of the tribe Zopherini with a review of the species and generic classification (Coleoptera: Zopheridae)* (Magnolia Press, 2008).

54. V. Le Nguyen, thesis, Mississippi State University (2017).

55. S. O. Andersen, Insect cuticular sclerotization: A review. *Insect Biochem. Mol. Biol.* **40**, 166–178 (2010).

56. R. Roer, S. Abehsera, A. Sagi, Exoskeletons across the Pancrustacea : Comparative Morphology , Physiology , Biochemistry and Genetics. *Integr. Comp. Biol.* **55**, 771–791 (2015).

57. A. Baselga, E. Recuero, G. Parra-Olea, M. García-París, Phylogenetic patterns in zopherine beetles are related to ecological niche width and dispersal limitation. *Mol. Ecol.* **20**, 5060–5073 (2011).

58. Q. Kan, W. Yan, G. Kang, Q. Sun, Oliver-Pharr indentation method in determining elastic moduli of shape memory alloys - A phase transformable material. *J. Mech. Phys. Solids*. **61**, 2015–2033 (2013).

59. S. S. Chaudhari *et al.*, Knickkopf protein protects and organizes chitin in the newly synthesized insect exoskeleton. *Proc. Natl. Acad. Sci.* **108**, 17028–17033 (2011).

60. Y. Arakane *et al.*, Formation of rigid, non-flight forewings (Elytra) of a beetle requires two major cuticular proteins. *PLoS Genet.* **8** (2012).

61. M. Y. Noh *et al.*, Two major cuticular proteins are required for assembly of horizontal laminae and vertical pore canals in rigid cuticle of Tribolium castaneum. *Insect Biochem. Mol. Biol.* **53**, 22–29 (2014).

62. M. Y. Noh, S. Muthukrishnan, K. J. Kramer, Y. Arakane, Cuticle formation and pigmentation in beetles. *Curr. Opin. Insect Sci.* **17**, 1–9 (2016).

63. M. Y. Noh, S. Muthukrishnan, K. J. Kramer, Y. Arakane, Tribolium castaneum RR-1 Cuticular Protein TcCPR4 Is Required for Formation of Pore Canals in Rigid Cuticle. *PLOS Genet.* **11** (2015), doi:10.1371/journal.pgen.1004963.

64. Y. Arakane *et al.*, Formation of Rigid, Non-Flight Forewings (Elytra) of a Beetle Requires Two Major Cuticular Proteins. *PLoS Genet.* **8**, e1002682 (2012).

65. Z. Dai, Y. Zhang, X. Liang, J. Sun, Coupling between elytra of some beetles: Mechanism, forces and effect of surface texture. *Sci. China, Ser. C Life Sci.* **51**, 894–901 (2008).

66. A. BASELGA, E. RECUERO, G. PARRA-OLEA, M. GARCÍA-PARÍS, Phylogenetic patterns in zopherine beetles are related to ecological niche width and dispersal limitation. *Mol. Ecol.* **20**, 5060–5073 (2011).

67. M. Polihronakis, M. S. Caterino, Contrasting patterns of phylogeographic relationships in sympatric sister species of ironclad beetles (Zopheridae: Phloeodes spp.) in California's Transverse Ranges. *BMC Evol. Biol.* **10**, 195 (2010).

68. P. E. Schilman, A. Kaiser, J. R. B. Lighton, Breathe softly, beetle: Continuous gas exchange, water loss and the role of the subelytral space in the tenebrionid beetle, Eleodes obscura. *J. Insect Physiol.* **54**, 192–203 (2008).

69. M. García-París, M. M. Coca-Abia, G. Parra-Olea, Re-evaluation of the genera Phloeodes, Noserus and Nosoderma (Coleoptera: Zopheridae) with description of a new species of Nosoderma from northern México. *Ann. la Soc. Entomol. Fr.* **42**, 215–230 (2006).

70. Michael L. Draney, The Subelytral Cavity of Desert Tenebrinoids. *Florida Entomol.* **76**, 539–549 (1993).

71. B. Y. C. N. Slobodchikoff, K. I. M. Wismann, A Function of the Subelytral Chamber of Tenebrionid Beetles. *J. Exp. Biol.* **90**, 109–114 (1981).

72. J. J. Connor, S. Faraji, *Fundamentals of Structural Engineering* (Springer, New York, ed. 2, 2013).

73. S. N. Gorb, Frictional surfaces of the elytra-to-body arresting mechanism in tenebrionid beetles (Coleoptera : Tenebrionidae): Design of co-opted fields of microtrichia and cuticle ultrastructure. *Int. J. Insect Morphol. Embryol.* **27**, 205–225 (1998).

74. S. Enders, N. Barbakadse, S. N. Gorb, E. Arzt, Exploring Biological Surfaces by Nanoindentation. *J. Mater. Res.* **19**, 880–887 (2004).

75. S. N. Gorb *et al.*, Structural Design and Biomechanics of Friction-Based Releasable Attachment Devices in Insects. *Integr. Comp. Biol.* **42**, 1127–1139 (2002).

76. S. N. Gorb, Frictional Surfaces of the Elytra-to-Body Arresting Mechanismin Tenebrinoid Beetles (Colioptera : Tenebrionidae) : Designe of Co-opted Fields of Microtrichia and Cuticle Ultrastructure. *Int. J. Insect Morphol. Embryol.* **27**, 205–225 (1998).

77. E. Lin, Y. Li, C. Ortiz, M. C. Boyce, 3D printed, bio-inspired prototypes and analytical models for structured suture interfaces with geometrically-tuned deformation and failure behavior. *J. Mech. Phys. Solids*. **73**, 166–182 (2014).

78. M. S. Hosseini, F. A. Cordisco, P. D. Zavattieri, Analysis of bioinspired non-interlocking geometrically patterned interfaces under predominant mode I loading. *J. Mech. Behav. Biomed. Mater.* **96**, 244–260 (2019).

79. I. A. Malik, M. Mirkhalaf, F. Barthelat, Bio-inspired “Jigsaw”-like interlocking sutures: Modeling, optimization, 3D printing and testing. *J. Mech. Phys. Solids*. **102**, 224–238 (2017).

80. M. Mirkhalaf, F. Barthelat, Design, 3D printing and testing of architectured materials with bistable interlocks. *Extrem. Mech. Lett.* **11**, 1–7 (2016).

81. Y. Li, C. Ortiz, M. C. Boyce, A generalized mechanical model for suture interfaces of arbitrary geometry. *J. Mech. Phys. Solids*. **61**, 1144–1167 (2013).

82. C. A. Tweedie *et al.*, Enhanced stiffness of amorphous polymer surfaces under confinement of localized contact loads. *Adv. Mater.* **19**, 2540–2546 (2007).

83. E. Lin, Y. Li, C. Ortiz, M. C. Boyce, 3D printed, bio-inspired prototypes and analytical models for structured suture interfaces with geometrically-tuned deformation and failure behavior. *J. Mech. Phys. Solids*. **73**, 166–182 (2014).

84. G. Melhem, S. Bandyopadhyay, C. Sorrell, Use of Aerospace Fasteners in Mechanical and Structural Applications. *Ann. Mater. Sci. Eng.* **1**, 1–5 (2014).

85. Y. Bouligand, Twisted Fibrous Arrangments in Biological Materials and Cholesteric Measophases. *Tissue Cell*. **4**, 189–217 (1972).

86. J. C. Weaver *et al.*, The Stomatopod Dactyl Club: A Formidable Damage-Tolerant Biological Hammer. *Science (80-.).* **336**, 1275–1280 (2012).

87. L. K. Grunenfelder *et al.*, Bio-inspired impact-resistant composites. *Acta Biomater.* **10**, 3997–4008 (2014).

88. N. Suksangpanya, N. A. Yaraghi, R. B. Pipes, D. Kisailus, P. Zavattieri, International Journal of Solids and Structures Crack twisting and toughening strategies in Bouligand architectures. **150**, 83–106 (2018).

89. M. Andrew Jansen, S. S. Singh, N. Chawla, N. M. Franz, A multilayer micromechanical model of the cuticle of Curculio longinasus Chittenden, 1927 (Coleoptera: Curculionidae). *J. Struct. Biol.* **195**, 139–158 (2016).

90. P. Chen, A. Y. Lin, J. McKittrick, M. Andre, Structure and mechanical properties of crab exoskeletons. **4**, 587–596 (2008).

91. W. Yang *et al.*, Structure and fracture resistance of alligator gar (Atractosteus spatula) armored fish scales. *Acta Biomater.* **9**, 5876–5889 (2013).

92. M. A. Kasapi, J. M. Gosline, Design Complexity and Fracture Control in the Equine Hoof Wall. *J. Exp. Biol. 200,*. **200**, 1639–1659 (1997).

93. P. Chen, A. G. Stokes, J. McKittrick, Comparison of the structure and mechanical properties of bovine femur bone and antler of the North American elk (Cervus elaphus canadensis). *Acta Biomater.* **5**, 693–706 (2009).

94. R. T. V Chintapalli, J. F. Hillyer, Hemolymph circulation in insect flight appendages: physiology of the wing heart and circulatory flow in the wings of the mosquito, Anopheles gambiae. *J. Exp. Biol.*, 3945–3951 (2016).

95. D. Klocke, H. Schmitz, Water as a major modulator of the mechanical properties of insect cuticle. *Acta Biomater.* **7**, 2935–2942 (2011).

96. M. Sun *et al.*, Compound Microstructures and Wax Layer of Beetle Elytral Surfaces and Their Influence on Wetting Properties. *PLoS One*. **7** (2012).

97. A. A. Darhuber, S. M. Troian, Dynamics of capillary spreading along hydrophilic microstripes. *Phys. Rev. E - Stat. Physics, Plasmas, Fluids, Relat. Interdiscip. Top.* **64**, 8 (2001).

98. J. Wang *et al.*, Hydrophobic sol-gel channel patterning strategies for paper-based microfluidics. *Lab Chip*. **14**, 691–695 (2014).

99. a R. Parker, C. R. Lawrence, Water capture by a desert beetle. *Nature*. **414**, 33–34 (2001).

100. M. Tani, D. Ishii, S. Ito, T. Hariyama, M. Shimomura, Capillary Rise on Legs of a Small Animal and on Artificially Textured Surfaces Mimicking Them. **9** (2014), doi:10.1371/journal.pone.0096813.

101. D. Ishii *et al.*, Water transport mechanism through open capillaries analyzed by direct surface modifications on biological surfaces. *Sci. Rep.* **3**, 3–7 (2013).

102. S. Kehl, K. Dettner, Surviving submerged-Setal tracheal gills for gas exchange in adult rheophilic diving beetles. *J. Morphol.* **270**, 1348–1355 (2009).

103. D. Ishii *et al.*, Water transport mechanism through open capillaries analyzed by direct surface modifications on biological surfaces. *Sci. Rep.* **3**, 1–5 (2013).

104. A. A. Darhuber, S. M. Troian, W. W. Reisner, Dynamics of capillary spreading along hydrophilic microstripes. *Phys. Rev. E - Stat. Physics, Plasmas, Fluids, Relat. Interdiscip. Top.* **64**, 031603-1-031603–8 (2001).

105. A. Ponomarenko, D. Quéré, C. Clanet, A universal law for capillary rise in corners. *J. Fluid Mech.* **666**, 146–154 (2011).

106. L. A. Romero, F. G. Yost, Flow in an open channel capillary. *J. Fluid Mech.* **322**, 109–129 (1996).

107. J. Y. Chung, J. P. Youngblood, C. M. Stafford, Anisotropic wetting on tunable micro-wrinkled surfaces. *Soft Matter*. **3**, 1163–1169 (2007).

108. A. Y. Vorobyev, C. Guo, Water sprints uphill on glass. *J. Appl. Phys.* **108**, 10–14 (2010).

109. N. F. Hadley, M. R. Warburg, Water loss in three species of xeric-adapted isopods: Correlations with cuticular lipids. *Comp. Biochem. Physiol. -- Part A Physiol.* **85**, 669–672 (1986).

110. K. Hoshino, S. Nakaba, H. Inoue, K. Iwabuchi, Structure and development of male pheromone gland of longicorn beetles and its phylogenetic relationships within the tribe Clytini. *J. Exp. Zool. Part B Mol. Dev. Evol.* **324**, 68–76 (2015).

111. P. Y. Chen, A. G. Stokes, J. McKittrick, Comparison of the structure and mechanical properties of bovine femur bone and antler of the North American elk (Cervus elaphus canadensis). *Acta Biomater.* **5**, 693–706 (2009).

112. S. E. Naleway, M. M. Porter, J. McKittrick, M. A. Meyers, Structural Design Elements in Biological Materials: Application to Bioinspiration. *Adv. Mater.* **27**, 5455–5476 (2015).

113. G. Pass, Beyond aerodynamics: The critical roles of the circulatory and tracheal systems in maintaining insect wing functionality. *Arthropod Struct. Dev.* **47**, 391–407 (2018).

114. J. Bico, C. Tordeux, D. Quéré, Rough wetting. *Europhys. Lett.* **55**, 214–220 (2001).

115. C. N. Slobodchikoff, K. Wismann, A Function of the Subelytral Chamber of Tenebrionid Beetles. *J. Exp. Biol.* **90**, 109–114 (1981).

116. M. L. Draney, The Subelytral Cavity of Desert Tenebrionids. *Florida Entomol.* **76**, 549 (1993).

117. W. J. Hamilton, M. K. Seely, Fog basking by the Namib Desert beetle, Onymacris unguicularis. *Nature*. **262**, 284–285 (1976).

118. T. Nørgaard, M. Dacke, Fog-basking behaviour and water collection efficiency in Namib Desert Darkling beetles. *Front. Zool.* **7**, 23 (2010).

119. L. Courbin *et al.*, Imbibition by polygonal spreading on microdecorated surfaces. *Nat. Mater.* **6**, 661–664 (2007).

120. C. Ishino, M. Reyssat, E. Reyssat, K. Okumura, D. Quéré, Wicking within forests of micropillars. *Epl*. **79**, 6–11 (2007).

121. P. C. Lin, S. Yang, Mechanically switchable wetting on wrinkled elastomers with dual-scale roughness. *Soft Matter*. **5**, 1011–1018 (2009).

122. S. Kehl, K. Dettner, Surviving submerged - Setal tracheal gills for gas exchange in adult rheophilic diving beetles. *J. Morphol.* **270**, 1348–1355 (2009).

123. J. Chen, J. Xie, Z. Wu, E. M. A. Elbashiry, Y. Lu, Review of beetle forewing structures and their biomimetic applications in China: (I) on the structural colors and the vertical and horizontal cross-sectional structures. *Mater. Sci. Eng. C*. **55**, 605–619 (2015).

124. D. D. McKenna *et al.*, The evolution and genomic basis of beetle diversity. *Proc. Natl. Acad. Sci. U. S. A.* **116**, 24729–24737 (2019).

125. S. S. Chaudhari *et al.*, Knickkopf protein protects and organizes chitin in the newly synthesized insect exoskeleton. *Proc. Natl. Acad. Sci. U. S. A.* **108**, 17028–17033 (2011).

126. T. Hunt *et al.*, A comprehensive phylogeny of beetles reveals the evolutionary origins of a superradiation. *Science (80-.).* **318**, 1913–1916 (2007).

127. T. Van de Kamp *et al.*, Beetle elytra as role models for lightweight building construction Beetle Elytra as Role Models. *Entomol. heute*. **27**, 149–158 (2015).

128. J. Chen, J. Xie, Z. Wu, E. M. A. Elbashiry, Y. Lu, Review of beetle forewing structures and their biomimetic applications in China: (I) on the structural colors and the vertical and horizontal cross-sectional structures. *Mater. Sci. Eng. C*. **55**, 605–619 (2015).

129. J. Chen *et al.*, Review of beetle forewing structures and their biomimetic applications in China: (I) on the structural colors and the vertical and horizontal cross-sectional structures. *Mater. Sci. Eng. C*. **55**, 605–619 (2015).

130. T. van de Kamp, A. Riedel, H. Greven, Micromorphology of the elytral cuticle of beetles, with an emphasis on weevils (Coleoptera: Curculionoidea). *Arthropod Struct. Dev.* **45**, 14–22 (2016).

131. M. Polihronakis, M. S. Caterino, Contrasting patterns of phylogeographic relationships in sympatric sister species of ironclad beetles (Zopheridae: Phloeodes spp.) in California's Transverse Ranges. *BMC Evol. Biol.* **10**, 195 (2010).

132. W. Kojima *et al.*, Rhinoceros Beetles Suffer Male-Biased Predation by Mammalian and Avian Predators Rhinoceros Beetles Suffer Male-Biased Predation by Mammalian. **31**, 109–115.

133. A. Kitchener, An analysis of the forces of fighting of the blackbuck (Antilope cervicapra) and the bighorn sheep (Ovis canadensis) and the mechanical design of the horn of bovids. *J. Zool.* **214**, 1–20 (1988).

134. T. Eisner, D. J. Aneshansley, Spray aiming in the bombardier beetle: Photographic evidence. *Proc. Natl. Acad. Sci. U. S. A.* **96**, 9705–9709 (1999).

135. T. Hörnschemeyer, J. Bond, P. G. Young, Analysis of the functional morphology of mouthparts of the beetle Priacma serrata, and a discussion of possible food sources. *J. Insect Sci.* **13**, 126 (2013).

136. H. Fabritius *et al.*, *Chitin in the Exoskeletons of Arthropoda: From Ancient Design to Novel Materials Science* (2011; http://link.springer.com/10.1007/978-90-481-9684-5), vol. 34.

137. T. van de Kamp *et al.*, Comparative thorax morphology of death-feigning flightless cryptorhynchine weevils (Coleoptera: Curculionidae) based on 3D reconstructions. *Arthropod Struct. Dev.* **44**, 509–523 (2015).

138. A. G. Gibbs, Water-proofing properties of cuticular lipids. *Am. Zool.* **38**, 471–482 (1998).

139. A. Ayari, M. Raimond, C. Souty-Grosset, K. Nasri-Ammar, Hierarchical organization of the cuticle of the subsocial desert isopod, Hemilepistus reaumurii. *J. Struct. Biol.* **193**, 115–123 (2016).

140. N. A. Yaraghi *et al.*, The Stomatopod Telson: Convergent Evolution in the Development of a Biological Shield. *Adv. Funct. Mater.* **1902238**, 1–13 (2019).

141. M. Y. Noh, S. Muthukrishnan, K. J. Kramer, Y. Arakane, Tribolium castaneum RR-1 Cuticular Protein TcCPR4 Is Required for Formation of Pore Canals in Rigid Cuticle, 1–21 (2015).

142. J. Hillerton, S. Reynolds, J. Vincent, On the Indentation Hardness of Insect Cuticle. *J. Exp. Biol.* **96**, 45–52 (1982).

143. G. Pass, Beyond aerodynamics: The critical roles of the circulatory and tracheal systems in maintaining insect wing functionality. *Arthropod Struct. Dev.* **47**, 391–407 (2018).

144. L. Kundanati, S. Signetti, H. S. Gupta, M. Menegon, N. M. Pugno, Multilayer stag beetle elytra perform better under external loading via nonsymmetric bending properties. *J. R. Soc. Interface*. **15** (2018), doi:10.1098/rsif.2018.0427.

145. C. Besjak, P. Biswas, A. Thewis, R. Sweeney, D. Chaudhuri, Chhatrapati shivaji international airport-integrated terminal building. *Struct. Eng. Int. J. Int. Assoc. Bridg. Struct. Eng.* **23**, 8–13 (2013).

146. C. H. E. N. Jin-xiang, N. I. Qing-qing, Y. Endo, M. Iwamoto, Distribution of trabeculae and elytral surface structures of the horned beetle, allomyrina dichotoma (linnÉ) (coleoptera: Scarabaeidae). *Insect Sci.* **9**, 55–61 (2002).

147. O. F. Allomyrzna, D. Linne, C. Jin-xiang, N. I. Qing-qind, Y. Endd, Fine structure of trabecula, 115–123 (2001).

148. M. Y. Noh, S. Muthukrishnan, K. J. Kramer, Y. Arakane, Cuticle formation and pigmentation in beetles. *Curr. Opin. Insect Sci.* **17**, 1–9 (2016).

149. C. Li, S. N. Gorb, H. Rajabi, Cuticle sclerotization determines the difference between the elastic moduli of locust tibiae. *Acta Biomater.* **103**, 189–195 (2020).

150. B. Moussian, Recent advances in understanding mechanisms of insect cuticle differentiation. *Insect Biochem. Mol. Biol.* **40**, 363–375 (2010).

151. N. Suksangpanya, N. A. Yaraghi, R. B. Pipes, D. Kisailus, P. Zavattieri, Crack twisting and toughening strategies in Bouligand architectures. *Int. J. Solids Struct.* **150**, 83–106 (2018).

152. J. C. Weaver *et al.*, The stomatopod dactyl club: A formidable damage-tolerant biological hammer. *Science (80-.).* **336**, 1275–1280 (2012).

153. J. F. V. Vincent, in *Composites Part A: Applied Science and Manufacturing* (Elsevier, 2002), vol. 33, pp. 1311–1315.

154. H. Quan, W. Yang, E. Schaible, R. O. Ritchie, M. A. Meyers, Novel Defense Mechanisms in the Armor of the Scales of the "Living Fossil" Coelacanth Fish. *Adv. Funct. Mater.* **28**, 1–13 (2018).

155. R. Matadi Boumbimba *et al.*, Glass fibres reinforced acrylic thermoplastic resin-based tri-block copolymers composites: Low velocity impact response at various temperatures. *Compos. Struct.* **160**, 939–951 (2017).

156. W. Huang, A. Zaheri, J. Y. Jung, H. D. Espinosa, J. Mckittrick, Hierarchical structure and compressive deformation mechanisms of bighorn sheep (Ovis canadensis) horn. *Acta Biomater.* **64**, 1–14 (2017).

157. J. McKittrick *et al.*, Energy absorbent natural materials and bioinspired design strategies: A review. *Mater. Sci. Eng. C*. **30**, 331–342 (2010).

158. J. J. Connor, S. Faraji, *Fundamentals of structural engineering: Second edition*

(Springer, New York, ed. 2, 2016).

159. S. Boria, A. Scattina, G. Belingardi, Impact behavior of a fully thermoplastic composite. *Compos. Struct.* **167**, 63–75 (2017).

160. N. Enemies, Y. B.-D. and C. J. H. (Editors), Ed. (Elsevier Science B.V., 1997), pp. 165–182.

161. A. Barth, The infrared absorption of amino acid side chains. *Prog. Biophys. Mol. Biol.* **74**, 141–173 (2000).

162. H. Li, Z. Lin, Y. Luo, Gas-phase IR spectroscopy of deprotonated amino acids: Global or Local minima? *Chem. Phys. Lett.* **598**, 86–90 (2014).

163. P. Alagusundaramoorthy, I. E. Harik, C. C. Choo, Flexural behavior of R/C beams strengthened with carbon fiber reinforced polymer sheets or fabric. *J. Compos. Constr.* **7**, 292–301 (2003).

164. L. K. Grunenfelder *et al.*, Bio-inspired impact-resistant composites. *Acta Biomater.* **10**, 3997–4008 (2014).

165. S. Nikolov *et al.*, Revealing the design principles of high-performance biological composites using Ab initio and multiscale simulations: The example of lobster cuticle. *Adv. Mater.* **22**, 519–526 (2010).

166. H. S. Gupta *et al.*, Mechanical modulation at the lamellar level in osteonal bone. *J. Mater. Res.* **21**, 1913–1921 (2006).

167. M. R. Abir, T. E. Tay, H. P. Lee, On the improved ballistic performance of bio-inspired composites. *Compos. Part A Appl. Sci. Manuf.* **123**, 59–70 (2019).

168. T. Apichattrabrut, K. Ravi-Chandar, Helicoidal composites. *Mech. Adv. Mater. Struct.* **13**, 61–76 (2006).

169. L. K. Grunenfelder *et al.*, in *Acta Biomaterialia* (Elsevier Ltd, 2014), vol. 10, pp. 3997–4008.

170. N. A. Yaraghi *et al.*, Biocomposites: A Sinusoidally Architected Helicoidal Biocomposite (Adv. Mater. 32/2016). *Adv. Mater.* **28**, 6769–6769 (2016).

171. Z. Architektur, K. Thomas Van De Kamp, H. Greven, On the architecture of beetle elytra. *Entomol. heute*. **22**, 191–204 (2010).

172. D. Liu, B. B. Raju, X. Dang, Impact perforation resistance of laminated and assembled composite plates. *Int. J. Impact Eng.* **24**, 733–746 (2000).